INFORMATION TO USERS

This manuscript has been reproduced from the microfilm master. UMI films the text directly from the original or copy submitted. Thus, some thesis and dissertation copies are in typewriter face, while others may be from any type of computer printer.

The quality of this reproduction is dependent upon the quality of the copy submitted. Broken or indistinct print, colored or poor quality illustrations and photographs, print bleedthrough, substandard margins, and improper alignment can adversely affect reproduction.

In the unlikely event that the author did not send UMI a complete manuscript and there are missing pages, these will be noted. Also, if unauthorized copyright material had to be removed, a note will indicate the deletion.

Oversize materials (e.g., maps, drawings, charts) are reproduced by sectioning the original, beginning at the upper left-hand corner and continuing from left to right in equal sections with small overlaps.

Photographs included in the original manuscript have been reproduced xerographically in this copy. Higher quality 6" x 9" black and white photographic prints are available for any photographs or illustrations appearing in this copy for an additional charge. Contact UMI directly to order.

ProQuest Information and Learning
300 North Zeeb Road, Ann Arbor, MI 48106-1346 USA
800-521-0600

UMI®

Computational Simulation and Morphological Analysis of Polymerization-induced Phase Separation

by

Junsuk Oh

Department of Chemical Engineering

McGill University, Montreal

November 1999

A Thesis submitted to the Faculty of Graduate Studies and Research in partial fulfillment of the requirements of the degree of Master of Engineering

National Library
of Canada

Acquisitions and
Bibliographic Services

395 Wellington Street
Ottawa ON K1A 0N4
Canada

Bibliothèque nationale
du Canada

Acquisitions et
services bibliographiques

395, rue Wellington
Ottawa ON K1A 0N4
Canada

Your file Votre référence

Our file Notre référence

0-612-64240-2

Abstract

The phase separation method is a practically important method for producing multi-component materials. Particularly, many commercialized polymer blends, such as High-Impact Polystyrene (HIPS) and acrylonitrile-butadiene-styrene (ABS), are manufactured by the polymerization-induced phase separation (PIPS) method, polymerizing monomer compounds (styrene) in the presence of polymers (polybutadiene). In this thesis, rigorous mathematical models, describing the PIPS process, have been formulated using the nonlinear Cahn-Hilliard (C-H) theory and the Flory-Huggins (F-H) theory combined with a second-order reaction equation. In particular, this thesis analyzes and simulates for the first time the PIPS process for the case of a monomer polymerizing in the presence of a polymer. The model equations are solved using the numerical methods, and the simulation results are characterized to identify the main dynamical and morphological phenomena of the PIPS process. Lastly, the PIPS process under a temperature gradient is studied to produce functional composite materials exhibiting space-dependent microstructures and properties.

Résumé

La méthode de séparation de phases est une méthode pratique importante pour la production des matériaux multi-composants. En particulier, plusieurs mélanges commerciaux de polymères comme par exemple le polystyrène haut impact (PSHI) et l'Acrylonitrile-Butadiene-Styrene (ABS) sont produits par méthode de séparation de phases induite par polymérisation (SPIP), en polymérisant des compounds de monomères (Styrene) en présence de polymères (Polybutadiene). Au cours de cette thèse, des modèles mathématiques rigoureux décrivant le procédé SPIP, ont été formulés en utilisant la théorie non-lineaire de Cahn-Hilliard (C-H) et la théorie de Flory-Huggins (F-H) combinée à une équation de réaction de second ordre. En particulier, cette thèse analyse et simule pour la première fois le procédé SPIP dans le cas d'un monomère polymérisé en présence d'un polymère. Les équations du modèle sont résolues en utilisant des méthodes numériques classiques et les résultats de la simulation sont caractérisés en utilisant de nouvelles techniques afin d'identifier les principaux phénomènes dynamiques et morphologiques du procédé SPIP. Pour finir, le procédé SPIP sous gradient de température est étudié afin de produire un matériau composite fonctionnel avec une microstructure et des propriétés spacio-dépendantes.

Acknowledgments

It is a great pleasure to express my deep gratitude to my research supervisor, Professor Alejandro D. Rey, for his sincere and valuable research guidance, motivation, and encouragement, throughout the course of this thesis.

I have been lucky to enjoy excellent working conditions in my computer lab, and I thank to all my colleagues, Arvinder Pal Singh, Ae-Gyeong Cheong, and Dinesh Sharma for their helpful discussions and suggestions. I would like to give special thanks to my officemate, Chang-Wook Choi, who encouraged me for last two years. I am also grateful to Philippe Le Bot for translating the thesis abstract into French.

Lastly, I would like to thank my parents and sister for their love, understanding, support, and sacrifice.

Table of Contents

Chapter 1
Introduction and Background

Chapter 2
Governing Equations for Polymerization-induced Phase Separation

Chapter 3
Computational Simulation and Morphological Analysis of Polymerization-induced Phase Separation

Chapter 4
Computational Simulation of Polymerization-induced Phase Separation under a Temperature Gradient

Chapter 5
Conclusions and Recommendations

List of Symbols

Simbol	Description	Typical units
A	area of the droplet	m^2
A^*	dimensionless collision frequency factor	dimensionless
A_0	collision frequency factor	m^3 $mole^{-1}$ s^{-1}
a	step length of primitive chain	$\overset{o}{A}$
b	bond length	$\overset{o}{A}$
D^*	dimensionless diffusion coefficient	dimensionless
D_A	self diffusion coefficient of polymer A	m^2 s^{-1}
D_B	self diffusion coefficient of polymer B	m^2 s^{-1}
d^*	dimensionless droplet diameter	dimensionless
E	extent of phase separation	-
E^*	dimensionless activation energy	dimensionless
E_0	Arrhenius activation energy	J $mole^{-1}$
F	total free energy of the system	J
f	free energy density of the system	Jm^{-3}
g	ratio of the square radius of a branched molecule to that of a linear one of the same molecular weight	-
I	intensity of segregation	-
J	net flux	-
K^*	dimensionless reaction rate constant	dimensionless
k_1	reaction rate constant	s^{-1}
k_B	Boltzmann constant	J K^{-1}
L	length scale of the computational domain	m

L_t	tube length	$\overset{o}{A}$
l_i	effective interaction length between the molecules	$\overset{o}{A}$
l_m	length of a monomer	m
M	mobility	m^3 s kg^{-1}
M_A	mobility of component A	m^3 s kg^{-1}
M_B	mobility of component B	m^3 s kg^{-1}
M_e	molecular weight between entanglement points	kg $mole^{-1}$
M_m	molecular weight of a monomer	kg $mole^{-1}$
M_p	molecular weight of a polymer	kg $mole^{-1}$
N	degree of polymerization of polymer	-
N'	total number of nodal points in the computational domain	-
N''	total number of couples of concentrations taken	-
N_A	degree of polymerization of polymer A	-
N_B	degree of polymerization of polymer B	-
N_c	critical degree of polymerization	-
N_e	number of monomer units between entanglement points	-
$\vec{n}$	outward unit normal vector	-
n_A	number of molecules of component A	-
n_B	number of molecules of component B	-
n_c	molar volume of the reference unit	m^3 $mole^{-1}$
n_m	number of monomers	-
P	perimeter of the droplet	m
p	extent of reaction	-
R	gas constant	kJ K^{-1} $mole^{-1}$
R	weighted residual	-
R (r)	coefficient of correlation	-

R_g	radius of gyration	Å
r	length of dipole	m
S	boundary of the domain	m^2
S	variance of concentrations	-
s	scale of segregation	-
S_f	shape factor	-
T	absolute temperature	K
T_i	initial temperature	K
T^*	dimensionless temperature	dimensionless
T_1	lowest temperature in a temperature gradient	K
T_1^*	dimensionless lowest temperature in a temperature gradient	dimensionless
T_2	highest temperature in a temperature gradient	K
T_2^*	dimensionless highest temperature in a temperature gradient	dimensionless
t	time	s
t^*	dimensionless time	dimensionless
t_c^*	dimensionless characteristic time	dimensionless
t_i^*	dimensionless induction time	dimensionless
t_{lp}^*	dimensionless polymerization lag time	dimensionless
t_{ls}^*	dimensionless phase separation lag time	dimensionless
t_t^*	dimensionless transition time	dimensionless
U_j	lumped unknown coefficient	-
u_a	approximate solution	-
u_j	unknown coefficient	-
V	volume of the domain	m^3
v	volume of the reference unit	m^3

$\vec{v}$	vector	-
w_i	weight function	-
$\overline{X}_n$	number average molecular weight	-
$\overline{X}_w$	weight average molecular weight	-
α	branching coefficient	-
α	scalar	-
α_c	critical branching coefficient	-
χ	Flory-Huggins' interaction parameter	-
χ_c	Flory-Huggins' interaction parameter at the critical point	-
χ_H	enthalpy contribution to χ	-
χ_S	entropy contribution to χ	-
Φ_A	volume fraction of component A	-
Φ_A^{α}	volume fraction of component A in α phase	-
Φ_A^{β}	volume fraction of component A in β phase	-
Φ_A^1	arbitrary chosen volume fraction of component A	-
Φ_A^2	arbitrary chosen volume fraction of component A	-
Φ_A^*	dimensionless concentration of component A	-
Φ_A^*	volume fraction of component A at the spinodal point	
$\Phi_{A,0}^*$	dimensionless average concentration of component A	-
$\Phi_{A,i,j}^*$	dimensionless concentration of component A at the (i, j)th computational nodal point	-
$\Phi_{A,l}^*$	dimensionless lower binodal concentration of component A	-
$\Phi_{A,u}^*$	dimensionless upper binodal concentration of component A	-
Φ_A^{**}	volume fraction of component A at the spinodal point	-
$\Phi_{A,i}^*$	one of dimensionless concentrations of component A at two points at a distance of r	-

$\Phi^*_{A,i}$	one of dimensionless concentrations of component A at two points at a distance of r	-
Φ_B	volume fraction of component B	-
Φ^*_B	dimensionless concentration of component B	-
Φ_c	critical volume fraction	-
φ^j	global trial and test function	-
φ_j	local basis function	-
γ	functionality of monomer	-
η	local orthogonal coordinate	-
κ	interfacial constant	J/m
κ_0	interfacial constant	J/m
μ_A	chemical potential of component A	J
μ_B	chemical potential of component B	J
Θ	theta temperature	K
σ_0^2	variance for completely unmixed state	-
ς	dipole length at which $R(\varsigma)=0$	m
τ	reduced time	dimensionless
ω^α	volume fraction of α phase	-
ω^β	volume fraction of β phase	-
ξ	local orthogonal coordinate	-
Ψ	dimensionless entropy	-
ψ_j	lumped Hermitian basis function	-
ζ	friction coefficient	kg/s

Chapter 1

Introduction and Background

1.1 General Introduction

Multi-component polymer materials such as polymer solutions, blends and composites find a wide range of engineering applications [1]. The combinations of two or more polymers give higher performance including impact resistance, toughness, high temperature performance, high modulus, and improved elasticity. Blending polymers also offer control over melt viscosity, processability, and solvent resistance. For example, homopolymer polystyrene is very brittle and fractures relatively easily. Mixing polybutadiene with styrene monomer, commercialized under the trade name High-Impact Polystyrene (HIPS), increases impact resistance and toughness of the final plastic. It absorbs more energy on loading, delaying, or preventing fracture. Poly(ethylene terephthalate) is used in nylon-6 tire to reduce flat spotting, and rubber-rubber blends such as polybutadiene or natural rubber, is also used to increase tear resistance. Acrylonitrile-butadiene-styrene (ABS) plastic is one of the fully developed and commercialized materials due to its excellent toughness. The acrylonitrile contributes oil resistance, a higher glass transition temperature to the plastic. The relative position of some commodity thermoplastics is shown in Table 1.1, taking HIPS as a standard [2]. As shown in Table 1.1, HIPS has an excellent price/property balance and ABS has an excellent toughness despite its inferior processability and price. On the other hand, PS does not have toughness and PP has lower processablility due to its crystalline nature and flexional modulus. The commercial importance of multi-component polymer materials is currently remarkable. The total amount of polymer composites and blends constitutes over 30 wt % of the total polymer consumption, with an annual growth rate of about 9 % [3, 4].

However, the great majority of polymer pairs are immiscible due to their endothermic heat of mixing and very small entropy of mixing, and only a few polymer pairs are known to be miscible. When two polymers dissolve even in the rare exception, generally they phase-separate at some temperature and molecular weight, and form multiphase systems. For this reason, phase separation methods have been one of the practical methods to produce multi-component composite materials, and an active research area in material science during the past two decades. Most polymer blends including thermoset / thermoplastic polymer blends, porous polymer membrances, rubber toughened engineering plastics, interpenetrating polymer networks (IPNs) and polymer dispersed liquid crystals (PDLC) are prepared via phase separation methods [5-10].

The phase separation method has a number of advantages compared to other methods. It offers a great deal of variation in the morphologies, depending on the polymer type, the polymer concentration, and the nature of the phase separation process [11]. In addition, films formed by the quenching and polymerization phase separation methods undergo relatively little shrinkage as the polymer phase separates. The polymerization-induced phase separation (PIPS) method is more complex compared to the thermal-induced phase separation (TIPS) method because phase separation and polymerization

	HIPS	PS	ABS	PP
Processablility	S	S	I	I
Toughness	S	P	E	S
Flexional Modulus	S	E	E	I
Surface gloss	S	transparent	E	S
ESCR	S	E	E	E

S: standard; E: excellent; I: inferior; P: poor

Table 1.1 Relative Position of Commodity Thermoplastics [2].

process occur simultaneously in the PIPS method. Nevertheless, the PIPS method involved condensation-reaction polymerization is one of major class of variable multi-phase material production because the phase-separated morphology can be relatively easily controlled by the rate of polymerization and diffusion. Furthermore, the desired morphology can be obtained by controlling the gelation point in the PIPS method. The typical example is the production of high impact polystyrene (HIPS). HIPS is manufactured by the PIPS process, polymerizing styrene in the presence of polybutadiene (PB). As polymerization proceeds, PB phase separates and disperses in the polystyrene (PS) matrix. The particle size of the PB phase can be controlled to obtain the desired properties by a proper choice of the processing conditions.

Polymer blends exhibit a number of morphologies, that is the physical arrangement of the phase domains [1], and the phase-separated morphologies may be simple or complex depending on the phase separation mechanism. Most well-known morphologies in a binary polymer blend system are droplets of phase α dispersed in phase β and interconnected cylinders of phase α in phase β as shown in Figure 1.1. The dispersed droplet-type morphology (Figure 1.1.a) characterizes the structure of a material for which the volume fraction of one phase α is low [12]. In this type of morphology, the droplets are discretely and uniformly distributed in the matrix phase. If the volume fraction of the minor phase α is increased until the critical point, the interconnected cylinder-type morphology (Figure 1.1.b) is observed. A more complex case is the double-diamond interconnected cylinders or onion rings of phase α in phase β. Recently, 'phase within a phase within a phase' is observed in multi-component high-impact polystyrene (HIPS) and acrylonitrite-butadiene-styrene (ABS) materials, as shown in Figure 1.2. Many polystyrene sub-particles also exist inside the polybutadiene particles. The phase-separated morphology, such as droplet size and distribution, is critical in determining the properties of multi-component composite materials [1]. For instance, the fracture toughness increases with decreasing particle sizes and the toughness of the high-impact plastic also increases with the volume fraction of polystyrene inside the polybutadiene droplets. The optical properties of materials are also affected by the phase-separated structures. If the average droplet size decreases, film scattering increases because the number of scattering sites within the film increases, and the film has a translucent white

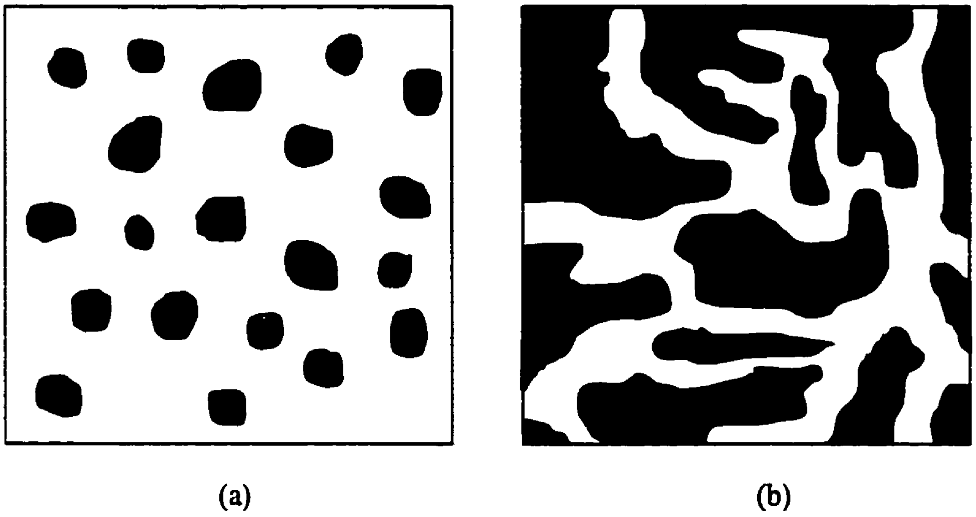

Figure 1.1 Typical phase-separated morphologies in a binary polymer blend system: (a) the droplet type morphology and (b) the interconnected cylinder-type morphology.

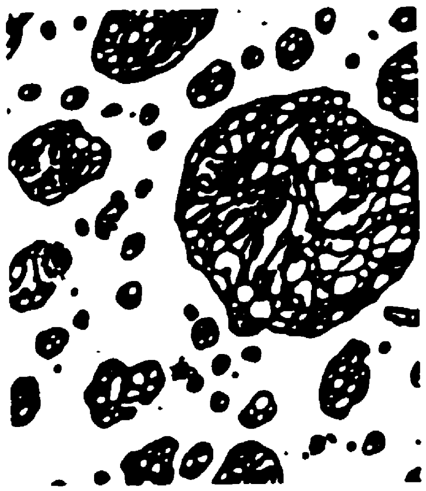

Figure 1.2 Morphology of a high-impact polystyrene (reprinted from reference [2]).

appearance [11]. Therefore, the optimum mechanical behavior for many materials is observed with the particles' size being about 2–5μm, and the spacing between the particles should be of the order of 1–5μm. Consequently, for multi-component composite materials with desirable properties, it is crucial to process the desirable phase-separated morphology.

More recently, an effort has been made to produce a composite material, exhibiting inhomogeneous microstructures (or composition) and properties in some spatial direction, namely a functionally graded material (FGM) [13, 14]. A schematic representation of the microstructure of a two-component FGM is shown in Figure 1.3. The composition gradually varies along the spatial direction. Many current applications of materials require performance, which vary with location within the component. For example, the body of a gear must be tough; however its surface must be hard and wear-resistant. The body of a turbine blade must be strong, tough and creep-resistant, whereas its outer surface must be refractory and oxidation-resistant. However, the abrupt transitions in composition and microstructure cause some serious damage and failure in interfaces. The graded structures designed with which the transition from one material to the other gradually can distribute the local concentrations of stress optically. FGM is also designed to take advantage of certain desirable features of each of the constituent phases [13]. The graded structures are fabricated by the several constructive processes: powder densification, coating or lamination. However, the transport-based processed, based on

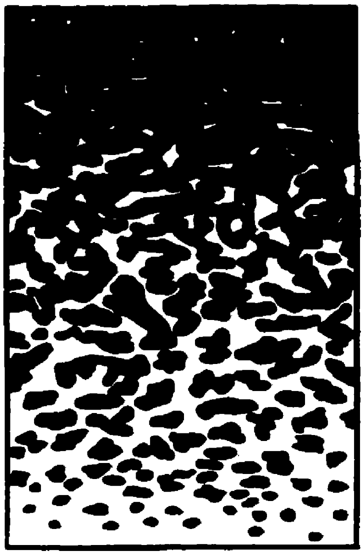

Figure 1.3 Schematic representation of the microstructure of a two-component functionally graded material (FGM), for which the composition gradually varies along the spatial direction (reprinted from reference [13]).

natural transport phenomena, such as the flow of fluid, the conduction of heat and the diffusion of species (in phase separation) can also create gradients in local microstructure and/or compositions that are useful [14]. In this thesis, a spatially dependent PIPS methodology will be applied to produce a FGM.

The objectives of this study are, therefore, to develop a rigorous model of the PIPS process for binary composite materials and to design the desirable phase-separated morphologies with desirable particle size and shape using computational methods. This study is mainly devoted to the PIPS process via spinodal decomposition for binary composite materials. To mimic a processing method for the various commercialized polymer blend materials, we assume that only one component undergoes polymerization in the presence of another polymer component that does not participate in the reaction and that has a constant molecular weight. Additionally, the PIPS process under the temperature gradient field is also studied with the aim to produce spatially graded structures with inhomogeneous microstructures and concentrations. The governing equations with auxiliary conditions of the PIPS process for binary composite materials is developed in Chapter 2. The method of solution is also outlined in Chapter 2, which includes the Galerkin finite elements method with bicubic Hermitian interpolants for spatial discretization and the finite difference method for time integration with a first-order implicit Euler predictor-corrector method and an adaptive time step control step. The governing equation is solved, implemented and validated in Chapter 3. The kinetics of phase separation and the obtained morphologies are characterized using novel dynamical and morphological analysis techniques. In Chapter 4, the governing equations of the PIPS process under a temperature gradients are solved and implemented to simulate the formation of graded materials.

Lastly, in this introductory chapter, the basic concepts of phase separation are presented to understand why (Section 1.2. Thermodynamics of phase separation) and how (Section 1.3: Methods of phase separation, and Section 1.4: Mechanisms of phase separation) phase separation occurs in a multi-component polymeric mixture. In Section 1.5, the nonlinear Cahn-Hilliard (C-H) theory and the Flory-Huggins theory, which are the basic theories for spindoal decomposition, are presented and discussed. Lastly, the description of previous works, the thesis objectives, methodology and organization are given in Section 1.6, 1.7, 1.8, and 1.9, respectively.

1.2 Thermodynamics of Phase Separation

To understand the nature of phase separation in two-component polymeric systems, it is important to understand the mixing properties of the two components, that is, under which conditions two polymers either form a homogeneous phase or a two-phase structure. In order to find out whether mixing occurs, the change in the Gibbs free energy f has to be considered.

The composition Φ_i of component i (i = A, B in a binary system) in terms of its volume fraction is given by:

$$\Phi_A = \frac{N_A n_A}{N_A n_A + N_B n_B} \quad ; \qquad \Phi_B = \frac{N_B n_B}{N_A n_A + N_B n_B} \qquad \text{(1-1-a,b)}$$

$$\Phi_A + \Phi_B = 1 \qquad \text{(1-2)}$$

where N_A and N_B are the degree of polymerization of polymer A and B, respectively, and n_A, n_B are the number of molecules of the corresponding polymers, respectively.

Let us begin with the determination of the free energy of a two-phase α/β mixture. If a two-phase (α and β) structure is formed, the composition of A in each phase is Φ_A^α and Φ_A^β, respectively. If the interphase surface energy of the two-phase mixture is neglected, the total free energy of component A may be written as the sum of the bulk free energies of the each component phases as follows [15]:

$$f_{\alpha.\beta}(\Phi_A) = f\left(\Phi_A^\alpha\right)\omega^\alpha + f\left(\Phi_A^\beta\right)\omega^\beta \qquad \text{(1-3)}$$

where $f_{\alpha.\beta}(\Phi_A)$ is the total Gibbs free energy of the two phases, $f\left(\Phi_A^\alpha\right)$ and $f\left(\Phi_A^\beta\right)$ are the Gibbs free energies of the α and β phases, respectively, and ω^α, ω^β are the volume fractions of the α and β phases, respectively. Thus, from following mass balance relations:

$$\Phi_A^{\alpha}\omega^{\alpha} + \Phi_A^{\beta}\omega^{\beta} = \Phi_A \tag{1-4}$$

$$\omega^{\alpha} + \omega^{\beta} = 1 \tag{1-5}$$

we find that:

$$\omega^{\alpha} = \frac{\Phi_A^{\beta} - \Phi_A}{\Phi_A^{\beta} - \Phi_A^{\alpha}} \quad ; \qquad \omega^{\beta} = \frac{\Phi_A - \Phi_A^{\alpha}}{\Phi_A^{\beta} - \Phi_A^{\alpha}} \tag{1-6-a,b}$$

Substituting Eq. (1-6-a) and (1-6-b) into Eq. (1-3) yields :

$$f_{\alpha,\beta}(\Phi_A) = \frac{\Phi_A^{\beta} - \Phi_A}{\Phi_A^{\beta} - \Phi_A^{\alpha}} f\left(\Phi_A^{\alpha}\right) + \frac{\Phi_A - \Phi_A^{\beta}}{\Phi_A^{\beta} - \Phi_A^{\alpha}} f\left(\Phi_A^{\beta}\right) \tag{1-7}$$

Figure 1.4 shows Eq. (1-7) as a straight line connecting $\left(\Phi_A^{\alpha}, f\left(\Phi_A^{\alpha}\right)\right)$ and $\left(\Phi_A^{\beta}, f\left(\Phi_A^{\beta}\right)\right)$.

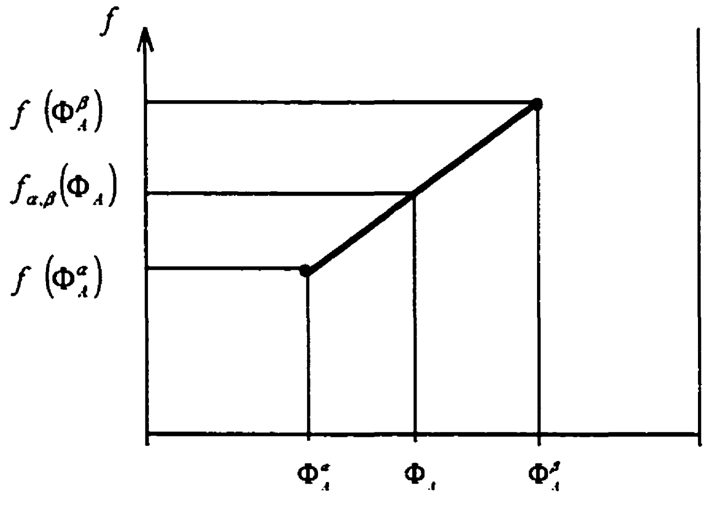

Figure 1.4 The Gibbs free energy, f, as a function of composition of component A, Φ_A for a two-phases mixture, α and β, where $f_{\alpha,\beta}\left(\Phi_A\right)$ is the total Gibbs free energy of two phases, $f\left(\Phi_A^{\alpha}\right)$ and $f\left(\Phi_A^{\beta}\right)$ are the Gibbs free energy of the α and β phases, and Φ_A^{α}, Φ_A^{β} are the concentrations of the mixture in phases α and β, respectively. The free energy of a two-phase mixture has a linear concentration dependence.

The Gibbs free energy of the single-phase mixture is shown as curves in Figure 1.5.a and Figure 1.5.b. Within the composition range $\Phi_A^1 < \Phi_A < \Phi_A^2$ in Figure 1.5.a, the curve describing the free energy of the single-phase mixture lies above the straight line describing the free energy of the two phase-mixture. The mixture cannot be stable in this region because the equilibrium state of a system tends toward the minimal free energy conditions. Consequently, a mixture of a composition corresponding to a point on the convex part of the Gibbs free energy curve, $d^2 f / d\Phi_A^2 < 0$, is unstable against an infinitesimal concentration heterogeneity and decomposition always occurs. This region is called the unstable region and the decomposition phenomena occurs in the unstable region is called spinodal decomposition (SD) [15].

However, if the Gibbs free energy curve is concave within the range $\Phi_A^1 < \Phi_A < \Phi_A^2$, which is characterized by $d^2 f \ / \ d\Phi_A^2 > 0$, it lies below the straight line connecting the points $\left(\Phi_A^1,\ f\ \left(\Phi_A^1\right)\right)$ and $\left(\Phi_A^2,\ f\ \left(\Phi_A^2\right)\right)$ (See Fig 1.5-b.). Thus in this case, the single-phase mixture has less free energy than the two-phase mixture. If a homogeneous mixture characterized by $d^2 f \ / \ d\Phi_A^2 > 0$ at the point Φ_A is unstable to the formation of a two-phase mixture with compositions, Φ_A^α and Φ_A^β, the mixture is stable with respect to infinitesimal fluctuations and the system does not undergo spinodal decomposition.

In the case presented in Figure 1.5.b, however, decomposition may occur under certain circumstances. The region, where decomposition occurs, is called metastable region and the decomposition occurs by the nucleation and growth (NG) mechanism. The boundary line between the unstable region and the metastable region is called the spinodal line. The spinodal line is defined by the expression:

$$\frac{d^2 f}{d\Phi_A^2} = 0 \tag{1-8}$$

Figure 1.6 shows a typical Gibbs free energy versus composition of an asymmetric polymer mixture (A and B), that is, the molecular weight of the mixture's components are different. The shape of the Gibbs free energy curve depends on temperature and molecular weights. When the free energy curve lies above the critical value (the

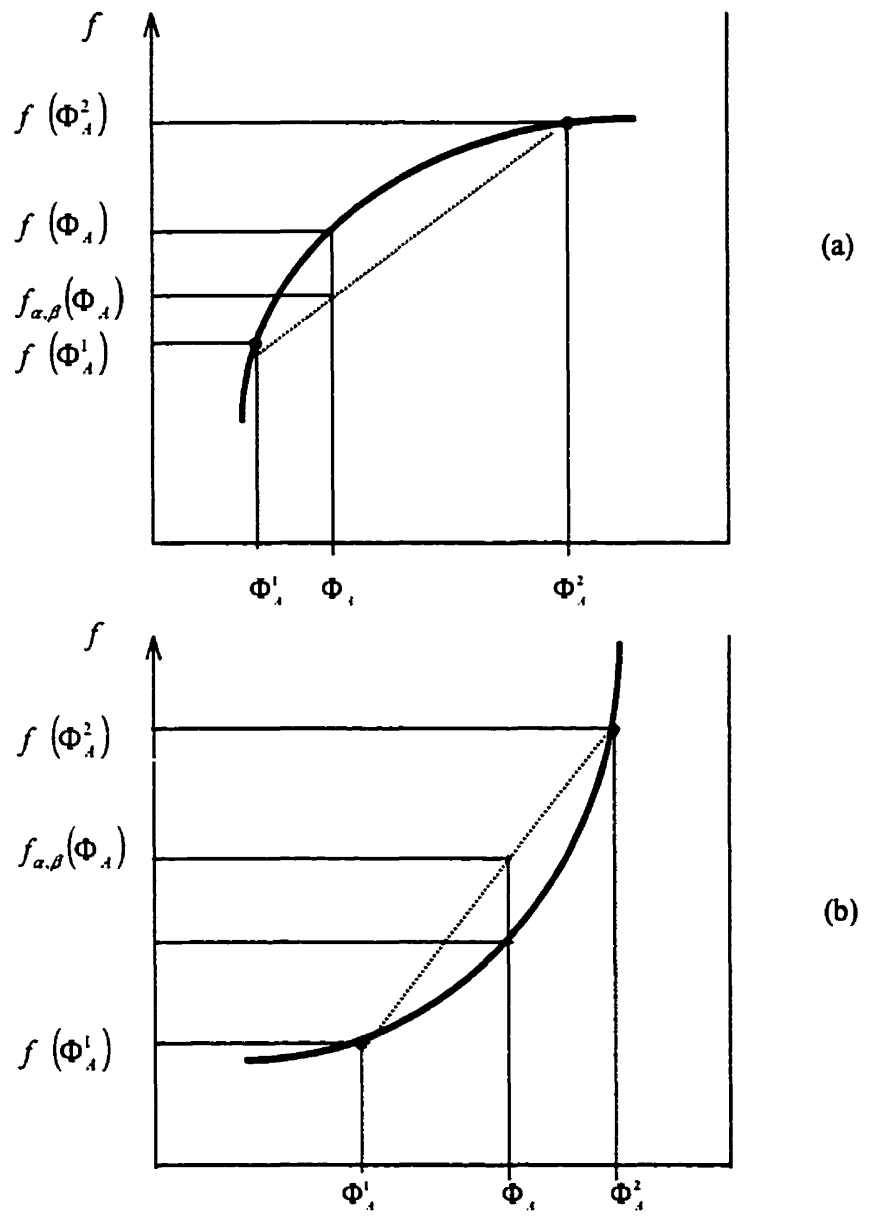

Figure 1.5 The Gibbs free energy, f, as a function of composition of component A, Φ_A, for a single-phase mixture (a solid curve) and two-phase mixture (a dotted line) where Φ_A^1 and Φ_A^2 are the two arbitrary concentrations of component A. (a) The free energy curve describing the single-phase state lies above the straight line describing the free energy of the two-phase mixture. Thus, a single-phase mixture is unstable against decomposition and this instability is called spinodal instability. (b) The free energy curve for a single-phase mixture lies below the straight line for the two-phase mixture. Therefore, a single-phase state is stable and spindoal decomposition does not occur.

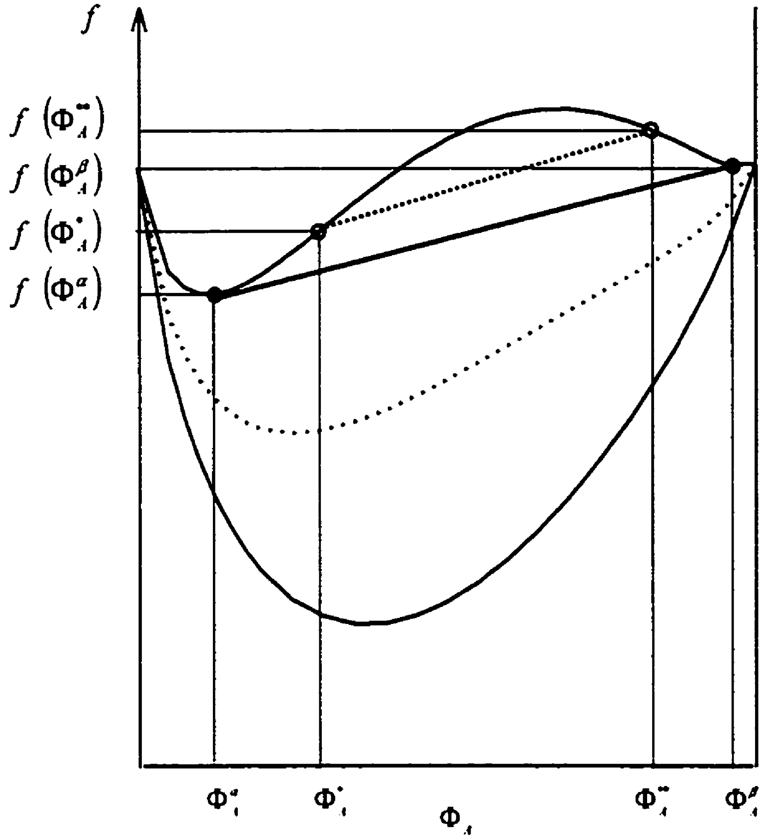

Figure 1.6 Typical Gibbs free energy versus composition diagram of an asymmetric polymer mixture (A and B). The dotted curve represents the critical Gibbs free energy curve and the solid curves represent the arbitrary Gibbs free energy curves. Two spinodal points, $\left(\Phi_A^{*}, f\left(\Phi_A^{*}\right)\right)$ and $\left(\Phi_A^{**}, f\left(\Phi_A^{**}\right)\right)$, denoted by the blanked circles (○) are located at the inflection points of the Gibbs free energy profile. Two binodal points, $\left(\Phi_A^{\alpha}, f\left(\Phi_A^{\alpha}\right)\right)$ and $\left(\Phi_A^{\beta}, f\left(\Phi_A^{\beta}\right)\right)$, denoted by the filled circles (●) are located where the straight tangent line touches the corresponding Gibbs free energy curve.

critical Gibbs free energy curve is denoted by the dotted curve in Figure 1.6.), a maximum point emerges. The spinodal points, $\left(\Phi_A^{*}, f\left(\Phi_A^{*}\right)\right)$ and $\left(\Phi_A^{**}, f\left(\Phi_A^{**}\right)\right)$, characterized by Eq. (1-8) are located at the inflection points of the Gibbs free energy profile. The two spinodal points are denoted by the blanked circle (○) in Figure 1.6. The lowest level of the straight lines describing the two-phase mixture can be represented by the common tangent line of the free energy curve, which connects two points $f\left(\Phi_A^{\alpha}\right)$

and $f\left(\Phi_A^\beta\right)$. Therefore, the regions, $\Phi_A^\alpha < \Phi_A < \Phi_A^*$ and $\Phi_A^{**} < \Phi_A < \Phi_A^\beta$, are metastable regions because the mixture is unstable against the formation of a two-phase mixture but the free energy curve is concave. However, if the free energy curve lies below the critical value, the Gibbs free energy curve is concave everywhere. The curve lies below the two-phase straight line, and the single-phase state has less free energy than the two-phase state. In this case the mixture of two polymers is always stable against decomposition and the system is entirely miscible. This condition is called the stable condition. The boundary line between the metastable region and the stable region is called the binodal line and is set up by two binodal points $\left(\Phi_A^\alpha, f\left(\Phi_A^\alpha\right)\right)$ and $\left(\Phi_A^\beta, f\left(\Phi_A^\beta\right)\right)$. The binodal points are located where the straight tangent line touches the corresponding Gibbs free energy curve. The two binodal points are denoted by the filled circles (●) in Figure 1.6.

1.3 Phase Separation Methods

As mentioned in the previous sections, the phase separation method is widely used to produce binary composite materials. In the phase separation method, phase separation can be accomplished by a change in temperature and/or molecular weight to transfer the mixture from the one-phase (stable) region into the two-phase (unstable or metastable) region. When an initial single-phase mixture is transferred into the two-phase region by thermal quenching, solvent evaporation or polymerization, one of the components phase separates from the other components' phase and forms either dispersed droplets or interconnected cylinders. These methods are called thermal-induced phase separation (TIPS), solvent-induced phase separation (SIPS), and polymerization-induced phase separation (PIPS), respectively [9, 10].

1.3.1 Thermal-induced Phase Separation (TIPS) method

In the TIPS process, a multi-component mixture is prepared at high temperature to form a single-phase mixture. When the mixture is quenched to low temperature (the unstable or metastable region), one component solidifies and the other phase separates. The phase diagram, temperature T versus concentration Φ, for the TIPS process is illustrated in Figure 1.7 (a). In Figure 1.7, the solid curves represent the binodal lines while the dashed curves represent the spinodal lines, where T_i, Φ_0, Φ_c and N_B are initial temperature, the average concentration, the critical concentration and the degree of polymerization, respectively. The TIPS process is useful for thermoplastic polymers that melt below their decomposition temperature [16]. Depending on the average concentration of the components, two types of phase separated structures can be obtained: droplet-type structure in the off-critical region$\left(\Phi_0 \neq \Phi_c\right)$ and the interconnected structure in the critical region$\left(\Phi_0 \approx \Phi_c\right)$. The droplet size in the TIPS process can be controlled by the rate of cooling [9, 10]. For instance, rapid cooling leads to smaller droplet sizes. The droplet size is also dependent on the rate of diffusion, viscosity, and chemical potential of the components. While the TIPS method is simple, the films formed by the TIPS method are often unstable at high temperature and sensitive to the process history [16].

1.3.2 Solvent-induced Phase Separation (SIPS) method

In the SIPS process, an organic solvent is used to solubilize the polymeric materials, and form a single phase. When the solvent evaporates, one component phase separates and disperses as droplets in a polymer matrix. This method is useful for thermoplastic polymers that melt above the decomposition temperature of the thermoplastic [16].

1.3.3 Polymerization-induced Phase Separation (PIPS) method

In the PIPS process, a single-phase mixture is initially prepared. Polymerization induced through the application of heat, light, or radiation leads to the increase of the length of polymer molecules [16, 17]. When the single-phase mixture is thrust into the unstable or metastable region, the solubility of polymer decreases and phase separation occurs. The schematic representation for the PIPS process is shown in Figure 1.7 (b).

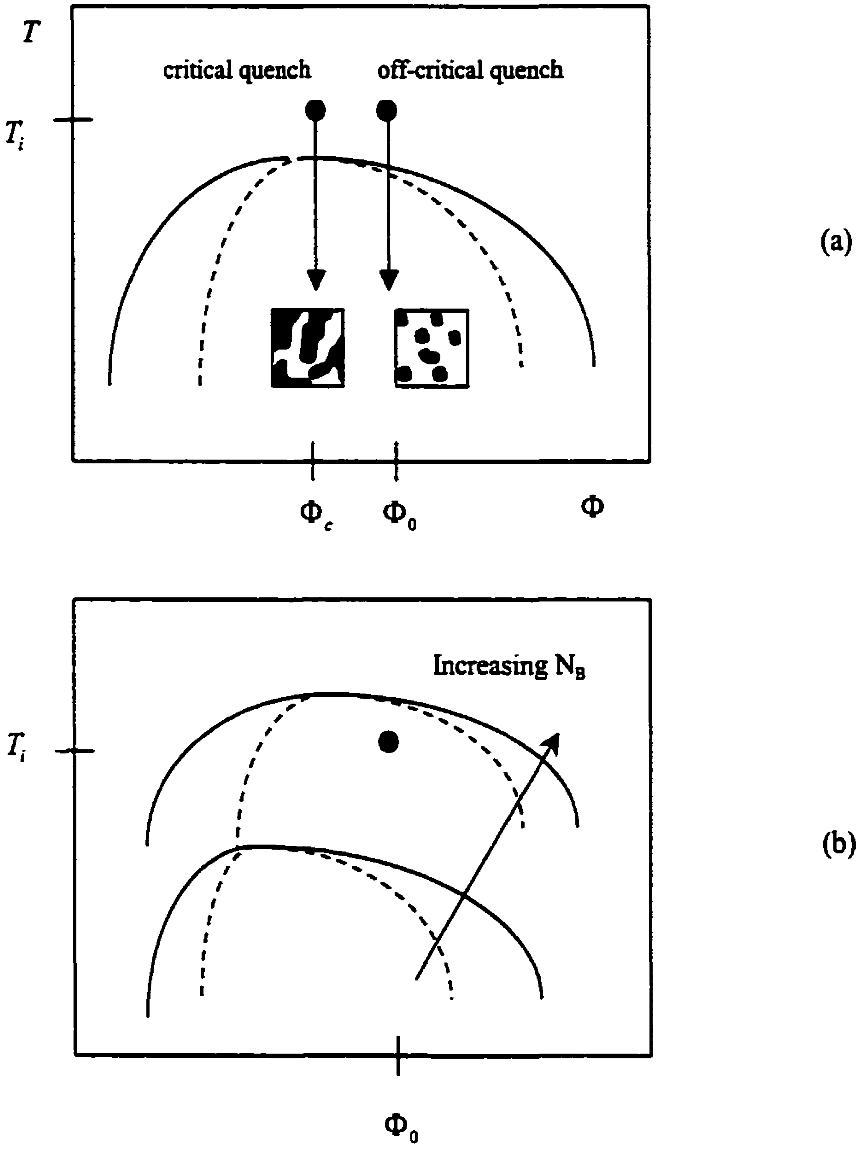

Figure 1.7 Schematic representation of the phase separation methods: (a) the thermal-induced phase separation (TIPS) method and (b) the polymerization-induced phase separation (PIPS) method. The solid curves represent the binodal lines and the dashed curves denote the spinodal lines where T_i, Φ_0, Φ_c, and N_B are initial temperature, the average concentration, the critical concentration and the degree of polymerization of component B. The phase separation phenomena take place when the initially prepared one-phase mixture transferred into the two-phase region by quenching (a) or increasing the degree of polymerization (b).

The PIPS method can be either photo-initiated [18-20] or thermal-initiated [10]. Thiol-ene and acrylate chemistries are mostly applied for photo-polymerization process, and epoxy chemistry is mostly used for thermal-initiated PIPS system. Photo-initiated polymerization usually follows addition polymerization while thermal-initiated system undergoes condensation polymerization or ring-opening polymerization [16]. Epoxy-based PIPS method forms the highly crosslinked networks. These networks can cause unstable long-term behavior of films because they reduce the mobility of unreacted species and these species continue to react over time, changing the properties of the materials [16]. Nevertheless, the PIPS method involved condensation-reaction polymerization is one of major class of PDLC film production.

In the PIPS method, the droplet size can be controlled by the rate of polymerization, the types of polymers used, and physical parameters such as viscosity, rate of diffusion, and solubility of the polymer [9, 10]. The rate of polymerization is controlled by cure temperature and the relative concentration of materials or by light intensity for photochemical polymerization. As the rate of polymerization increases, the crosslinked networks form earlier and the droplets, which are formed by mass diffusion, are not allowed to grow larger.

1.4. Phase Separation Mechanisms

When the mixture is transferred from the one-phase (stable) region into the two-phase (unstable or metastable) region, phase separation occurs. Phase separation can be accomplished by a change in temperature in the TIPS method or in molecular weights of components in the PIPS process. The evolution of a two-phase structure, that arises during phase separation, can be observed by several methods such as light microscopy or scattering experiments.

An example of two temperature jumps from the homogeneous-phase region into the two-phase region for a typical symmetric binary polymer mixture, that is $N_A = N_B$ is illustrated in Figure 1.8. The arrow (a) indicates the temperature change into the metastable region (nucleation and growth) while the arrow (b) jumps into the unstable region (spinodal decomposition). In Figure 1.8, the solid curve denotes the binodal line and the dotted curve represents the spinodal line, respectively. Depending on the location in the two-phase region, phase separation occurs by spinodal decomposition (SD) or by nucleation and growth (NG).

The most significant differences between nucleation and growth (NG) and spinodal decomposition (SD) are the mechanism of decomposition, caused by the different character of the instability [1,15]. Even if a mixture is homogenous, concentrations are not uniform on microscopic scales. There are always fluctuations about the average concentration, $\Phi_{A,0}$, and these fluctuations lead to a change in the Gibbs free energy. Depending on the curvature, the Gibbs free energy can increase or decrease by the concentration fluctuation. In the metastable region, characterized by $\partial^2 f / \partial \Phi_A^2 > 0$, the concentration fluctuation causes the increase in the Gibbs free energy and the structure is stable with respect to spontaneous concentration fluctuation. Therefore, ND is a non-active mechanism and some form of activation mechanisms such as nucleation is necessary. On the other hand, in the unstable region, characterized by $\partial^2 f / \partial \Phi_A^2 < 0$, the fluctuation lead to a decrease in the Gibbs free energy and the system is unstable even

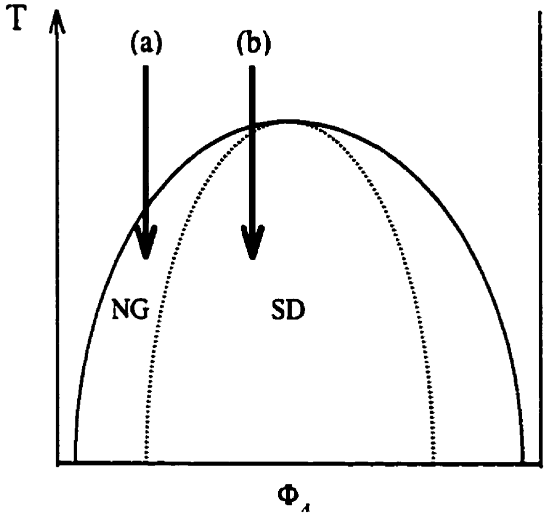

Figure 1.8 Typical phase diagram of a symmetric binary polymer mixture for the TIPS precess. The arrow (a) indicates a temperature change from the homogeneous region into the metastable region (nucleation and growth) and the arrow (b) represents a temperature jump into the unstable region (spinodal decomposition) where the solid curve is binodal line and the dotted curve is spinodal line.

for an infinitesimally small fluctuation. Phase separation takes place spontaneously and continuously. SD is an active and irreversible mechanism, that is, once the phase separation has occurred, the system cannot homogenize.

Figure 1.9 shows phase separation mechanism for nucleation and growth (top) and spinodal decomposition (bottom) where (a-1) and (b-1) represent the early stage of phase separation while (a-2) and (b-2) represent the intermediate stage, and (a-3) and (b-3) denote the late stage of phase separation. If a nucleus of composition Φ_A^{α} is formed in

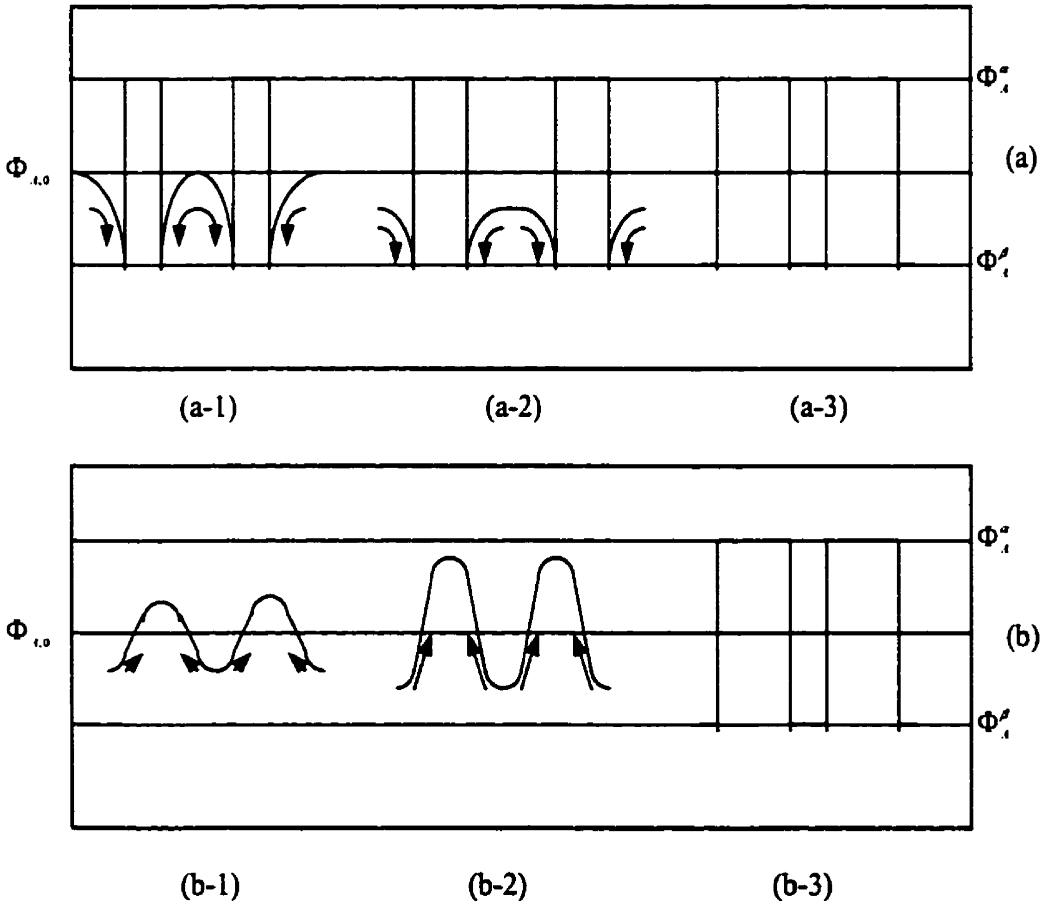

(a-1) (a-2) (a-3)

(b-1) (b-2) (b-3)

Figure 1.9 Schematic representation of phase separation mechanisms for nucleation and growth (a), and spinodal decomposition (b) where $\Phi_{A,0}$ denotes the average concentration, and Φ_A^{α}, Φ_A^{β} represent the concentration in phase α and β in the early, (a-1) and (b-1), intermediate, (a-2) and (b-2), and late, (a-3) and (b-3), stages, respectively. The arrows indicate the direction of the diffusion of the molecules. The diffusion coefficient is positive in nucleation and growth mechanism, while it is negative in spinodal decomposition.

NG process (a-1), the composition of the matrix in the immediate vicinity of that nucleus would be Φ_A^β through the phase separation process, (see (a-2) and (a-3)). During phase separation of NG, the composition of the minor component domains, that is nucleus, remains constant, and only size of the domains and its distribution change with time. On the other hand, in SD, a multi-component system of composition $\Phi_{A,0}$ with a concentration fluctuation continuously decompose into two phases of composition Φ_A^α and Φ_A^β. In this case, both the composition and size of the domains increase continuously with time (see (b-1) and (b-2)). At the late stage of SD, (b-3), the wavelength of the oscillation is fixed by the scale of phase-separated structure, which has the minimization condition of the free energy. The arrows in Figure 1.8 indicate the direction of diffusion of the component A. The diffusion coefficient can be negative or positive depending on the sign of the curvature $\partial^2 f / \partial \Phi_A^2$. Therefore, as we can see, the molecules diffuse from higher concentrations toward lower concentrations in NG, that is positive diffusion; however, in SD, the diffusion coefficient is negative and abnormally molecules diffuse toward higher concentrations from lower concentration.

1.5 Spinodal Decomposition Theories.

1.5.1 Cahn and Hilliard Equation

The idea of the gradient contribution to the thermodynamic properties of materials was first presented by Cahn and Hilliard [21]. In systems with large spatial inhomogeneity, the local density of thermodynamic functions, such as entropy, volume, energy, etc., depends not only on the values of the intensive properties in the volume element but also on their local gradients [22]. For a system undergoing spinodal decomposition, the length scale of the concentration profile is of the order of 10nm or shorter, thus the contribution of its local gradients is not negligible. The composition fluctuations of this length scale which lead to phase separation occur in spinodal decomposition. Thus the C-H equation has been widely used for phase separation process as well as pattern formation [23, 24]. According to the Cahn and Hilliard assumption, the total free energy F can be expressed as the integral of the sum of a homogeneous contribution $f(\Phi_A)$ and a gradient contribution $\nabla\Phi_A$:

$$F = \int \left[f^{\circ}(\Phi_A) + \kappa(\nabla\Phi_A)^2 \right] dV \tag{1-9}$$

where κ is a positive interfacial constant and $f^{\circ}(\Phi_A)$ denotes the free energy of homogeneous concentration. Eq. (1-9) can be obtained from the Taylor series expansion of a local free energy density, as follows:

$$f(\Phi_A, \nabla\Phi_A, \nabla^2\Phi_A, \ldots) = f^{\circ}(\Phi_A) + \kappa_1\nabla^2\Phi_A + \kappa_2(\nabla\Phi_A)^2 + \ldots \tag{1-10}$$

where

$$\kappa_1 = \frac{\partial f}{\partial \nabla^2\Phi_A} \quad \text{and} \quad \kappa_2 = \frac{\partial^2 f}{\partial |\nabla\Phi_A|^2} \tag{1-11-a,b}$$

If higher order terms in Eq. (1-10) are neglected, the total free energy F of this volume will be:

$$F = \int \left[f^{\circ}(\Phi_A) + \kappa_1\nabla^2\Phi_A + \kappa_2(\nabla\Phi_A)^2 \right] dV \tag{1-12}$$

By assuming the surface gradients are zero, and applying the divergence theorem and natural boundary conditions [21], $\nabla\Phi_A \cdot \vec{n} = 0$, the second term in the right hand side in Eq. (1-12) may be expressed as:

$$\int (\kappa_1\nabla^2\Phi_A)dV = -\int (d\kappa_1 / d\Phi_A)(\nabla\Phi_A)^2 dV + \int (\kappa_1\nabla\Phi_A \cdot \vec{n})dS = -\int (d\kappa_1 / d\Phi_A)(\nabla\Phi_A)^2 dV \tag{1-13}$$

Thus, Eq. (1-12) can be simply written as:

$$F = \int \left[f^{\circ}(\Phi_A) + \kappa(\nabla\Phi_A)^2 \right] dV \tag{1-14}$$

where

$$\kappa = \kappa_2 - \frac{d\,\kappa_1}{d\,\Phi_A} \tag{1-15}$$

The most important feature of Eq. (1-14), compared to the classical mass diffusion equation, is the additional term which is proportional to the square of the gradient of the composition distribution, $(\nabla\Phi_A)^2$.

In order to describe phase transition in binary systems, the model equation can be derived from a continuum model [25, 26]. If we consider only pure diffusion, the net flux J might be expressed as chemical potentials per unit volume of each component, μ_A and μ_B, as:

$$J = -M\nabla(\mu_B - \mu_A) \tag{1-16}$$

where M is total mobility [27, 28] in the given system which depend on the volume fractions Φ_A and Φ_B. General thermodynamic relation between the chemical potential and the free energy which can be written as:

$$\mu_B - \mu_A = \frac{\partial F}{\partial \Phi_A} \tag{1-17}$$

Hence, Eq. (1-16) gives [25]:

$$J = -M\nabla\frac{\partial F}{\partial \Phi_A} \tag{1-18}$$

By inserting Eq. (1-18) into the continuity equation for a non-reacting mixture:

$$\frac{\partial \Phi_A}{\partial t} + \nabla \cdot J = 0 \tag{1-19}$$

we can obtain the following equation:

$$\frac{\partial \Phi_A}{\partial t} = \nabla \cdot \left[M\nabla\left[\frac{\partial f}{\partial \Phi_A} - 2\kappa\nabla^2\Phi_A\right]\right] \tag{1-20}$$

Eq. (1-20) is the fourth-order non-linear partial differential equation that governs the spatial and temporal evolution of concentration fluctuation in spinodal decomposition.

1.5.2 Flory-Huggins Theory

To describe the phase separation phenomena, an appropriate expression for the bulk free energy density f in the nonlinear C-H equation, Eq. (1-20), has to be selected. The most widely and successfully used theory in polymer studies is the Flory-Huggins (F-H) theory [29, 30]. The Flory-Huggins treatment represents the free energy density of mixing, f, as a sum of two contributions [30]. The increase in the configurational entropy associated with the increase of motion of all the polymer molecules during the mixing process, and the change in the local interactions and motions of the monomers. Combining these two contributions and assuming that the two polymer species have the same volume v and they occupy the cells of a regular lattice [30], the F-H free energy density of mixing f can be expressed as:

$$\begin{aligned} f &= RTn_c\left(\frac{\Phi_A}{N_A}\ln\Phi_A + \frac{\Phi_B}{N_B}\ln\Phi_B + \chi\,\Phi_A\Phi_B\right) \\ &= \frac{k_B T}{v}\left(\frac{\Phi_A}{N_A}\ln\Phi_A + \frac{\Phi_B}{N_B}\ln\Phi_B + \chi\,\Phi_A\Phi_B\right) \end{aligned} \tag{1-21}$$

where R is the gas constant, T is the absolute temperature, χ is the temperature-dependent Flory's interaction parameter, k_B is Boltzmann constant, v is the volume of each polymer species, and n_c is the molar volume of the reference unit, i.e. the molar volume of each polymer species given by:

$$n_c = \left(\frac{V}{v}\right) \tag{1-22}$$

where V is the total volume of the system. Additionally, we assume that the volume change of mixing is negligible. Note that, for $\Phi_A \to 0$ and $\Phi_B \to 0$, the local free energy term in Eq. (1-21), $\chi\,\Phi_A\Phi_B$, must vanish. Miscibility between two polymers occurs when

χ has negative values, but the two polymers are incompatible with each other when χ is positive. The interaction parameter χ can be expressed as the addition of two contributions, an entropic part χ_s and an enthalpy part χ_H [31]:

$$\chi = \chi_s + \chi_H \tag{1-23}$$

Since, in most polymer mixtures the entropic part χ_s is positive due to very small combination of entropy of mixing, the compatibility of two polymers is determined by the enthalpy term. However, endothermal conditions are dominant in polymers and the great majority of polymer mixtures are immiscible [32]. Only when special local interactions exist between A and B monomers, miscibility is possible.

1.6 Previous Works and Motivation of Present Thesis

The polymerization-induced phase separation (PIPS) method, coupled phase separation and polymerization, has been modeled using the time dependent nonlinear Cahn-Hilliard theory, the Flory-Huggins (F-H) theory for phase separation, and a reaction kinetic equation for polymerization, in the previous studies [33-35]. It has been found that the combination of diffusion and reaction mechanisms determines the length scale of the phase separation patterns, and the phase-separated morphology can be controlled by the rate of diffusion and polymerization. However, relatively few studies have been completed on the PIPS method because it is a more complicated process than the classical thermal-induced phase separation (TIPS) method. Many numerical studies have been performed assuming that the mobility of a polymer and its interfacial parameter are constants with an attempt to simplify the problems [36-41] and only a few studies have been performed with a molecular weight and concentration dependent mobility [42, 43]. Therefore, the classical model equations describing the PIPS process are not realistic since the expressions for the mobility used in the previous studies are inaccurate. In addition, computational divergence problem occurs in the classical numerical studies for highly asymmetric polymer systems, and the attempts have failed in describing practically important process, such as a monomer polymerizing in the presence of a polymer.

1.7 Thesis Objectives

The objectives of the present thesis are as follows:

1. To formulate, solve and validate a mathematical model that describes the polymerization-induced phase separation method, suitable for the widely commercialized polymer blend material process, that is, a monomer B polymerizing in the presence of a polymer A.

2. To develop an appropriate expression for mobility that depends both on the molecular weight of components and their local concentration.

3. To formulate, solve and validate a mathematical model that describes the polymerization-induced phase separation process under a temperature gradient.

4. To develop a characterization method of the state of mixing and the phase-separated morphologies.

1.8 Methodology

In this thesis, the computational simulation of polymerization-induced phase separation has been carried out using the following procedure:

1. Specify the independent variables (time and space dimensions) and dependent variables of the model. The dependent variables are initial concentration of component A and the degree of polymerization of component B. To do this, it is

necessary to calculate phase diagrams numerically using the Flory-Huggins equation for our particular conditions.

2. Derive the appropriate expression for mobility that depends on the molecular weight of components and their local concentration to reflect the diffusion behavior of polymer molecules with increasing the molecular weight and changing their local concentration in the PIPS process.

3. Derive the governing time-dependent partial differential equations to describe the PIPS process using the expression of mobility derived in step 2 and the conditions specified in step 1. The Cahn-Hilliard and Flory-Huggins theories are used for phase separation and the first-order kinetic reaction equation is used for polymerization.

4. Derive the appropriate boundary and initial conditions to solve the governing equation developed in step2. The zero mass flux and natural boundary conditions, and the randomly generated initial conditions are used to reflect the infinitesimal thermal concentration fluctuations initially presented.

5. Nondimensionalize the governing equations and boundary conditions obtained in step 3 and 4 to obtain the dimensionless parameters.

6. Develop a computation program using the Galerkin finite element method with Hermitian bicubic basis functions to solve the dimensionless governing equation and boundary conditions obtained in step 4.

7. Solve the computation program obtained in step 6 using the appropriate dimensionless parameter values.

8. Analyze the computer simulation output. The primary outputs are concentration of component A and the degree of polymerization of component B. The secondary outputs are the results from calculation of the extent of phase separation for the dynamical analysis, and calculation of the intensity and scale of phase separation, the

dimensionless average droplet diameter, and the shape factor for the morphological analysis.

9. Derive the governing time-dependent partial differential equations to describe the PIPS process under a temperature gradient using the expression of mobility derived in step 2 and the conditions specified in step 1. The Cahn-Hilliard and Flory-Huggins theories are used for phase separation and the first-order kinetic reaction equation is used for polymerization. The space dimension, the diffusion coefficient, the reaction rate constant and the Flory-Huggins interaction parameter are dependent on temperature in the part of the thesis. The temperature dependent reaction rate constant is obtained using the chemical Arrhenius equation.

10. Follow step 4, 5, 6, 7, and 8 to solve the governing equation derived in step 9.

11. Finally, validate the simulation results with published data.

The computational modeling procedure based on our objectives and methodology is given in Figure 1.10, in a compact flow-chart format. As shown in Figure 1.10, the primary step in the numerical study is to propose objectives. As a secondary step, a model is developed and implemented based on these objectives, existing theories, and experimental data. The model is then solved using the appropriate computational methods. Lastly, the numerical results obtained from the simulations are characterized such that they can be validated with existing experimental data.

1.9 Thesis Organization

The thesis organization is as follows:

Chapter 1 presented a general introduction and a background of this thesis, including an industrial and academic motivation, the nature and methods of the phase separation phenomena, and the thesis objective and organization.

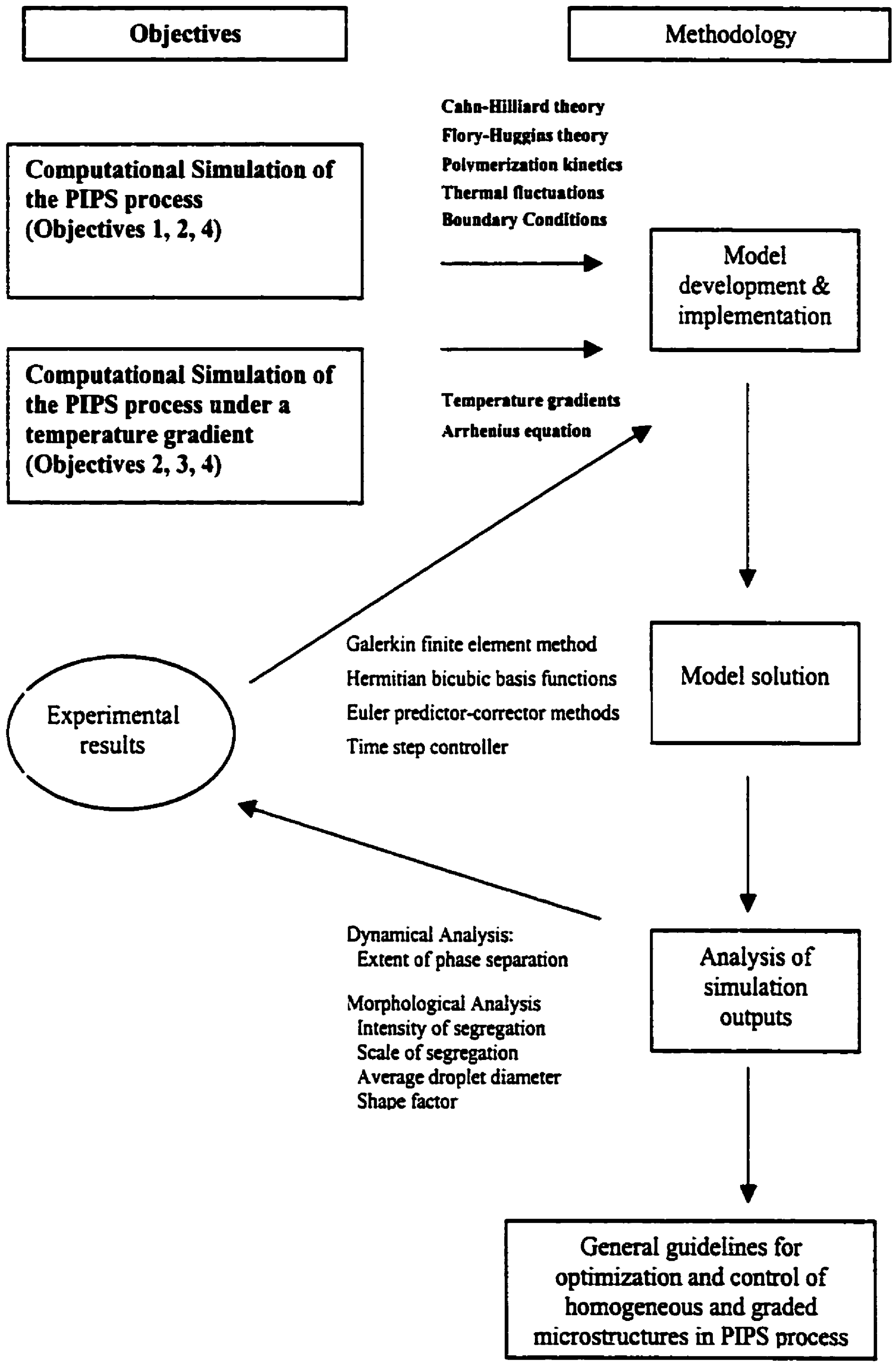

Figure 1.10 Computational modeling procedures based on our objectives and methodology

Chapter 2 presents the mathematical model equation that describes the polymerization-induced phase separation, ranging from the low molecular weight regime to the high molecular weight regime. The model is composed of the nonlinear Cahn-Hiliard and Flory-Huggins theories for spinodal decomposition and the first-order kinetic reaction equation for polymerization. A rigorous expression for mobility in the Cahn-Hilliard theory is also derived in this chapter.

Chapter 3 presents results from computational simulation of polymerization-induced phase separation. Numerical results that describe the time dependent morphological evolution of concentration fluctuations in spinodal decomposition are characterized and discussed dynamically and morphologically, performing an extensive dimensionless parametric study.

Chapter 4 presents results from numerical simulation of polymerization-induced phase separation under a temperature gradient field. Numerical results that show the spatially inhomogeneous phase-separated structure are elucidated to design and tailor the morphology with desirable properties for high performance.

Chapter 2

Governing Equations for Polymerization-induced Phase Separation

Summary

When a monomer (component B) polymerizes in the presence of another polymer (component A), the initial one-phase mixture phase-separates via spinodal decomposition. The model equations based on the Cahn-Hilliard theory and the Flory-Huggins theory are developed to describe this polymerization-induced phase separation (PIPS) process. The theoretical models derived in this study can cover the range from the polymer's low molecular weight regime to the highly entangled molecular weight regime, using the different diffusion theories. The expression for the mobility is also developed, that is dependent on the molecular weight of components and their local concentration.

2.1 Introduction

Phase separation is a common technique for producing multi-component composite materials such as thermoset / thermoplastic blends, porous polymer membranes and polymer dispersed liquid crystal (PDLC) films [5-10]. As a result, phase separation in general and spinodal decomposition (SD) in particular have been active areas of material science research. A great number of experimental [5-10, 44-47] and theoretical [33-38, 42-43, 48-51] studies on SD have been performed intensively during the past two decades. The majority of these works has been performed under thermodynamic equilibrium conditions, but recently a few studies has been performed on the phase behavior under external fields such as shear flow [52-54] or electric fields [55, 56]. However, relatively few studies have been completed on the polymerization-induced phase separation (PIPS) method [33-35, 50] because it is a more complicated process than the thermal-induce phase separation (TIPS) method, although the PIPS process has many advantages over other phase separation techniques.

The variable properties of polymer mixtures are caused by their morphology or phase separated structure. For instance, the properties of PDLC films, such as scattering, reflection, solar energy transmission, and the switching response time, are determined by the droplet size, orientation, distribution, etc [9, 10]. The toughness of high impact polystyrene (HIPS) can be increased with decreasing droplet size. In the PIPS process, it has been shown that the resulting morphology can be controlled by changing cure temperature, polymerization rate or concentration [9, 10]. To obtain desired material properties, solidification of phases such as gelation can also be used [33, 34].

The phase separation phenomena combined with polymerization has been modeled using the time dependent Cahn-Hilliard (C-H) theory and the Flory-Huggins (F-H) theory for phase separation, and the reaction kinetic equation for polymerization. Glotzer et al [35] solved the nonlinear Cahn and Hilliard equation with coupled diffusion and chemical reaction. They found that the combination of diffusion and reaction mechanisms determines the length scale of the phase-separated pattern. However, they used the solvent and solute system, thus the mobility (see Eqs. (2-16) and (2-17)) was constant. Lin and Taylor [50] studied theoretically the PIPS method to understand the effects of temperature, polymerization rate and concentration on the resulting droplet size and uniformity. They simulated the morphological evolution by evaluating the energy difference between a randomly selected site and one of its neighbors, and exchanging their occupancies if the energy difference is negative. Chan and Rey [33, 34] solved the nonlinear fourth-order C-H equation to study the effects of diffusion coefficient and polymerization rate on the phase separated morphology in the PIPS process. However, they studied only polymer solutions. In addition they used the concentration independent mobility, thus their equation diverges when the concentration approaches unity for an asymmetric polymer solution system. Shaginyan and Manevich [57] studied the initial stage of the PIPS process of a multi-component blend. The degree of polymerization of the second component N_s is determined by the time dependent reaction conversion factor in their study. However, the molecular weight effect on the mobility was not considered in their study. It is known that the mobility is highly dependent on the molecular weight of component and their local concentration as suggested by several authors [42, 43]. Consequently, the classical model equations describing the PIPS process are not realistic since the expressions for the mobility used in previous works are inaccurate. The objective of this chapter is to develop a generally valid model and an accurate expression for the mobility

In this chapter, two governing equations are developed to describe the PIPS process taking into account the concentration and molecular weight dependence of the mobility. The mobility is formulated to reflect the effect of the polymer chain length growth due to reaction by using the Rouse theory in the non-entanglement regime [58] and the de Gennes' reptation theory in the entanglement regime [59, 60]. Non-periodic boundary conditions and zero mass flux boundary conditions are used to solve the governing equations [33, 34, 48, 49].

2.2 Theory of the Governing Equations

2.2.1 Theory of Spinodal Decomposition

This section briefly summarizes the theoretical background and spinodal decomposition (SD) equations presented in Chapter 1. Phase separation via SD can be induced by thermal quenching, solvent evaporation or polymerization, namely the thermal-induced phase separation (TIPS), solvent-induced phase separation (SIPS) and polymerization-induced phase separation (PIPS), respectively [9, 10]. In the PIPS method, as the molecular weight of component increases due to polymerization reaction, the phase diagram shifts toward higher temperature and concentration. When the homogeneous initial system located in the stable region above the binodal line passes over the spinodal line, it is thrust into the unstable region and phase separation occurs.

The Cahn and Hilliard (C-H) theory [21] is most widely used theory for phase separation via SD [23] because it takes into account the contribution of the local gradients. According to C-H's assumption, the total free energy F can be expressed as the integral of the sum of two contributions; homogenous contribution $f(\Phi_A)$ and gradient contribution $\nabla\Phi_A$ as follows:

$$F = \int \left[f(\Phi_A) + \kappa(\nabla\Phi_A)^2\right] dV \tag{2-1}$$

where κ is a positive interfacial constant, Φ_A is the volume fraction of polymer A, and V is the total volume of the system. For binary mixture, $\Phi_A = 1 - \Phi_B$, where Φ_B is the volume fraction of polymer B. Eq. (2-1) has been obtained from the Taylor series expansion with the natural boundary conditions, $\nabla\Phi_A \cdot \vec{n} = 0$. By using a continuum model equation [25, 26] and expressing the net flux J with chemical potentials, the following forth-order partial differential equation can be obtained:

$$\frac{\partial \Phi_A}{\partial t} = \nabla \cdot \left[M(\Phi_A, N_A, N_B)\nabla \frac{\partial f}{\partial \Phi_A} - 2\kappa\nabla^2\Phi_A \right] \tag{2-2}$$

where M is concentration and molecular weight dependent mobility, t is time, and N_A and N_B are the degree of polymerization of polymers A and B, respectively.

An appropriate expression for the bulk free energy density has to be selected to solve the nonlinear C-H equation, Eq. (2-2), and the most widely and successfully used theory is the Flory-Huggins (F-H) theory [29, 30]. The F-H free energy of mixing f is expressed as:

$$\begin{aligned} f &= RTn_c\left(\frac{\Phi_A}{N_A}\ln\Phi_A + \frac{\Phi_B}{N_B}\ln\Phi_B + \chi\,\Phi_A\Phi_B\right) \\ &= \frac{k_BT}{v}\left(\frac{\Phi_A}{N_A}\ln\Phi_A + \frac{\Phi_B}{N_B}\ln\Phi_B + \chi\,\Phi_A\Phi_B\right) \end{aligned} \tag{2-3}$$

where R is the gas constant, T is the absolute temperature, n_c is the molar volume of the reference unit, χ is temperature dependent interaction parameter, k_B is Boltzmann constant, and v is the volume of the reference unit. In Eq. (2-3), the first two terms inside parenthesis represent the contribution of the configurational entropy and the last term represents the contribution of the enthalpy of mixing. The interaction parameter χ is a function of temperature and can be written as [31]:

$$\chi = \frac{1}{2} - \Psi\left(1 - \frac{\Theta}{T}\right) \tag{2-4}$$

where Ψ is the dimensionless entropy and Θ is the theta temperature defined by:

$$\Psi = \frac{1}{2} - \chi_s \tag{2-5}$$

$$\Theta = \frac{\chi_H T}{1/2 - \chi_s} \tag{2-6}$$

where χ_H and χ_s are the enthalpy and entropy contribution to χ, respectively.

2.2.2 Molecular Weight and Concentration Dependence of Mobility and Interfacial Parameter.

In the PIPS method, the polymer molecular weight constantly increases during the polymerization process, and the local concentration continuously changes due to phase separation. The mobility M and interfacial parameter κ are dependent on both the polymer molecular chain length and local concentration. Many numerical studies, however, have been performed assuming that M and κ are constants with an attempt to simplify the problems [36-41] and only a few studies have been performed with a molecular weight and concentration dependent mobility [42, 43]. The interfacial parameter κ can be assumed to be concentration independent in the absence of any accurate information about its behavior; however, M is known to be highly sensitive to concentration changes [43].

The molecular chain lengths and local concentration dependence of the mobility can be captured from its relation with the self-diffusion coefficient [61-63] as:

$$D_A = M_A \frac{\partial^2 f}{\partial \Phi_A^2} \tag{2-7-a}$$

$$D_B = M_B \frac{\partial^2 f}{\partial \Phi_B^2} \tag{2-7-b}$$

where D_A and D_B are the self-diffusion coefficients of polymer segments and f is the free energy of mixing. In Eqs. (2-7-a) and (2-7-b), an expression of $\partial^2 f / \partial \Phi^2$ can be formed using the Flory-Huggins theory when we neglect any interactions between polymer chains [59], as follows:

$$\frac{\partial^2 f}{\partial \Phi_A^2} = \frac{k_B T}{v}\left(\frac{1}{N_A \Phi_A} + \frac{1}{N_B \Phi_B}\right) \tag{2-8-a}$$

$$\frac{\partial^2 f}{\partial \Phi_B^2} = \frac{k_B T}{v}\left(\frac{1}{N_A \Phi_A} + \frac{1}{N_B \Phi_B}\right) \tag{2-8-b}$$

Substituting $\partial^2 f / \partial \Phi^2$ in Eqs. (2-7-a) and (2-7-b) with Eqs. (2-8-a) and (2-8-b), we obtain the following expressions of the mobility of polymer segments:

$$M_A = \frac{D_A}{\dfrac{k_B T}{v}\left(\dfrac{1}{N_A \Phi_A} + \dfrac{1}{N_B \Phi_B}\right)} \tag{2-9-a}$$

$$M_B = \frac{D_B}{\dfrac{k_B T}{v}\left(\dfrac{1}{N_A \Phi_A} + \dfrac{1}{N_B \Phi_B}\right)} \tag{2-9-b}$$

The total mobility can be obtained by simply adding up M_A^{-1} and M_B^{-1} as:

$$M = \frac{M_A M_B}{M_A + M_B} \tag{2-10}$$

This mixing rule has been used for deriving the total mobility in the system by de Gennes [59]. Thus, we find that the total mobility can be expressed by inserting Eqs. (2-9-a) and (2-9-b) into Eq. (2-10) as:

$$M = \frac{D_A D_B N_A N_B \Phi_A \Phi_B}{\left(\frac{k_B T}{v}\right)(D_A + D_B)(N_A \Phi_A + N_B \Phi_B)} \tag{2-11}$$

H. Zhang et. al [42] arrived at a similar result for the mobility.

All diffusion phenomena of polymers are nearly proportional to either N^{-1} or N^{-2}, depending on their molecular weight. Published data shows that in the low molecular weight regime, $N < N_c$, where the material dependent N_c is the critical degree of polymerization, diffusion of polymer exhibits an N^{-1} dependence as expected from the Rouse prediction [58]. The diffusion coefficient based on the Rouse theory is written as:

$$D = \frac{k_B T}{N\zeta}, \qquad N < N_c \tag{2-12}$$

where ζ is a friction coefficient characteristic of the interaction of a bead with its surrounding (Rouse model represents the polymer chain as a linear series of beads connected by springs).

On the other hand, in the high molecular weight regime, $N > N_c$, diffusion of polymers would depend on the inverse square of the molecular weight since polymer properties such as diffusion coefficient or viscosity are affected by entanglements. The reptation model represents the behavior of the highly entangled polymers and the diffusion coefficient may be written as [59, 60, 64]:

$$D = \left(\frac{k_B T}{3\zeta}\right)\frac{\langle R_g^2 \rangle}{N L_t^2} = \left(\frac{k_B T}{3\zeta}\right)\frac{a^2}{N^2 b^2}, \qquad N > N_c \tag{2-13}$$

where R_g is the radius of gyration, L_t is the tube length (the reptation model imagines that the motion of the polymer chain is confined in a tube-like region), a is the step length of primitive chain and b is bond length, respectively. It is convenient to express Eq. (2-13) in terms of molecular weight instead of the coefficients a and b. To do this, we can use the relation between a and b as [60]:

$$a^2 = \frac{4 M_e}{5 M_p} N b^2 \tag{2-14}$$

where M_e is the molecular weight between entanglement and M_p is the molecular weight of a polymer, respectively. Since $M = M_m N$ and $M_e / M_m = N_e$ where M_m denotes the molecular weight of each monomer and N_e represents the molecular chain length between entanglements, we can obtain the diffusion coefficient in the high molecular weight region by inserting Eq. (2-14) into Eq. (2-13) as:

$$D = \left(\frac{4}{15}\right)\left(\frac{k_B T N_e}{\zeta N^2}\right), \qquad N > N_c \tag{2-15}$$

The crossover in D from the Rouse theory to the reptation theory occurs at the critical polymer chain length, N_c. It is known that $N_c = 2N_e$. The value of N_c is material dependent and in the range of $30 \le N_c \le 120$ for typical thermoplastic and thermoset polymers. The diffusion of polymer chains starts to deviate slightly from Rouse behavior where $N \ge 30$ [65].

Substituting the diffusion coefficients in Eq. (2-11) with Eq. (2-12), one finds that the mobility for the low molecular weight system is given by:

$$M = \frac{v N_A N_B \Phi_A \Phi_B}{\zeta (N_A + N_B)(N_A \Phi_A + N_B \Phi_B)}, \qquad N < N_c \tag{2-16}$$

while for the high molecular weight region, the mobility M is found by inserting Eq. (2-15) into Eq. (2-11) to give:

$$M = \frac{4 v N_e N_A N_B \Phi_A \Phi_B}{15 \zeta (N_A^2 + N_B^2)(N_A \Phi_A + N_B \Phi_B)}, \qquad N > N_c \tag{2-17}$$

Note that ζ can be assumed to be the same for A and B segments [66].

For polymer solution, Chan [24] derived an expression for the κ parameter that is a function of the radius of gyration. They used de Gennes' [59] derivation that is appropriate for symmetric polymer blends, assuming that the effective interaction length between the molecules l_i is same with the radius of gyration:

$$\kappa = \frac{k_B T}{v} l_i^2 \chi = \frac{k_B T}{v} R_g^2 \chi \tag{2-18}$$

The radius of gyration R_g of a nonlinear polymer can be written in terms of polymer chain length of component *i* as [24]:

$$R_g = \left[g \frac{l_m^2}{6} n_m N \right]^{\frac{1}{2}} \tag{2-19}$$

where g is the ratio of the square radius of gyration of a branched molecule to that of a linear one of the same molecular weight, and is less than unity, n_m is the number of monomers, and l_m is length of each monomer, respectively.

In order to obtain an appropriate expression of κ for the mixed two components system, we can use the random phase approximation [67, 68]. Assuming n_m and l_m for each component A and B are identical, we arrive at [33, 34]:

$$\kappa = \kappa_0 \left(N_A + N_B \right) \tag{2-20}$$

where

$$\kappa_0 = \frac{k_B T}{12 v} \chi g l_m^2 n_m \tag{2-21}$$

Note that in Eq. (2-20), we neglect any concentration dependence of κ, because κ can be assumed to be constant as mentioned earlier. On the other hand, κ is proportional to the polymer chain lengths in Eq. (2-20). As the polymer chain grows, the interaction between the molecules increases. As shown below, Eq. (2-16), $(N<N_c)$, and Eq. (2-17) $(N>N_c)$, are used for M, and Eq. (2-20) is used for κ in Eq. (2-2) to derive the governing equation, respectively.

2.2.3 Polymerization Kinetics and Molecular Weight Distributions in Nonlinear Polymerization

In the PIPS method, the phase diagram continuously changes as molecular weight increases during polymerization. The rate of molecular weight increase is governed by its polymerization kinetics. The rate of polymerization also affects the morphology of mixtures such as droplet size [9, 10]. In addition, if the monomers are multi-functional, polymerization leads to the formation of branched polymers and three-dimensional network. In this study, we assumed that a monomer B undergoes the self-condensation polymerization in the presence of a non-reactive polymer A, and it is assumed that monomer B has three functional groups, B_3.

The kinetic rate equation for bimolecular of a single reactant is expressed as [69]:

$$\frac{dp}{dt} = k_1(1-p)^2 \tag{2-22}$$

where p is the extent of reaction, t is time and k_1 is the rate constant. Using the initial condition $p(t=0)=0$, the solution to Eq. (2-22) is:

$$p = \frac{k_1 t}{1+k_1 t} \tag{2-23}$$

The expressions for the number average $\overline{X}_n$ and the weight average $\overline{X}_w$ molecular sizes in terms of functionality have been derived by Stockmayer [70-72] for predicting the extent of reaction at the gel point. These expressions are obtained by assuming that the reactivity of all functional groups is the same and that there are no intramolecular reactions between functional groups [70-72], and are given by:

$$\overline{X}_n = \frac{1}{1-\alpha\gamma/2} \tag{2-24-a}$$

$$\overline{X}_w = \frac{1+\alpha}{1-(\gamma-1)\alpha} \tag{2-24-b}$$

where γ is the functionality of the monomer and α is the branching coefficient, defined as the probability that a given functional group of a branch unit leads to another branch unit [55]. Since the extent of reaction p at time t is given by the ratio of the number of functional groups that have reacted to the number of functional groups presented initially, for the single reactant system, α is equal to p. The gelation for a reactant of functionality γ can occur when at least one of the $(\gamma - 1)$ chain segments connect its branch unit to another branch unit. Thus, the critical branching coefficient can be defined as [73]:

$$\alpha_c = \frac{1}{\gamma - 1} \tag{2-25}$$

Eq. (2-25) is valid only for $\gamma > 2$, and when $\gamma = 3$, $\alpha_c = 0.5$. Because $\overline{X}_w$ is infinite while $\overline{X}_n$ has a finite value of 4, at the critical point ($\alpha_c = 0.5$), $\overline{X}_w$ better reflects the molecular weight growth of multi-functional units [33, 34]. By assuming N_B can be represented with $\overline{X}_w$ and combining Eq. (2-23) and Eq. (2-24-b), we can obtain for N_B as:

$$N_B = \frac{1 + 2k_1 t}{1 + 2k_1 t - \gamma\, k_1 t} \tag{2-26}$$

This value of N_B is used to determine the free energy function f in Eq. (2-3) and the mobility M in Eq. (2-2). Hence, the Gibbs free energy $f(t)$ and the mobility $M(t)$ are now time dependent functions.

2.3 Formulation of the Governing Equations of Polymerization-induced Phase Separation.

We assume that the initial system is located in the one-phase region and it is a homogenous-phase mixture consisting of two components, a polymer A with chain length N_A and a monomer B ($N_B = 1$) that has three functional groups. The condensation polymerization in the system induces the growth of N_B and leads to the formation of a branched polymer B. It is also assumed that only one constituent B undergoes polymerization, and a polymer A does not participate in this reaction and its molecular weight remains constant ($N_A = 100$). As N_B increases due to polymerization, the phase diagram changes continuously and shifts toward higher temperature and concentration (see Figure 1.7 (b)). As a result, the curing point is thrust into the unstable region, hence spinodal decomposition takes place during the polymerization process. Even though the system might pass through a metastable region before it reaches the unstable region, the phase separation phenomenon can be considered strictly as spinodal decomposition. Nucleation and growth (NG) can be skipped because of the fact that NG is a very slow and stochastic process [74].

2.3.1 Model Equation for the Non-Entanglement Region ($N < N_c$)

The model of spinodal decomposition is governed by the nonlinear Cahn-Hilliard theory given by Eq. (2-2). The time variation of the volume fraction field of polymer component A, $\Phi_A(x,y,t)$ in terms of the Flory-Huggins free energy function is given by:

$$\frac{\partial \Phi_A(x,y,t)}{\partial t} = \nabla\left[M(\Phi_A, N_A, N_B)\cdot\nabla\left(\frac{\partial f(\Phi_A)}{\partial \Phi_A} - 2\kappa\nabla^2\Phi_A\right)\right] \qquad (2\text{-}27)$$

where M is mobility given by Eq. (2-16) and Eq. (2-17) for two different molecular weight regime. Combining Eq. (2-27) with the F-H theory, Eq. (2-3), gives:

$$\frac{\partial \Phi_A(x,y,t)}{\partial t} = \nabla\left[M(\Phi_A, N_A, N_B)\cdot\nabla\left(\frac{k_B T}{v}\left[\frac{\ln\Phi_A}{N_A} + \frac{1}{N_A} - \frac{\ln(1-\Phi_A)}{N_B} - \frac{1}{N_B} + \chi(1-2\Phi_A)\right] - 2\kappa\nabla^2\Phi_A\right)\right] \qquad (2\text{-}28)$$

For the low molecular weight regime ($N < N_c$), or non-entanglement region, by inserting the mobility M given in Eq. (2-16) into Eq. (2-28) and performing the functional derivative, Eq. (2-28) is rewritten as:

$$\frac{\partial \Phi_A(x,y,t)}{\partial t} = \frac{k_B T}{\zeta(N_A + N_B)}\Bigg[\frac{-N_B(N_A\Phi_A + N_B(1-\Phi_A)) - N_B(N_A - N_B)(1-\Phi_A)}{(N_A\Phi_A + N_B(1-\Phi_A))^2} + \frac{N_A(N_A\Phi_A + N_B(1-\Phi_A)) - N_A(N_A - N_B)\Phi_A}{(N_A\Phi_A + N_B(1-\Phi_A))^2} \qquad (2\text{-}29)$$

$$
-2\chi\frac{N_A N_B\left(N_A\Phi_A+N_B(1-\Phi_A)\right)(1-2\Phi_A)-N_A N_B(N_A-N_B)\Phi_A(1-\Phi_A)}{\left(N_A\Phi_A+N_B(1-\Phi_A)\right)^2}\Bigg]
$$

$$
\left(\frac{\partial\Phi_A}{\partial x}\frac{\partial\Phi_A}{\partial x}+\frac{\partial\Phi_A}{\partial y}\frac{\partial\Phi_A}{\partial y}\right)+\frac{k_B T}{\zeta(N_A+N_B)}\left[\frac{N_B(1-\Phi_A)}{N_A\Phi_A+N_B(1-\Phi_A)}\right.
$$

$$
\left.+\frac{N_A\Phi_A}{N_A\Phi_A+N_B(1-\Phi_A)}-2\chi\frac{N_A N_B\Phi_A(1-\Phi_A)}{N_A\Phi_A+N_B(1-\Phi_A)}\right]\left(\frac{\partial^2\Phi_A}{\partial x^2}+\frac{\partial^2\Phi_A}{\partial y^2}\right)
$$

$$
-\frac{2\kappa\nu}{\zeta(N_A+N_B)}\frac{N_A N_B\left(N_A\Phi_A+N_B(1-\Phi_A)\right)(1-2\Phi_A)-N_A N_B(N_A-N_B)\Phi_A(1-\Phi_A)}{\left(N_A\Phi_A+N_B(1-\Phi_A)\right)^2}
$$

$$
\left(\frac{\partial^3\Phi_A}{\partial x^3}\frac{\partial\Phi_A}{\partial x}+\frac{\partial^3\Phi_A}{\partial x\partial y^2}\frac{\partial\Phi_A}{\partial x}+\frac{\partial^3\Phi_A}{\partial x^2\partial y}\frac{\partial\Phi_A}{\partial y}+\frac{\partial^3\Phi_A}{\partial y^3}\frac{\partial\Phi_A}{\partial y}\right)
$$

$$
-\frac{2\kappa\nu N_A N_B\Phi_A(1-\Phi_A)}{\zeta(N_A+N_B)\left(N_A\Phi_A+N_B(1-\Phi_A)\right)}\left(\frac{\partial^4\Phi_A}{\partial x^4}+2\frac{\partial^4\Phi_A}{\partial x^2\partial y^2}+\frac{\partial^4\Phi_A}{\partial y^4}\right)
$$

For convenience, it is assumed that the degree of polymerization N_A and N_B are always monodisperse and Flory's interaction parameter χ given in Eq. (2-4) is temperature dependent only. The system will be restricted to a two-dimensional square of length L in this study.

Eq. (2-29) can be written in dimensionless form by suitable rescaling. The following dimensionless variables are used: $x^* = x/L$, $y^* = y/L$, $T^* = T/\Theta$, $t^* = 2\kappa_0 \nu t / L^4\zeta$, and $D^* = k_B\Theta L^2/2\nu\kappa_0$. Therefore, Eq. (2-29) can be rewritten as:

$$
\frac{\partial\Phi_A^*(x,y,t)}{\partial t^*}=\frac{D^*T^*}{(N_A+N_B)}\left[\frac{-N_B\left(N_A\Phi_A^*+N_B(1-\Phi_A^*)\right)-N_B(N_A-N_B)(1-\Phi_A^*)}{\left(N_A\Phi_A^*+N_B(1-\Phi_A^*)\right)^2}\right.
$$

$$
+\frac{N_A\left(N_A\Phi_A^*+N_B(1-\Phi_A^*)\right)-N_A(N_A-N_B)\Phi_A^*}{\left(N_A\Phi_A^*+N_B(1-\Phi_A^*)\right)^2} \tag{2-30}
$$

$$
\left.-2\chi\frac{N_A N_B\left(N_A\Phi_A^*+N_B(1-\Phi_A^*)\right)(1-2\Phi_A^*)-N_A N_B(N_A-N_B)\Phi_A^*(1-\Phi_A^*)}{\left(N_A\Phi_A^*+N_B(1-\Phi_A^*)\right)^2}\right]
$$

$$
\left(\frac{\partial\Phi_A^*}{\partial x^*}\frac{\partial\Phi_A^*}{\partial x^*}+\frac{\partial\Phi_A^*}{\partial y^*}\frac{\partial\Phi_A^*}{\partial y^*}\right)+\frac{D^*T^*}{(N_A+N_B)}\left[\frac{N_B(1-\Phi_A^*)}{N_A\Phi_A^*+N_B(1-\Phi_A^*)}\right.
$$

$$
+\frac{N_A\Phi_A^*}{N_A\Phi_A^*+N_B(1-\Phi_A^*)}-2\chi\frac{N_AN_B\Phi_A^*(1-\Phi_A^*)}{N_A\Phi_A^*+N_B(1-\Phi_A^*)}\Bigg]\left(\frac{\partial^2\Phi_A^*}{\partial x^{*2}}+\frac{\partial^2\Phi_A^*}{\partial y^{*2}}\right)
$$

$$
-\frac{N_AN_B\left(N_A\Phi_A^*+N_B(1-\Phi_A^*)\right)(1-2\Phi_A^*)-N_AN_B(N_A-N_B)\Phi_A^*(1-\Phi_A^*)}{\left(N_A\Phi_A^*+N_B(1-\Phi_A^*)\right)^2}
$$

$$
\left(\frac{\partial^3\Phi_A^*}{\partial x^{*3}}\frac{\partial\Phi_A^*}{\partial x^*}+\frac{\partial^3\Phi_A^*}{\partial x^*\partial y^{*2}}\frac{\partial\Phi_A^*}{\partial x^*}+\frac{\partial^3\Phi_A^*}{\partial x^{*2}\partial y^*}\frac{\partial\Phi_A^*}{\partial y^*}+\frac{\partial^3\Phi_A^*}{\partial y^{*3}}\frac{\partial\Phi_A^*}{\partial y^*}\right)
$$

$$
-\frac{N_AN_B\Phi_A^*(1-\Phi_A^*)}{\left(N_A\Phi_A^*+N_B(1-\Phi_A^*)\right)}\left(\frac{\partial^4\Phi_A^*}{\partial x^{*4}}+2\frac{\partial^4\Phi_A^*}{\partial x^{*2}\partial y^{*2}}+\frac{\partial^4\Phi_A^*}{\partial y^{*4}}\right)
$$

where the superscripted asterisks denote dimensionless variables.

2.3.2 Model Equation for the Entanglement Region ($N > N_c$)

The physical properties of a polymer such as viscosity, modulus and diffusion coefficient dramatically change when its molecular weight exceeds a certain critical value, N_c. This change is due to the entanglement effect of polymer molecules. The governing equation for high molecular weight region can be obtained by inserting Eq. (2-17) into Eq. (2-28), reflecting the entanglement effect. After performing functional derivative, Eq. (2-28) gives:

$$
\begin{aligned}
\frac{\partial\Phi_A(x,y,t)}{\partial t}=\frac{4\,k_BT\,N_e}{15\,\zeta(N_A^2+N_B^2)}\Bigg[&\frac{-N_B\left(N_A\Phi_A+N_B(1-\Phi_A)\right)-N_B(N_A-N_B)(1-\Phi_A)}{\left(N_A\Phi_A+N_B(1-\Phi_A)\right)^2}\\
&+\frac{N_A\left(N_A\Phi_A+N_B(1-\Phi_A)\right)-N_A(N_A-N_B)\Phi_A}{\left(N_A\Phi_A+N_B(1-\Phi_A)\right)^2}\\
&-2\chi\frac{N_AN_B\left(N_A\Phi_A+N_B(1-\Phi_A)\right)(1-2\Phi_A)-N_AN_B(N_A-N_B)\Phi_A(1-\Phi_A)}{\left(N_A\Phi_A+N_B(1-\Phi_A)\right)^2}\Bigg]\\
&\left(\frac{\partial\Phi_A}{\partial x}\frac{\partial\Phi_A}{\partial x}+\frac{\partial\Phi_A}{\partial y}\frac{\partial\Phi_A}{\partial y}\right)+\frac{4\,k_BT\,N_e}{15\,\zeta(N_A^2+N_B^2)}\Bigg[\frac{N_B(1-\Phi_A)}{N_A\Phi_A+N_B(1-\Phi_A)}\\
&+\frac{N_A\Phi_A}{N_A\Phi_A+N_B(1-\Phi_A)}-2\chi\frac{N_AN_B\Phi_A(1-\Phi_A)}{N_A\Phi_A+N_B(1-\Phi_A)}\Bigg]\left(\frac{\partial^2\Phi_A}{\partial x^2}+\frac{\partial^2\Phi_A}{\partial y^2}\right)
\end{aligned}
\tag{2-31}
$$

$$-\frac{8\kappa\nu N_e}{15\ \zeta(N_A^2+N_B^2)}\frac{N_AN_B(N_A\Phi_A+N_B(1-\Phi_A))(1-2\Phi_A)-N_AN_B(N_A-N_B)\Phi_A(1-\Phi_A)}{(N_A\Phi_A+N_B(1-\Phi_A))^2}$$

$$\left(\frac{\partial^3\Phi_A}{\partial x^3}\frac{\partial\Phi_A}{\partial x}+\frac{\partial^3\Phi_A}{\partial x\partial y^2}\frac{\partial\Phi_A}{\partial x}+\frac{\partial^3\Phi_A}{\partial x^2\partial y}\frac{\partial\Phi_A}{\partial y}+\frac{\partial^3\Phi_A}{\partial y^3}\frac{\partial\Phi_A}{\partial y}\right)$$

$$-\frac{8\kappa\nu N_AN_BN_e\Phi_A(1-\Phi_A)}{15\ \zeta(N_A^2+N_B^2)(N_A\Phi_A+N_B(1-\Phi_A))}\left(\frac{\partial^4\Phi_A}{\partial x^4}+2\frac{\partial^4\Phi_A}{\partial x^2\partial y^2}+\frac{\partial^4\Phi_A}{\partial y^4}\right)$$

Using the same scaling variables used in Eq. (2-30), we can rewrite Eq. (2-31) as:

$$\begin{aligned}
\frac{\partial\Phi_A^*(x,y,t)}{\partial t^*}=\frac{4\ D^*T^*N_e}{15\ (N_A^2+N_B^2)}\Bigg[&\frac{-N_B(N_A\Phi_A^*+N_B(1-\Phi_A^*))-N_B(N_A-N_B)(1-\Phi_A^*)}{(N_A\Phi_A^*+N_B(1-\Phi_A^*))^2}\\
&+\frac{N_A(N_A\Phi_A^*+N_B(1-\Phi_A^*))-N_A(N_A-N_B)\Phi_A^*}{(N_A\Phi_A^*+N_B(1-\Phi_A^*))^2}\\
&-2\chi\frac{N_AN_B(N_A\Phi_A^*+N_B(1-\Phi_A^*))(1-2\Phi_A^*)-N_AN_B(N_A-N_B)\Phi_A^*(1-\Phi_A^*)}{(N_A\Phi_A^*+N_B(1-\Phi_A^*))^2}\Bigg]\\
&\left(\frac{\partial\Phi_A^*}{\partial x^*}\frac{\partial\Phi_A^*}{\partial x^*}+\frac{\partial\Phi_A^*}{\partial y^*}\frac{\partial\Phi_A^*}{\partial y^*}\right)+\frac{4\ D^*T^*N_e}{15\ (N_A^*+N_B^*)}\Bigg[\frac{N_B(1-\Phi_A^*)}{N_A\Phi_A^*+N_B(1-\Phi_A^*)}\\
&+\frac{N_A\Phi_A^*}{N_A\Phi_A^*+N_B(1-\Phi_A^*)}-2\chi\frac{N_AN_B\Phi_A^*(1-\Phi_A^*)}{N_A\Phi_A^*+N_B(1-\Phi_A^*)}\Bigg]\left(\frac{\partial^2\Phi_A^*}{\partial x^{*2}}+\frac{\partial^2\Phi_A^*}{\partial y^{*2}}\right)\\
&-\frac{4\ N_e(N_A+N_B)}{15\ (N_A^2+N_B^2)}\frac{N_AN_B(N_A\Phi_A^*+N_B(1-\Phi_A^*))(1-2\Phi_A^*)-N_AN_B(N_A-N_B)\Phi_A^*(1-\Phi_A^*)}{(N_A\Phi_A^*+N_B(1-\Phi_A^*))^2}\\
&\left(\frac{\partial^3\Phi_A^*}{\partial x^{*3}}\frac{\partial\Phi_A^*}{\partial x^*}+\frac{\partial^3\Phi_A^*}{\partial x^*\partial y^{*2}}\frac{\partial\Phi_A^*}{\partial x^*}+\frac{\partial^3\Phi_A^*}{\partial x^{*2}\partial y^*}\frac{\partial\Phi_A^*}{\partial y^*}+\frac{\partial^3\Phi_A^*}{\partial y^{*3}}\frac{\partial\Phi_A^*}{\partial y^*}\right)\\
&-\frac{4\ N_e(N_A+N_B)}{15\ (N_A^2+N_B^2)}\frac{N_AN_B\Phi_A^*(1-\Phi_A^*)}{(N_A\Phi_A^*+N_B(1-\Phi_A^*))}\left(\frac{\partial^4\Phi_A^*}{\partial x^{*4}}+2\frac{\partial^4\Phi_A^*}{\partial x^{*2}\partial y^{*2}}+\frac{\partial^4\Phi_A^*}{\partial y^{*4}}\right)
\end{aligned}\qquad(2\text{-}32)$$

To determine the crossover point from the non-entanglement regime to the entanglement regime, the values of N_e for typical thermoset polymers are given as follows: N_e(PMMA) ≅ 100, N_e(PSF: alternating copolymer of Bisphenol A and dichlorodiphenyl sulfone) ≅ 20 [75]. Recall that $N_c \cong 2N_e$. Because N_c is a material dependent value, the crossover point from the non-entanglement regime (Eq. 2-30) to the entanglement regime (Eq. 2.32) would vary depending on the materials used. In this study, it is assumed that $N_{c,A} > 100$ and $N_{c,B} = 31.5$. Since component A does not participate in the reaction, remaining constant molecular weight ($N_A = 100$), the model equation governed by Rouse theory (Eq. (2-30)) is used from $t^* = 0$ to $t^*(N_B = 31.5)$ and it is switched to the equation governed by reptation theory (Eq. (2-32)) for $t^* > t^*(N_B = 31.5)$.

The value of N_B in Eqs. (2-30) and (2-32) is determined by Eq. (2-26) to describe polymerization process. Eq. (2-26) also can be written in dimensionless form as:

$$N_B = \frac{1 + 2K^* t^*}{1 + 2K^* t^* - \gamma K^* t^*} \tag{2-33}$$

where K^* is the dimensionless reaction rate constant defined by:

$$K^* = \frac{k_1 L^4 \zeta}{2\kappa_0 \nu} \tag{2-34}$$

In Eq. (2-33), if $t^* = 0$, $N_B = 1$, and if $t^* \to \infty$, $N_B \to \infty$ and gelation occurs

2.3.3 Initial and Boundary Conditions

To solve the governing dimensionless equations given in Eq. (2-30) and Eq. (2-32), four boundary conditions and one initial condition for each equation are required. A set of natural boundary conditions can be used for solution of Eq. (2-30) and Eq. (2-32) which is written as:

$$\left(\nabla \Phi_A^*\right) \cdot \vec{n} = 0 \tag{2-35}$$

where $\vec{n}$ is the outward unit normal vector to a bounding surface. Therefore, the first set of dimensionless boundary equations are given by:

$$\frac{\partial \Phi^*_A}{\partial x^*} = 0 \quad , \qquad \text{at } t^* > 0,\ \text{and } x^* = 0 \ \text{ and } \ x^* = 1 \tag{2-36-a}$$

$$\frac{\partial \Phi^*_A}{\partial y^*} = 0 \quad , \qquad \text{at } t^* > 0,\ \text{and } y^* = 0 \ \text{ and } \ y^* = 1 \tag{2-36-b}$$

The other set of boundary conditions can be obtained by the fact that there is no mass flux with the surroundings [49]. By setting the mass flux $\bar{J}$ to zero, Elliott and Songmu [76] derived the zero mass flux boundary conditions as:

$$\bar{J} = -M\nabla\left(\frac{\partial f(\Phi^*_A)}{\partial \Phi^*_A} - 2\kappa\nabla^2\Phi^*_A\right) = 0 \tag{2-37}$$

Thus, the second set of dimensionless boundary conditions are written as [49]:

$$\frac{\partial^3 \Phi^*_A}{\partial x^{*3}} + \frac{\partial^3 \Phi^*_A}{\partial x^* \partial y^{*2}} = 0 \quad , \qquad \text{at } t^* > 0,\ \text{and } x^* = 0 \ \text{ and } \ x^* = 1 \tag{2-38-a}$$

$$\frac{\partial^3 \Phi^*_A}{\partial y^{*3}} + \frac{\partial^3 \Phi^*_A}{\partial y^* \partial x^{*2}} = 0 \quad , \qquad \text{at } t^* > 0,\ \text{and } y^* = 0 \ \text{ and } \ y^* = 1 \tag{2-38-b}$$

The infinitesimal concentration deviations from the average concentration are always present initially even in the homogeneous one-phase mixture. These deviations are called homophase thermal concentration fluctuations. The infinitesimal thermal concentration fluctuations must be reflected in the initial condition as:

$$\Phi^*_A(x^*, y^*, t^* = 0) = \Phi^*_{A0} + \delta\,\Phi^*_A(x^*, y^*, t^* = 0) \tag{2-39}$$

where Φ^*_{A0} is the average concentration. Chan et al [33, 34, 49] used a linearization approximation to describe the thermal concentration fluctuations $\delta\,\Phi^*_A$ by retaining only linear terms in their equation. Then they decomposed the free energy function into its Fourier components and applied the equipartition theorem. This approximation is plausible because the homophase concentration fluctuations in the very early stages of the phase separation are infinitesimal. Thus, their approximation and expression for $\delta\,\Phi^*_A$ are employed to describe the thermal concentration fluctuation in this study.

In summary, from $t^* = 0$ to $t^* = t_c^*(N_B = 31.5)$, Eqs. (2-30) and (2-33) are solved with four sets of boundary conditions given in Eqs. (2-36-a), (2-36-b), (2-38-a) and (2-38-b), and an initial condition given in Eq. (2-39). At $t^* > t_c^*$, Eqs. (2-32) and (2-33) are solved with the same boundary conditions used for $t^* < t_c^*$. In addition, the solutions of Eq. (2-30) at $t_c^*(N_B = 31.5)$ are used as the initial condition for Eq. (2-32). The dependent variables are Φ_A^* and N_B, and the independent variables are x^*, y^* and t^*. While there is an analytical solution to the equation describing the polymerization process (Eq. (2-33)), there is none for phase separation process (Eqs. (2-30) and (2-32)). Thus, Eqs. (2-30) and (2-32) with their auxiliary conditions must be solved numerically to obtain the solution vector for $\Phi_A^*(x^*, y^*, t^*)$. The parameters are the dimensionless diffusion coefficient D^*, the dimensionless rate constant K^*, the dimensionless initial average concentration $\Phi_{A,0}^*$, the dimensionless temperature T^*, and the Flory-Huggins interaction parameter χ. The temperature dependence of χ is given in Eq. (2-4).

2.4 Methods of Solution

2.4.1 Galerkin Finite Elements Method and Hermitian Basis Functions

The Galerkin finite elements method (GFEM) has been widely used for solving problems governed by ordinary differential equations, partial differential equations and integral equations in many applications [77, 78]. When we suppose that the given differential equation with appropriate initial condition and boundary conditions for two dimensional problem is expressed as:

$$L(u) = 0 \qquad a \le x \le b, \qquad a \le y \le b \tag{2-40}$$

then, an approximate solution u_a can be assumed to be written as:

$$u_a(x,y,t)=\sum_{j=1}^{N}u_j(t)\varphi^j(x,y) \tag{2-41}$$

where φ^j 's are known analytic functions, called global trial and test functions, and u_j 's are time dependent unknown coefficients. Replacing u in Eq. (2-40) with u_a in Eq. (2-41), we can obtain the following expression:

$$L(u_a)=R\neq 0 \tag{2-42}$$

where R is the residual. An approximate solution u_a is assumed to be represented in a piecewise approximate function, so that if this piecewise approximation is correctly constructed, then it will approach the corresponding exact solution u. In other words, the aim of method of residual is to force R to zero and consequently to make an approximate solution u_a approach the exact solution. To do this, we need to set the inner product of the residual R and an independent weight function w_i equal to zero:

$$F_i=\iint_A R\ w_i(x,y)dA=\iint_A L(u_a)\ w_i(x,y)dA=0 \tag{2-43}$$

In the Gakerkin method, the weight function w_i is chosen from the same family of function in Eq. (2-41), hence, Eq. (2-43) can be rewritten as:

$$F_i=\iint_A R\ \varphi^i(x,y)dA=\iint_A L(u_a)\ \varphi^i(x,y)dA=0 \tag{2-44}$$

where $i,\ j=1,2,\ldots N$. We can note that Eq. (2-44) can be expressed as a set of N differential equations to be solved for the unknown coefficients u_a when we use the Gaussian integration. Consequently, Eq. (2-40) has been reduced to a set of ordinary differential equations (2-44).

In this study, the given differential equation $L(u_a)$ is the fourth-order two-dimensional partial differential equation (see Eq. (2-30) and Eq. (2-32)) given by:

$$L(u_a)=\frac{\partial u_a}{\partial t}-F(u_a)\nabla u_a\cdot\nabla u_a-G(u_a)\nabla^2 u_a+H(u_a)\nabla u_a\cdot\nabla(\nabla^2 u_a)+I(u_a)\nabla^4 u_a=0 \tag{2-45}$$

where $\nabla=(\partial/\partial x)\vec{i}+(\partial/\partial y)\vec{j}$. Inserting Eq. (2-45) into Eq. (2-44) leads the residual equation as:

$$F_i=\int_a^b\!\!\int_a^b\left[\frac{\partial u_a}{\partial t}-F(u_a)\nabla u_a\cdot\nabla u_a-G(u_a)\nabla^2 u_a+H(u_a)\nabla u_a\cdot\nabla(\nabla^2 u_a)+I(u_a)\nabla^4 u_a\right]\varphi^i\,dxdy \quad (2\text{-}46)$$

To lower the order of the derivatives of Eq. (2-46), we can use the divergence theorem. For a scalar α and vector $\vec{v}$:

$$\int_V \alpha\nabla\cdot\vec{v}\,dV=\int_S \alpha\vec{n}\cdot\vec{v}\,dS-\int_V \nabla\alpha\cdot\vec{v}\,dV \quad (2\text{-}47)$$

where S is the boundary of the domain V, and $\vec{n}$ is the outward unit normal vector. Using the divergence theorem twice and the vector differential identity [79]:

$$\nabla^3\alpha\cdot\nabla\gamma=\nabla\cdot\left[(\nabla^2\alpha)(\nabla^2\gamma)\right]-\nabla^2\alpha\nabla^2\gamma \quad (2\text{-}48)$$

we can rewrite the fourth order terms in Eq. (2-46) as:

$$\begin{aligned}\int_a^b\!\!\int_a^b H(u_a)\varphi^i\left[\nabla u_a\cdot\nabla(\nabla^2 u_a)\right]dxdy&=\int_S H(u_a)\varphi^i\vec{n}\cdot\left[(\nabla^2 u_a)(\nabla u_a)\right]dS-\int_a^b\!\!\int_a^b\nabla\left[H(u_a)\varphi^i\right]\cdot\left[(\nabla^2 u_a)(\nabla u_a)\right]dxdy\\&\quad-\int_a^b\!\!\int_a^b H(u_a)\varphi^i\left[(\nabla^2 u_a)(\nabla^2 u_a)\right]dxdy \qquad (2\text{-}49\text{-}a)\end{aligned}$$

and

$$\begin{aligned}\int_a^b\!\!\int_a^b I(u_a)\varphi^i\nabla^4 u_a\,dxdy&=\int_S I(u_a)\varphi^i\vec{n}\cdot\nabla^3 u_a\,dS-\int_S\vec{n}\cdot(\nabla^2 u_a)\nabla\left[I(u_a)\varphi^i\right]dS\\&\quad+\int_a^b\!\!\int_a^b(\nabla^2 u_a)\nabla^2\left[I(u_a)\varphi^i\right]dxdy \qquad (2\text{-}49\text{-}b)\end{aligned}$$

Finally, Eq. (2-46) can be expressed as governing terms and three boundary terms as:

$$\begin{aligned}F_i&=\int_a^b\!\!\int_a^b\left[\frac{\partial u_a}{\partial t}-F(u_a)\nabla u_a\cdot\nabla u_a-G(u_a)\nabla^2 u_a\right]\varphi^i\,dxdy\\&\quad-\int_a^b\!\!\int_a^b\left[\nabla\left[H(u_a)\varphi^i\right]\cdot\left[(\nabla^2 u_a)(\nabla u_a)\right]+H(u_a)\varphi^i\left[(\nabla^2 u_a)(\nabla^2 u_a)\right]-(\nabla^2 u_a)\left[\nabla^2\left[I(u_a)\varphi^i\right]\right]\right]dxdy \qquad (2\text{-}50)\\&\quad+\int_S H(u_a)\varphi^i\vec{n}\cdot\left[(\nabla^2 u_a)(\nabla u_a)\right]dS+\int_S I(u_a)\varphi^i\vec{n}\cdot\nabla^3 u_a\,dS-\int_S\vec{n}\cdot(\nabla^2 u_a)\left[\nabla\left[I(u_a)\varphi^i\right]\right]dS\end{aligned}$$

Once the governing equation has been set in Galerkin form, the next step is discretization, that is, the domain must be divided into a number of finite elements. Note that for one-dimensional problem each element has two nodes, thus if there are N elements, N+1 nodes exist. For two-dimensional problems, either triangles or rectangles can be used for elements, depending on the boundary geometry. The number of nodes has to be properly chosen to represent the solution more effectively where rapid changes in the solution are expected. Balance between the number of elements and computational time and memory space should be also taken into account.

As shown in Eq. (2-41), an approximate solution has been expressed as the summation of the product of unknown coefficient $u_j(t)$ and the global trial and test function $\varphi^j(x,y)$. However, in computations, by using the local test and trial functions instead of the global test and trial function, the given problems can be solved very economically. This is plausible because the test and trial functions span a very small section of the spatial domain. The test and trial functions are nonzero only in the immediate vicinity of the j-th node and zero outside of this range. A schematic representation of two-dimensional global and local domains is shown in Figure 2.1, where ξ and η represent the local orthogonal coordinate system. Note that u_i defined at the local level is identical to $u^{e,j}$ at the global level where the subscript index represents the local level and the superscript index implies the global level. So thus in each element, we obtain that:

$$u(\xi,\eta)=\sum_{j=1}^{4} u_{e,j}\varphi_j(\xi,\eta) \tag{2-51}$$

where φ_j is the local basis function.

Once the locations of the nodes have been determined, the appropriate nodal basis functions have to be selected. Hermitian cubic basis functions are known to be appropriate for the forth-order partial differential equations [80]. In Hermite interpolation both function values and derivatives are interpolated at the ends of each element. Therefore, in one dimension, each element has two double nodes and four basis functions. Using the following features of the Hermitian basis functions:

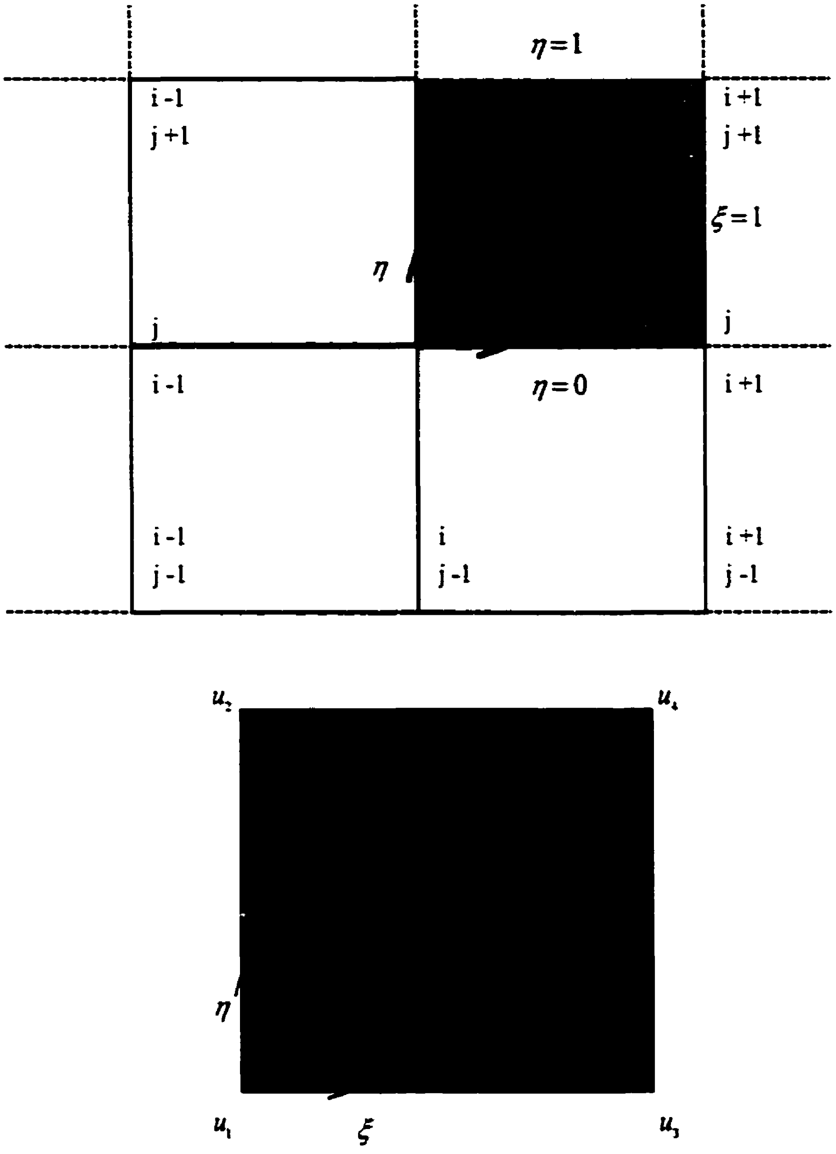

Figure 2.1 Element configurations in a two-dimensional global domain and corresponding local domain. x and y represent the global two-dimensional coordinate axes while ξ and η represent the local coordinate axes. Note that u_1 defined at the local domain becomes $u_{i,j}$ at the global domain.

$$\varphi_{1,0}(0)=\varphi_{2,0}(1)=1 \qquad \text{(2-52-a)}$$

$$\varphi_{1,0}(1)=\varphi_{2,0}(0)=0 \qquad \text{(2-52-b)}$$

$$\frac{d\varphi_{1,0}}{d\xi}(0)=\frac{d\varphi_{1,0}}{d\xi}(1)=\frac{d\varphi_{2,0}}{d\xi}(0)=\frac{d\varphi_{2,0}}{d\xi}(1)=0 \qquad \text{(2-52-c)}$$

$$\varphi_{1,1}(0)=\varphi_{1,1}(1)=\varphi_{2,1}(0)=\varphi_{2,1}(1)=0 \qquad \text{(2-52-d)}$$

$$\frac{d\varphi_{1,1}}{d\xi}(0)=\frac{d\varphi_{2,1}}{d\xi}(1)=1 \qquad \text{(2-52-e)}$$

$$\frac{d\varphi_{1,1}}{d\xi}(1)=\frac{d\varphi_{2,1}}{d\xi}(0)=0 \qquad \text{(2-52-f)}$$

we can construct the Hermitian cubic basis functions as:

$$\varphi_{1,0}=1-3\xi^2+2\xi^3 \qquad \text{(2-53-a)}$$

$$\varphi_{1,1}=\xi-2\xi^2+\xi^3 \qquad \text{(2-53-b)}$$

$$\varphi_{2,0}=3\xi^2-2\xi^3 \qquad \text{(2-53-c)}$$

$$\varphi_{2,1}=-\xi^2+\xi^3 \qquad \text{(2-53-e)}$$

where $\varphi_{j,0}$ interpolate the function values and $\varphi_{j,1}$ interpolate their derivatives. Hence, the Hermitian cubic expansion based on local domain can be written as:

$$u(\xi)=\sum_{j=1}^{2}u_j\varphi_{j,0}(\xi)+\sum_{j=1}^{2}\frac{du_j}{dx}\varphi_{j,1}(\xi) \qquad \text{(2-54)}$$

By means of mapping $\xi\rightarrow x$, the approximate solution of the global domain has the form:

$$u_e=\sum_{j=1}^{N}\left[u_j\varphi_0^j+\frac{du_j}{dx}\varphi_1^j\right] \qquad \text{(2-55)}$$

On the other hand, for two dimensional problem, each element has four sets of four nodes and 16 basis functions. Thus introducing $\varphi_{j,0}(\xi,\eta)$ and $\varphi_{j,1}(\xi,\eta)$ in the orthogonal coordinate (ξ,η), Eq. (2-54) and (2-55) have to be rewritten as:

$$u(\xi,\eta)=\sum_{j=1}^{4}u_j\varphi_{j,0}(\xi,\eta)+\sum_{j=1}^{4}\left(\frac{\partial u_j}{\partial\xi}\right)\varphi_{j,1}(\xi,\eta)+\sum_{j=1}^{4}\left(\frac{\partial u_j}{\partial\eta}\right)\varphi_{j,2}(\xi,\eta)+\sum_{j=1}^{4}\left(\frac{\partial^2 u_j}{\partial\xi\partial\eta}\right)\varphi_{j,3}(\xi,\eta) \qquad \text{(2-56)}$$

and

$$u_s = \sum_{j=1}^{N} \left(u_j \varphi_0^j + \frac{\partial u_j}{\partial x} \varphi_1^j + \frac{\partial u_j}{\partial y} \varphi_2^j + \frac{\partial^2 u_j}{\partial x \partial y} \varphi_3^j \right) \qquad \text{(2-57)}$$

where $\varphi_{j,0}$ interpolates the function values and $\varphi_{j,1}$, $\varphi_{j,2}$, and $\varphi_{j,3}$ interpolate their derivatives with respect to ξ, η. It is much convenient way to lump the coefficient in Eq. (2-57) together as U_j and the Hermitian basis functions together as ψ_j [48], which gives:

$$u_s = \sum_{j=1}^{4N} U_j \psi_j \qquad \text{(2-58)}$$

where

$$U_j = u_k,\ \psi_j = \varphi_0^k \qquad \text{for} \begin{pmatrix} j = 1,\ 5,\ 9,\ 13,\ \ldots,\ 4N-3 \\ \\ k = 1,\ 2,\ 3,\ 4,\ \ldots,\ N \end{pmatrix} \qquad \text{(2-59-a)}$$

$$U_j = \frac{\partial u_k}{\partial x},\ \psi_j = \varphi_1^k \qquad \text{for} \begin{pmatrix} j = 2,\ 6,\ 10,\ 14,\ \ldots,\ 4N-2 \\ \\ k = 1,\ 2,\ 3,\ 4,\ \ldots,\ N \end{pmatrix} \qquad \text{(2-59-b)}$$

$$U_j = \frac{\partial u_k}{\partial y},\ \psi_j = \varphi_2^k \qquad \text{for} \begin{pmatrix} j = 3,\ 7,\ 11,\ 15,\ \ldots,\ 4N-1 \\ \\ k = 1,\ 2,\ 3,\ 4,\ \ldots,\ N \end{pmatrix} \qquad \text{(2-59-c)}$$

$$U_j = \frac{\partial^2 u_k}{\partial x \partial y},\ \psi_j = \varphi_3^k \qquad \text{for} \begin{pmatrix} j = 4,\ 8,\ 12,\ 16,\ \ldots,\ 4N \\ \\ k = 1,\ 2,\ 3,\ 4,\ \ldots,\ N \end{pmatrix} \qquad \text{(2-59-d)}$$

Inserting Eq. (2-58) into Eq. (2-50) and applying the boundary conditions, we can obtain an equation in a matrix form:

$$\underline{\underline{J}} \cdot \underline{U} = -\underline{F} \qquad \text{(2-60)}$$

where $\underline{\underline{J}}$ is the Jacobian matrix which can be determined by $J_{i,j} = \partial F_i / \partial U_j$ and F_i is given in Eq. (2-50). Finally Eq. (2-60) is solved for the unknown coefficient U_j using a Newton-Raphson iteration scheme. Convergence is assumed when the length of the vector of the difference of two successive computed solution vectors is less than 10^{-6}.

2.4.2 Time Integration Methods

The nonlinear time-dependent partial differential equations given in Eq. (2-50) have been reduced to a set of ordinary time-dependent differential equations. The finite difference method and a first-order implicit Euler predictor-corrector method are used for time discretization [81]. In addition, an adaptive time step control method [81] is used to minimize computing time while maintaining accuracy.

2.5 Conclusions

A theoretical model was developed to describe the phase separation phenomena during polymerization of a monomer B in the presence of a polymer A. During polymerization takes place, the phase diagram of the two component mixture A and B continuously moves toward higher temperature and concentration. The curing point initially located in the homogeneous phase region is thrust into the unstable region, and phase separation occurs via spinodal decomposition. The nonlinear Cahn-Hilliard theory and the Flory-Huggins theory were used to develop a model of spinodal decomposition. The local concentration and molecular weight dependent mobility was derived to reflect the molecular dynamics in the multi-component polymeric system. The two different diffusion theories, the Rouse theory and the reptation theory, were used for mobility to reflect the different molecular behavior with an entanglement effect. Therefore, two governing equations were developed for the non-entanglement regime and for the entanglement regime, respectively, for one reaction operation. The sets of zero mass flux and natural boundary conditions were formulated as non-periodic boundary conditions. The infinitesimal thermal concentration fluctuations present in an initial homogeneous mixture implemented to reflect better initial conditions. The Galerkin finite element method with Hermitian bicubic interpolants was chosen for spatial discretization of the governing equations. In addition, a first-order implicit Euler predictor-corrector method and an adaptive time scheme were used to perform temporal discretization. In summary, a full model for the PIPS method and its method of solutions, based on GFEM and corrector/predictor method, have been developed.

Chapter 3

Computational Simulation and Morphological Analysis of Polymerization-induced Phase Separation

Summary

A rigorous model of polymerization-induced phase separation (PIPS), based on the nonlinear Cahn-Hilliard (C-H) and Flory-Huggins (F-H) theories combined with a second-order polymerization reaction equation, has been formulated. The model describes phase separation in system consisting of a non-reactive polymer and a monomer that undergoes condensation polymerization. The model consists of a balance equation for the low molecular weight regime and another balance equation for the high molecular weight entangled region. The model equations are solved, and the solutions are characterized to identify the dynamical and morphological phenomena of the PIPS process. The extent of phase separation increases with time significantly during the early stage of phase separation, and slows down in the intermediate stage. The various types of the phase-separated morphologies are fully characterized using the novel morphological characterization techniques, known as the intensity and scale of segregation. Both the dynamical and morphological features of the PIPS method are sensitive to the magnitudes of the dimensionless diffusion coefficient D^* and the dimensionless reaction rate constant K^*. The scale of segregation and the droplet size decrease as D^* and K^* increase. On the other hand, the intensity of segregation increases with K^*, but decreases with D^*.

3.1 Introduction

When a single-phase mixture is thrust into the unstable region of the phase diagram, the mixture phase separates via spinodal decomposition (SD). Phase separation can be induced by thermal quenching, solvent evaporation or polymerization, known as thermal-induced phase separation (TIPS), solvent-induced phase separation (SIPS), and polymerization-induced phase separation (PIPS), respectively. The PIPS method is a complex process because phase separation and polymerization occur simultaneously. In the PIPS method, the degree of polymerization of the polymerizing component continuously increases as the reaction proceeds, and this induces phase separation because the curing point eventually crosses over from the homogenous (stable) region to the two-phase (unstable) region [1, 9, 10].

The PIPS method based on condensation-reaction polymerization is an important manufacturing route for multi-phase material production. A typical example is the production of high impact polystyrene (HIPS). HIPS is manufactured using the PIPS process by polymerizing styrene monomer in the presence of polybutadiene (PB). As polymerization proceeds, PB phase separates and disperses in the polystyrene (PS) matrix. The particle size of the PB phase can be controlled by a proper choice of the processing conditions to obtain the desired properties. However, despite practical importance of PIPS in producing multi-component composite materials, relatively few theoretical [33-35, 50, 57, 82] and experimental [5, 44, 63, 74, 83] studies have been performed. In particular, no model has yet been developed to describe monomer polymerization in the presence of a polymer taking into account phase separation.

Coupled phase separation and polymerization processes have been modeled using the time dependent nonlinear Cahn-Hilliard (C-H) and Flory-Huggins (F-H) theory for phase separation, and a reaction kinetic equation for polymerization, in the previous studies [33-35]. The mobility and interfacial parameter in the C-H theory are dependent on both the polymer molecular chain lengths and local concentration in the PIPS process. Many numerical studies, however, have been performed assuming constant mobility and interfacial parameter with an attempt to simplify the problem. The interfacial parameter can be assumed to be concentration independent in the absence of any accurate information about its behavior; however, the mobility is known to be highly sensitive to concentration changes [43].

Glotzer et. al. [35] solved the nonlinear C-H equation with coupled diffusion and chemical reaction equations. They found that the combination of diffusion and reaction mechanisms determines the length scale of the phase separation patterns. However, they considered only a low-molar mass solvent and solute system using constant mobility. Chan and Rey [33, 34] solved the nonlinear fourth-order C-H equation to study the effects of diffusion coefficient and polymerization rate constant on the phase-separated morphology for polymer solutions in the PIPS process. Their system described polymerizing monomers in the presence of low molar mass solvents. They found that morphologies with high density of small droplets would be obtained by increasing the diffusion coefficient and the rate constant. However, they used a concentration independent mobility and, as a consequence, their equation diverges in the intermediate stage of phase separation when the concentration approaches unity. Furthermore, they obtained almost perfectly spherical droplets due to constant mobility. Shaginyan and Manevich [57] studied the PIPS process for a multi-component blend using a time-dependent reaction conversion factor. They used a concentration dependent mobility based on the Rouse theory and found that the thermodynamic states of the reacting mixture contain two different classes of relaxation of the concentration inhomogeneities. However, their study is limited to the very early stage of spinodal decomposition, where linear governing equation is solved analytically. The PIPS process is complex to describe and, for highly asymmetric polymer systems, computational divergence problem occurs in the very early stage of phase separation. For these reasons, the attempts have failed in describing practically important process, such as a monomer polymerizing in the presence of a polymer.

As a result of phase separation, various types of phase-separated structures can be formed depending on several factors, including concentration, the rate of polymerization, the types of materials used, and physical properties such as viscosity and the rate of diffusion [1]. Typical examples of phase-separated morphologies in polymer systems are the droplet-type morphology and the interconnected cylinder-type morphology. The type and characteristics of the phase-separated morphology are critical in determining the mechanical and optical properties of multi-component composite materials. For example, the fracture toughness increases as particle sizes in the morphology decrease. However, if the average droplet size decreases, scattering of multi-component materials increases because the number of scattering sites within the film increases. Therefore, it is necessary to develop a characterization of phase-separated morphologies to eventually find optical structures. A morphological analysis technique, known as intensity of segregation and scale of segregation, are employed in this study to characterize the phase-separated morphologies arising in the PIPS method.

In this chapter, the model equations based on the nonlinear C-H and F-H theory coupled with a reaction kinetic equation are solved to describe the PIPS method for the case of a monomer polymerization in the presence of a polymer. Numerical results are presented with the intensive parameter studies: the dimensionless diffusion coefficient and the dimensionless reaction rate constant. The dynamical and morphological studies on PIPS are performed and discussed to evaluate numerical results. The governing equations and auxiliary conditions are developed in Section 3.2 using the molecular weight and local concentration dependent mobility. Two governing equations for spinodal decomposition are formulated depending on the molecular weight regime of polymerizing component to reflect polymer chain diffusion in the presence of entanglements. In this study, the degree of polymerization of one component increases with time due to polymerization. Therefore, at the moment the degree of polymerization of the polymerizing component exceeds a critical degree of polymerization compounds to the onset of entanglements, the model equation is switched. In other word, our model equation covers various molecular weight regimes of polymerizing component ranging from low molecular weight polymer solutions to highly entangled polymer blends. The sets of non-periodic natural and zero-mass flux boundary conditions are used. In addition, the randomly generated initial conditions are used to reflect the infinitesimal thermal concentration fluctuations. Section 3.3 presents the brief background in the morphological characterization methods. The concepts of the intensity of segregation and the scale of segregation are discussed in this section.

The results of the intensive dynamical and morphological studies on PIPS are presented in Section 3.4. The typical types of the phase-separated structures of the PIPS method are illustrated in Section 3.4.1. The effects of the initial composition on the phase-separated morphologies are also discussed in this section. The dynamical features of the phase separation phenomena are studied and discussed, using Nauman's extent of phase separation [84], in Section 3.4.2. The extent of phase separation is a useful measure to determine the stages of phase separation and their temporal ranges. The various temporal critical points (the dimensionless polymerization lag time, the dimensionless phase separation lag time, the dimensionless induction time, the dimensionless transition time, etc.) are determined and studied for the different values of the dimensionless diffusion coefficient and the dimensionless reaction rate constant. Section 3.4.3 presents a study of the morphological analysis of PIPS. In this section, visualizations of patterns as a function of the dimensionless diffusion coefficient and the dimensionless reaction constant are presented to show how the morphologies change as two dimensionless parameters change. The effects of the dimensionless diffusion coefficient and the dimensionless reaction constant on the phase-separated morphologies are evaluated by using the scale of segregation. In addition, a measure of the time kinetics and the compositional non-uniformity of the phase separation process known as the intensity of segregation is shown as a function of time for different values of the dimensionless diffusion coefficient and the dimensionless reaction rate constant in this section. The various types of the phase-separated morphologies are re-characterized using the dimensionless average droplet diameter and the shape factor in Section 3.4.4. The dimensionless average droplet diameter and the shape factor give more accurate information about droplet size and shape distribution. Lastly, the general guidelines for morphological control in the PIPS process are presented in Section 3.4.6.

3.2 Governing Equations and Auxiliary Conditions

The Cahn and Hilliard equation is a widely used model for the phase separation phenomena via spinodal decomposition and is given by [21, 25, 26]:

$$\frac{\partial \Phi_A}{\partial t} = \nabla \cdot \left[M\nabla \left[\frac{\partial f}{\partial \Phi_A} - 2\kappa \nabla^2 \Phi_A \right] \right] \tag{3-1}$$

where Φ_A is the volume fraction of component A (for a binary mixture, $\Phi_A + \Phi_B = 1$), ∇ denotes $\partial/\partial x\ \bar{i} + \partial/\partial y\ \bar{j}$, where $\bar{i}$ and $\bar{j}$ are unit normal vectors for x and y directions, respectively, M is mobility, f is free energy density of the system, t is time, and κ is a positive interfacial constant, respectively.

For the bulk free energy density f in Eq. (3-1), the Flory-Huggins theory is used and is written as [29, 30]:

$$f = \frac{k_B T}{v} \left(\frac{\Phi_A}{N_A} \ln \Phi_A + \frac{\Phi_B}{N_B} \ln \Phi_B + \chi \Phi_A \Phi_B \right) \tag{3-2}$$

where k_B is Boltzmann constant, T is absolute temperature, v is the volume of the reference unit, N_A and N_B are the degree of polymerization of polymer A and B, respectively, and χ is the temperature dependent interaction parameter. The temperature dependence of χ can be written as [31]:

$$\chi = \frac{1}{2} - \Psi \left(1 - \frac{\Theta}{T} \right) \tag{3-3}$$

where Ψ is the dimensionless entropy and Θ is the theta temperature.

The mobility M in Eq. (3-1) is known to be highly dependent on the molecular weight and local concentration of the components and it is defined by:

$$M = \frac{D_A D_B N_A N_B \Phi_A \Phi_B}{\left(\frac{k_B T}{v} \right) (D_A + D_B)(N_A \Phi_A + N_B \Phi_B)} \tag{3-4}$$

where D_A and D_B are the self diffusion coefficients of polymer segments A and B, respectively. Full details of the derivation of Eq. (3-4) are given in Chapter 2, Section 2.2.2. Since polymer segments entangle when their molecular weight exceeds a critical degree of polymerization value N_c, polymers exhibit a different diffusion behavior depending on their molecular weight. To capture this different diffusion behavior, Eq. (3-

4) has to be specialized by using two different theories according to components' molecular weight. The Rouse theory represents the diffusion phenomena in the non-entanglement regime as [58]:

$$D = \frac{k_B T}{N\zeta}, \qquad N < N_c \tag{3-5}$$

while the diffusion of entangled polymers follows the reptation theory as [59, 60]:

$$D = \left(\frac{4}{15}\right)\left(\frac{k_B T N_e}{\zeta N^2}\right), \qquad N > N_c \tag{3-6}$$

where ζ is the friction coefficient and N_e is the entanglement chain length. Note here that $N_c \approx 2N_e$.

The molecular dependent interfacial parameter κ in Eq. (3-1) is given by [24]:

$$\kappa = \kappa_0 \left(N_A + N_B\right) \tag{3-7}$$

where

$$\kappa_0 = \frac{k_B T}{12v} \chi \, g \, l_m^2 \, n_m \tag{3-8}$$

where g is the ratio of the square radius of a branched molecule to that of a linear one of the same molecular weight, n_m and l_m are the number of monomers and length of each monomer, respectively.

The governing equations describing spinodal decomposition are obtained by inserting Eqs. (3-2), (3-4), and (3-7) into Eq. (3-1), and performing the functional derivative. The diffusion coefficients, D_A and D_B, in Eq. (3-4) can be replaced with either Eq. (3-5) or Eq. (3-6) based on polymer components' molecular weight. Thus, for the non-entanglement regime:

$N < N_c$:

$$\frac{\partial \Phi_A^*(x,y,t)}{\partial t^*} = \frac{D^* T^*}{\left(N_A + N_B\right)} \left[\frac{-N_B\left(N_A\Phi_A^* + N_B\left(1-\Phi_A^*\right)\right) - N_B\left(N_A - N_B\right)\left(1-\Phi_A^*\right)}{\left(N_A\Phi_A^* + N_B\left(1-\Phi_A^*\right)\right)^2} \right.$$

$$+\frac{N_A\left(N_A\Phi_A^* + N_B\left(1-\Phi_A^*\right)\right) - N_A\left(N_A - N_B\right)\Phi_A^*}{\left(N_A\Phi_A^* + N_B\left(1-\Phi_A^*\right)\right)^2}$$

$$-2\chi\frac{N_A N_B\left(N_A\Phi_A^* + N_B\left(1-\Phi_A^*\right)\right)\left(1-2\Phi_A^*\right) - N_A N_B\left(N_A - N_B\right)\Phi_A^*\left(1-\Phi_A^*\right)}{\left(N_A\Phi_A^* + N_B\left(1-\Phi_A^*\right)\right)^2}\Bigg]$$

$$\left(\frac{\partial\Phi_A^*}{\partial x^*}\frac{\partial\Phi_A^*}{\partial x^*} + \frac{\partial\Phi_A^*}{\partial y^*}\frac{\partial\Phi_A^*}{\partial y^*}\right) + \frac{D^*T^*}{\left(N_A + N_B\right)}\Bigg[\frac{N_B\left(1-\Phi_A^*\right)}{N_A\Phi_A^* + N_B\left(1-\Phi_A^*\right)} \qquad (3\text{-}9)$$

$$+\frac{N_A\Phi_A^*}{N_A\Phi_A^* + N_B\left(1-\Phi_A^*\right)} - 2\chi\frac{N_A N_B\Phi_A^*\left(1-\Phi_A^*\right)}{N_A\Phi_A^* + N_B\left(1-\Phi_A^*\right)}\Bigg]\left(\frac{\partial^2\Phi_A^*}{\partial x^{*2}} + \frac{\partial^2\Phi_A^*}{\partial y^{*2}}\right)$$

$$-\frac{N_A N_B\left(N_A\Phi_A^* + N_B\left(1-\Phi_A^*\right)\right)\left(1-2\Phi_A^*\right) - N_A N_B\left(N_A - N_B\right)\Phi_A^*\left(1-\Phi_A^*\right)}{\left(N_A\Phi_A^* + N_B\left(1-\Phi_A^*\right)\right)^2}$$

$$\left(\frac{\partial^3\Phi_A^*}{\partial x^{*3}}\frac{\partial\Phi_A^*}{\partial x^*} + \frac{\partial^3\Phi_A^*}{\partial x^*\partial y^{*2}}\frac{\partial\Phi_A^*}{\partial x^*} + \frac{\partial^3\Phi_A^*}{\partial x^{*2}\partial y^*}\frac{\partial\Phi_A^*}{\partial y^*} + \frac{\partial^3\Phi_A^*}{\partial y^{*3}}\frac{\partial\Phi_A^*}{\partial y^*}\right)$$

$$-\frac{N_A N_B\Phi_A^*\left(1-\Phi_A^*\right)}{\left(N_A\Phi_A^* + N_B\left(1-\Phi_A^*\right)\right)}\left(\frac{\partial^4\Phi_A^*}{\partial x^{*4}} + 2\frac{\partial^4\Phi_A^*}{\partial x^{*2}\partial y^{*2}} + \frac{\partial^4\Phi_A^*}{\partial y^{*4}}\right)$$

For the entangled high molecular weight regime, the governing equation is written as:

$N > N_c$:

$$\frac{\partial\Phi_A^*(x,y,t)}{\partial t^*} = \frac{4\ D^*T^*N_e}{15\ \left(N_A^2 + N_B^2\right)}\Bigg[\frac{-N_B\left(N_A\Phi_A^* + N_B\left(1-\Phi_A^*\right)\right) - N_B\left(N_A - N_B\right)\left(1-\Phi_A^*\right)}{\left(N_A\Phi_A^* + N_B\left(1-\Phi_A^*\right)\right)^2}$$

$$+\frac{N_A\left(N_A\Phi_A^* + N_B\left(1-\Phi_A^*\right)\right) - N_A\left(N_A - N_B\right)\Phi_A^*}{\left(N_A\Phi_A^* + N_B\left(1-\Phi_A^*\right)\right)^2}$$

$$-2\chi\frac{N_A N_B\left(N_A\Phi_A^* + N_B\left(1-\Phi_A^*\right)\right)\left(1-2\Phi_A^*\right) - N_A N_B\left(N_A - N_B\right)\Phi_A^*\left(1-\Phi_A^*\right)}{\left(N_A\Phi_A^* + N_B\left(1-\Phi_A^*\right)\right)^2}\Bigg]$$

$$\left(\frac{\partial\Phi_A^*}{\partial x^*}\frac{\partial\Phi_A^*}{\partial x^*} + \frac{\partial\Phi_A^*}{\partial y^*}\frac{\partial\Phi_A^*}{\partial y^*}\right) + \frac{4\ D^*T^*N_e}{15\ \left(N_A^* + N_B^*\right)}\Bigg[\frac{N_B\left(1-\Phi_A^*\right)}{N_A\Phi_A^* + N_B\left(1-\Phi_A^*\right)} \qquad (3\text{-}10)$$

$$+\frac{N_A\Phi_A^*}{N_A\Phi_A^* + N_B\left(1-\Phi_A^*\right)} - 2\chi\frac{N_A N_B\Phi_A^*\left(1-\Phi_A^*\right)}{N_A\Phi_A^* + N_B\left(1-\Phi_A^*\right)}\Bigg]\left(\frac{\partial^2\Phi_A^*}{\partial x^{*2}} + \frac{\partial^2\Phi_A^*}{\partial y^{*2}}\right)$$

$$-\frac{4}{15}\frac{N_e(N_A+N_B)}{(N_A^2+N_B^2)}\frac{N_AN_B\left(N_A\Phi_A^*+N_B(1-\Phi_A^*)\right)(1-2\Phi_A^*)-N_AN_B(N_A-N_B)\Phi_A^*(1-\Phi_A^*)}{\left(N_A\Phi_A^*+N_B(1-\Phi_A^*)\right)^2}$$

$$\left(\frac{\partial^3\Phi_A^*}{\partial x^{*3}}\frac{\partial\Phi_A^*}{\partial x^*}+\frac{\partial^3\Phi_A^*}{\partial x^*\partial y^{*2}}\frac{\partial\Phi_A^*}{\partial x^*}+\frac{\partial^3\Phi_A^*}{\partial x^{*2}\partial y^*}\frac{\partial\Phi_A^*}{\partial y^*}+\frac{\partial^3\Phi_A^*}{\partial y^{*3}}\frac{\partial\Phi_A^*}{\partial y^*}\right)$$

$$-\frac{4}{15}\frac{N_e(N_A+N_B)}{(N_A^2+N_B^2)}\frac{N_AN_B\Phi_A^*(1-\Phi_A^*)}{\left(N_A\Phi_A^*+N_B(1-\Phi_A^*)\right)}\left(\frac{\partial^4\Phi_A^*}{\partial x^{*4}}+2\frac{\partial^4\Phi_A^*}{\partial x^{*2}\partial y^{*2}}+\frac{\partial^4\Phi_A^*}{\partial y^{*4}}\right)$$

Eqs. (3-9) and (3-10) are written in dimensionless form and the superscripted asterisks denote dimensionless variables where dimensionless variables are as follows: $x^* = x/L$, $y^* = y/L$, $t^* = 2\kappa_0 vt/L^4\zeta$, $T^* = T/\Theta$, and $D^* = k_B\Theta L^2/2v\kappa_0$ where L represents length scale of the computational domain. To solve Eq. (3-9) and Eq. (3-10), the following sets of natural and zero-mass flux boundary conditions are used:

$$\frac{\partial\Phi_A^*}{\partial x^*}=0 \quad , \qquad \text{at } t^*>0, \text{ and } x^*=0 \text{ and } x^*=1 \qquad \text{(3-11-a)}$$

$$\frac{\partial\Phi_A^*}{\partial y^*}=0 \quad , \qquad \text{at } t^*>0, \text{ and } y^*=0 \text{ and } y^*=1 \qquad \text{(3-11-b)}$$

and

$$\frac{\partial^3\Phi_A^*}{\partial x^{*3}}+\frac{\partial^3\Phi_A^*}{\partial x^*\partial y^{*2}}=0 \quad , \qquad \text{at } t^*>0, \text{ and } x^*=0 \text{ and } x^*=1 \qquad \text{(3-12-a)}$$

$$\frac{\partial^3\Phi_A^*}{\partial y^{*3}}+\frac{\partial^3\Phi_A^*}{\partial y^*\partial x^{*2}}=0 \quad , \qquad \text{at } t^*>0, \text{ and } y^*=0 \text{ and } y^*=1 \qquad \text{(3-12-b)}$$

In addition, the randomly generated initial conditions are used to reflect the infinitesimal thermal concentration fluctuations present initially in the homogeneous phase mixture as:

$$\Phi_A^*(\,t^*=0\,)=\Phi_{A,0}^*+\delta\,\Phi_A^*(\,t^*=0\,) \qquad \text{(3-13)}$$

The linearization approximation and the equipartition theorem are employed for the infinitesimal concentration derivations $\delta\ \Phi_A^*$, and details are given in references [48] and [49].

In the PIPS method, the molecular weight of one of the components, say B, increases with time due to polymerization and this induces phase separation. The growth rate of N_B in Eqs. (3-9) and (3-10) is determined by solving the following kinetic rate equation:

$$\frac{dp}{dt} = k_1(1 - p)^2 \qquad (3\text{-}14)$$

where p is the extent of reaction and k_1 is the rate constant. By assuming N_B can be represented with the weight average molecular sizes $\overline{X}_w$, for the single reactant system the solution to Eq. (3-14) leads to [24]:

$$N_B = \frac{1 + 2K^*t^*}{1 + 2K^*t^* - \gamma\, K^*t^*} \qquad (3\text{-}15)$$

where γ is the functionality of monomer, and the dimensionless reaction rate constant K^* is defined by $K^* = k_1 L^4 \zeta / 2\kappa_0 v$. Note that, for $t = 0$, $N_B = 1$ while for $t^* \rightarrow \infty$, N_B is infinite and gelation occurs.

The governing equations, describing the polymerization-induced phase separation process, are Eq. (3-9) to Eq. (3-13), and Eq. (3-15). At $t^* < t_c^*(N_c)$, Eqs. (3-9) and (3-15) are solved with the boundary conditions given in Eqs. (3-11) and (3-12), and the initial condition given in Eq. (3-13). At $t^* = t^*(N_c)$, the polymer molecules start to entangle with each other. Therefore, the governing equation describing phase separation process is switched from Eq. (3-9) to Eq. (3-10) to reflect the entanglement effect and Eqs. (3-10) and (3-15) are solved using the same boundary conditions. However, the solution of the previous time step is used for the initial condition for Eq. (3-10). The value of N_c is material dependent, and it is set $N_c = 31.5$ in this study. The dependent variables are Φ_A^* and N_B, and the independent variables are x^*, y^* and t^*. While there is an analytical solution to Eq. (3-15), there is none for Eqs. (3-9) and (3-10). Thus, Eqs. (3-9) and (3-10) with their auxiliary conditions must be solved numerically for $\Phi_A^*(x^*, y^*, t^*)$. The parameters are the dimensionless diffusion coefficient D^*, the dimensionless rate constant K^*, the dimensionless initial average concentration $\Phi_{A,0}^*$, the dimensionless temperature T^*, and the Flory-Huggins interaction parameter χ. Moreover, the 2-dimensional square ($L \times L$) geometry is used in this study. The main object of interest in the computational modeling of the PIPS process is to characterize the temporal dynamics and morphological phenomena as a function of the governing dimensionless parameters. Therefore, in this study, we mainly focus on the effect of the dimensionless diffusion coefficient D^* and the dimensionless reaction rate constant K^* on the dynamical and morphological features of the PIPS process.

3.3 Morphological Characterizations

As mentioned earlier, a characterization of phase-separated morphologies is necessary to implement and visualize the SD in the PIPS method because mechanical properties of polymer blends depend on their morphologies, as mentioned earlier. The morphologies induced by SD could be uniform spherical droplets or non-uniform interconnected structures depending on the concentration of components [48, 49]. In visualizing morphological characteristics, it is much more complicated to analyze non-uniform structures than uniformly distributed components in matrix. In this study, a method for characterizing texture is introduced to analyze the various types of morphologies induced by SD.

In his paper dealing with the human visual perception of texture [85], Julesz introduced the order of complexity of textures to demonstrate that one can discriminate from each other if textures differ in their first- and second-order statistics, but cannot if they differ in their third- or higher-order statistics. The order of complexity is determined by scattering dots, needles, or triangles on the two textures and observing the probabilities with which dots, both ends of the needles, or all three ends of the triangles land on one component for the first-, second-, or third-order statistics, respectively. In other word, the first-order statistics represents the concentration of one component in a sample texture. Thus, we can distinguish its difference by brightness or luminance if one component is black and the other is white, for example. Even if, however, the proportions of two components are the same in two different samples, the probability of both ends of the needles landing on one component could be different if the two components are distributed differently in those samples. The second-order statistics are different for two sample textures in this case.

Tadmor and Gogos [86] applied the concept of the order of complexity to the characterization of polymer mixtures. They concluded that the state of the mixture can be characterized by gross uniformity, texture and local structure. In dealing with 'gross uniformity', only the first-order statistics can be taken into account, however, in dealing with 'texture', the situation is more complex because it depends on component's size, shape and distribution, that is, second-order statistics.

In this study, a gross uniformity does not have to be considered because we already assumed that there is no mass exchange with surroundings in our calculation. Thus a perfect gross uniformity can be assumed once we initialize same average concentration for two different calculations.

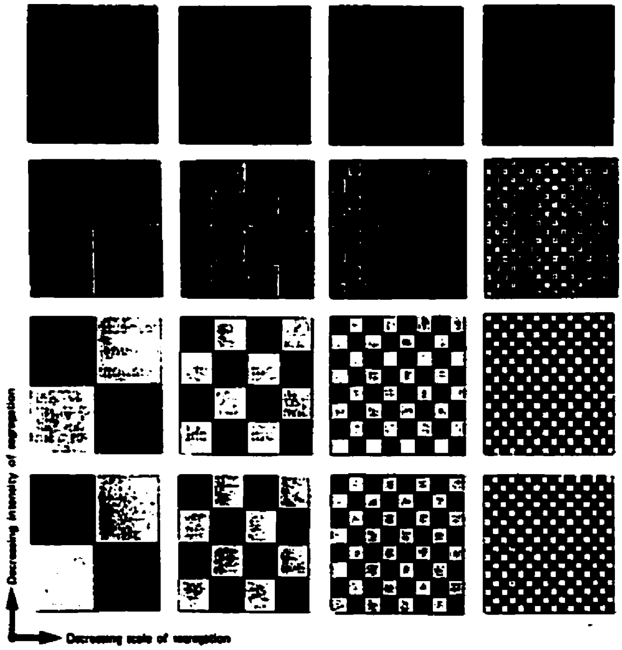

Figure 3.1 Schematic representation of the intensity segregation and the scale of segregation. A perfect compositional uniformity is obtained by either reducing the scale of segregation to the scale of the ultimate particle or by reducing the intensity of segregation to zero. (reprinted from reference [86])

The textures can be fully characterized by measuring two values; one is 'the scale of segregation' and the other is 'the intensity of segregation' [86]. The schematic representation of the scale of segregation and the intensity of segregation is shown in Fig. 3.1. It should be noted that a perfect compositional uniformity can be obtained by either reducing the scale of segregation to the scale of the ultimate particle or by reducing the intensity of segregation to zero [86].

'The scale of segregation' is calculated by a process known as 'dipole (needle) throwing', which consists in dropping a dipole of length r on the textures and observing the frequency with which both ends of the dipole fall on the same phase. However to avoid to do this tedious process, the coefficient of correlation is defined as:

$$R(r) = \frac{\sum_{i=1}^{N''} \left(\Phi'_{A,i} - \Phi^*_{A,0}\right)\left(\Phi''_{A,i} - \Phi^*_{A,0}\right)}{N'' S^2} \tag{3-16}$$

where $\Phi'_{A,i}$ and $\Phi''_{A,i}$ are concentrations at two points at a distance of r from each other, $\Phi^*_{A,0}$ is the average concentration, N'' is the total number of couples of concentrations taken, and S is the variance which is calculated from the concentrations at all points and given by:

$$S^2 = \frac{\sum_{i=1}^{2N''} \left(\Phi^*_{A,i} - \Phi^*_{A,0}\right)^2}{2N'' - 1} \tag{3-17}$$

Then, the scale of segregation s is defined as the integral of the coefficient of correlation $R(r)$ over values of r from zero to ς as:

$$s = \int_0^{\varsigma} R(r) dr \tag{3-18}$$

where ς represents the dipole length at which $R(\varsigma) = 0$. Note here that for a perfect correlation between the two phases, $R(r) = 1$, and for no correlation between the two phases, $R(r) = 0$.

The intensity of segregation I is defined as the ratio of the measured variance to the variance of a completely segregated system. Thus it is written as:

$$I = \frac{S^2}{\sigma_0^2} \tag{3-19}$$

where S^2 is the measured variance of the various points in the sample defined as:

$$S^2 = \frac{1}{N' - 1} \sum_{i=1}^{N'} \left(\Phi^*_{A,i} - \Phi^*_{A,0}\right)^2 \tag{3-20}$$

and σ_0^2 is the variance for completely unmixed state defined as:

$$\sigma_0^2 = \Phi^*_{A,0}\left(1 - \Phi^*_{A,0}\right) \tag{3-21}$$

where N' is the total number of concentration taken. For completely segregated state, $I = 1$ and uniformly distributed state, $I = 0$ since $S^2 = 0$.

3.4 Result and Discussion

3.4.1 Typical Phase-Separated Structures and Patterns

Figure 3.2 shows plots of $1/\chi$ versus Φ^*_A computed based on the Flory-Huggins equation (Eq. (3-2)) for increasing molecular weight of component B. The solid curves denote the binodal lines and the dashed curves represent the spinodal lines. The bold solid and dashed curves represent the initial binodal line and spinodal line, respectively, i.e. $N_A = 100$ and $N_B = 1$. As polymerization proceeds at point **a** or **b**, the molecular weight of component B increases and the phase diagram moves up gradually, as indicated by the upward pointing arrow. In this study, the composition of component A/B is set at 0.2/0.8 (point **a**) and 0.4/0.6 (point **b**). Initially, both point **a** and point **b** are located in the off-critical concentration region. However, as polymerization proceeds, point **b** is thrust into the dimensionless critical concentration region $\Phi^*_{A,c}$, while point **a** remains the off-

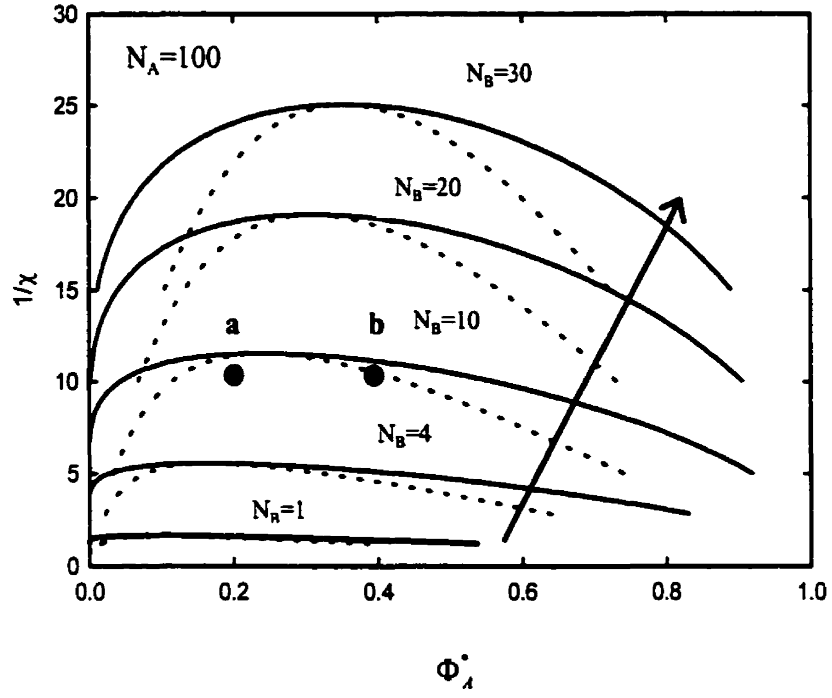

Figure 3.2. Phase diagrams of $1/\chi$ versus Φ_A^* computed based on the Flory-Huggins equation for increasing molecular weight of component B where χ is the Flory-Huggins interaction parameter and Φ_A^* is dimensionless concentration of polymer A. The solid curves denote the binodal lines and the dashed curves represent the spinodal lines. As polymerization proceeds at point **a** (A/B=20/80) or point **b** (A/B=40/60), the molecular weight of component B increases and the phase diagram is gradually elevated.

critical region at all times during the polymerization process. At both curing points, **a** and **b**, the mixture is initially homogeneous. After a certain reaction time ($N_s > 10$ in Figure 3.1), the curing point is thrust into a two-phase region and phase separation via spinodal decomposition takes place. The simulations listed in Table 1 are performed for the system described in Figure 3.1. The cases from A to I correspond to point **a**, while the case J, K, and L correspond to point **b**. All simulations are performed with $\Psi = 1.0$, $T^* = 1.7$ and $\chi = 0.0882$.

Case	$D^*/10^6$	$K^*/10^3$	$\Phi^*_{A,0}$
A	1	2	0.2
B	1	10	0.2
C	1	50	0.2
D	2	2	0.2
E	2	10	0.2
F	2	50	0.2
G	4	2	0.2
H	4	10	0.2
I	4	50	0.2
J	2	10	0.4
K	2	50	0.4
L	4	50	0.4

Table 3.1. The simulations listed above are performed for the system described in Figure 3.2 where D^* is the dimensionless diffusion coefficient, K^* is the dimensionless reaction rate constant, and $\Phi^*_{A,0}$ is the dimensionless initial concentration of component A. The cases from A to I correspond to point **a**, while the cases J, K and L correspond to point **b**. All simulations are performed with $\Psi = 1.0$, $T^* = 1.7$ and $\chi = 0.0882$.

Figure 3.3 describes the dimensionless concentration spatial profile $\Phi^*_A(x^*, y^*)$ (first column) and patterns (second column) formed during phase separation for Case F in Table 3.1 and at point **a** in Figure 3.2, and at the following dimensionless times: (a) $t^* = 1.619 \times 10^{-5}$, (b) $t^* = 1.808 \times 10^{-5}$, (c) $t^* = 1.816 \times 10^{-5}$, (d) $t^* = 1.823 \times 10^{-5}$, (e) $t^* = 1.838 \times 10^{-5}$, and (f) $t^* = 1.853 \times 10^{-5}$. Darker regions are polymer A rich regions while brighter regions are polymer B rich region. Since the dimensionless average concentration of polymer A, $\Phi^*_{A,0}$, remains in the off-critical region at all times during the polymerization and phase separation process for point **a**, a droplet-type morphology forms and evolves. At the very early stage, the random initial condition develops into a droplet-type phase-separated structure (see pattern (b)). The average droplet diameter

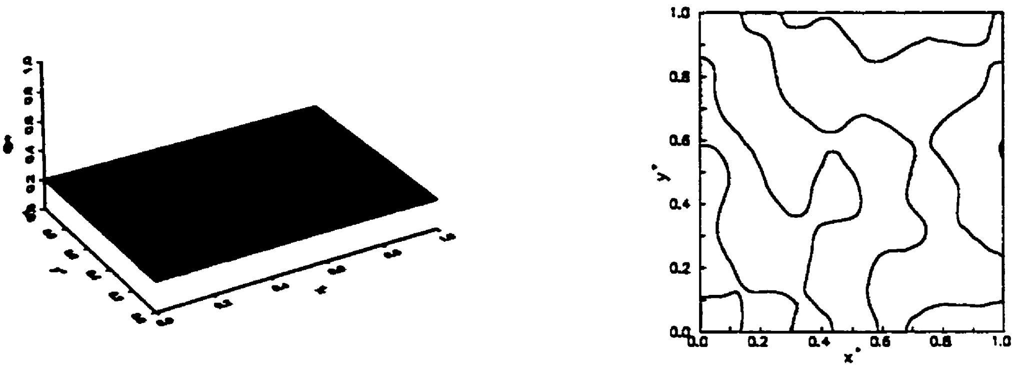

(a) $t^* = 1.619 \times 10^{-5}$

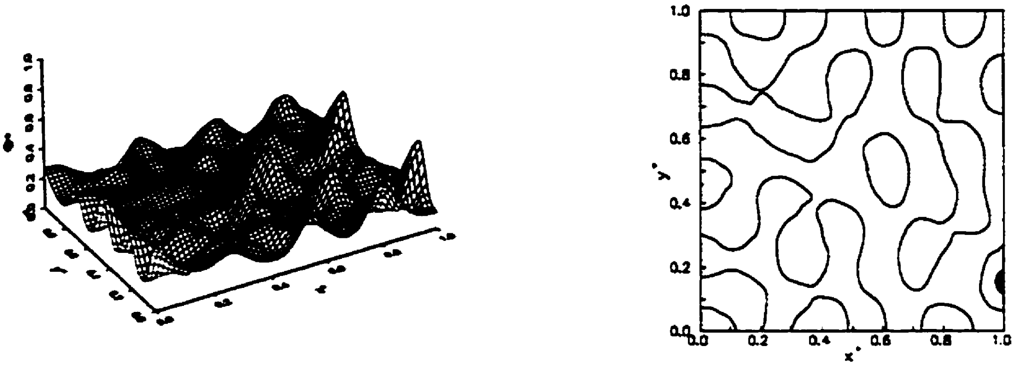

(b) $t^* = 1.808 \times 10^{-5}$

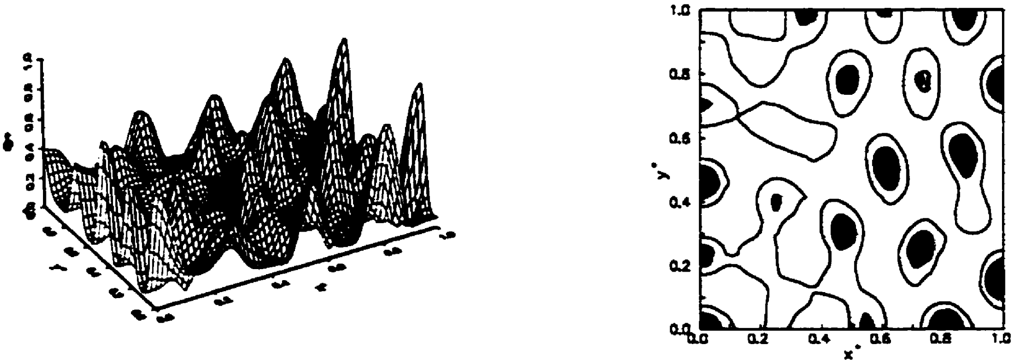

(c) $t^* = 1.816 \times 10^{-5}$

☐ ☐ ■

Φ_B^* Φ_A^*

Figure 3.3 (Continued on next page) Dimensionless concentration spatial profiles $\Phi_A^*(x^*, y^*)$ (first column) and patterns (second column) formed during the phase separation phenomena for Case F at point **a** (A/B=20/80).

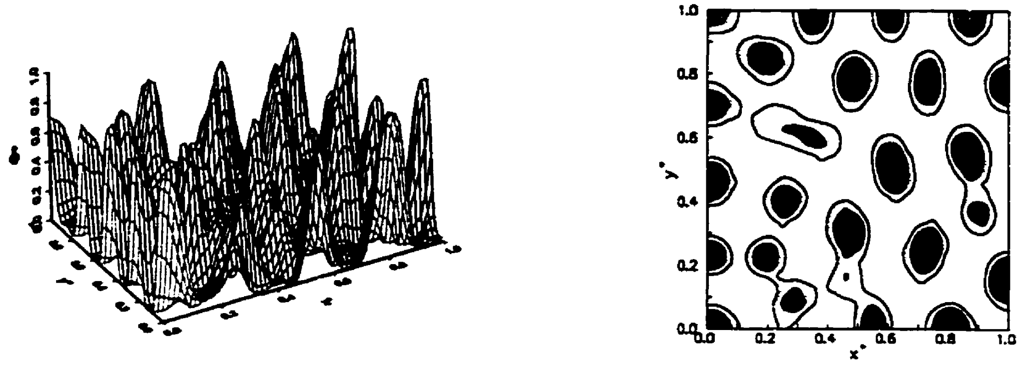

(d) $t^* = 1.823 \times 10^{-5}$

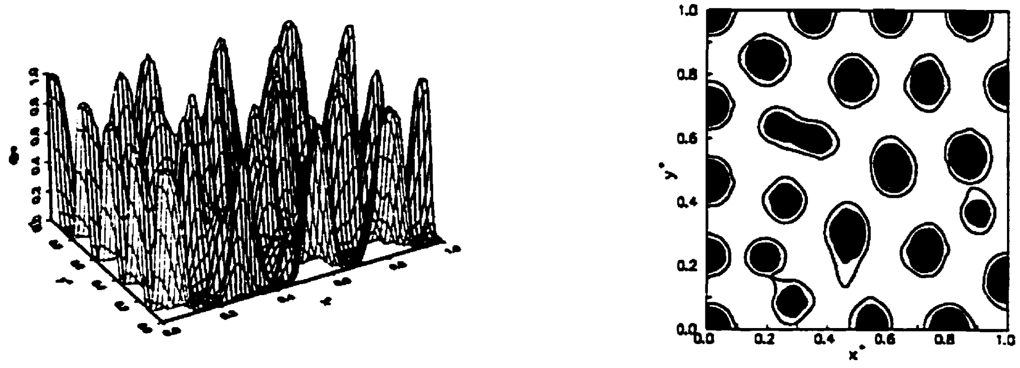

(e) $t^* = 1.838 \times 10^{-5}$

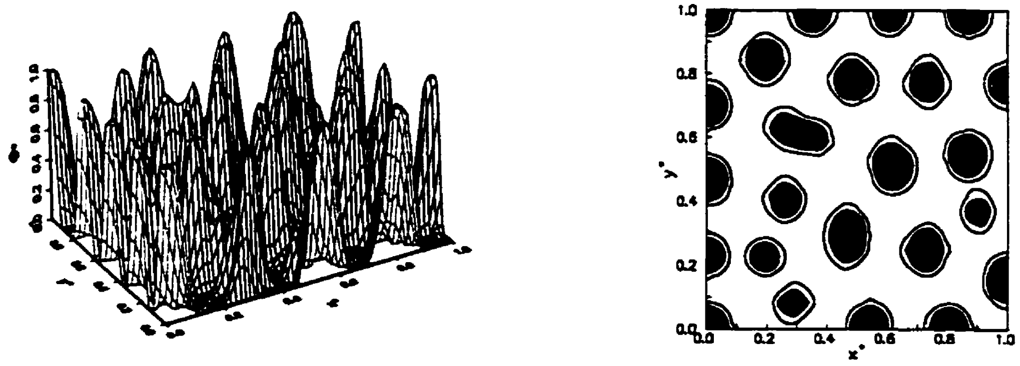

(f) $t^* = 1.853 \times 10^{-5}$

☐ ☐ ■

Φ_B^* Φ_A^*

Figure 3.3.

decreases, but the droplet number density and the concentration intensity inside the droplets increases with time during phase separation. As polymerization proceeds, the phase diagram shifts toward higher temperature and concentration as shown in Figure 3.2. As a result, the quench depth, defined as the absolute difference between the critical and curing temperature, $\left| T_c - T \right|$, increases with time and results in the smaller average droplet diameter and the higher droplet number density because it is known that wavelength of concentration is inversely proportional to the quench depth [9]. Even though this fact applies to the TIPS process, it can be also used for the PIPS process since the phase diagram is fixed at any given time. Some elliptically shaped particles can be observed in the patterns (d) and (e); however they are subsequently absorbed into the neighboring matrix as phase separation proceeds, and evolve to the nearly circular particles.

Figure 3.4 represents the dimensionless concentration spatial profiles $\Phi_A^*(x^*, y^*)$ (first column) and patterns (second column) formed during the phase separation phenomena for Case K in Table 3.1 and at point **b** (A/B=40/60) in Figure 3.2, and at the following dimensionless times: (a) $t^* = 1.649 \times 10^{-5}$, (b) $t^* = 1.797 \times 10^{-5}$, (c) $t^* = 1.804 \times 10^{-5}$, (d) $t^* = 1.806 \times 10^{-5}$, (e) $t^* = 1.810 \times 10^{-5}$, and (f) $t^* = 1.820 \times 10^{-5}$. Again, darker regions are polymer A rich regions, while brighter regions represent polymer B rich regions. As shown in Figure 3.2, the initial curing point **b** is located in the off-critical region during the very early phase separation stage $\left(t^* < t^*(N_B{=}20) \right)$. As a result, the phase-separated structure at $t^* = 1.797 \times 10^{-5}$ (pattern (b)) in Figure 3.4 is very similar to pattern at $t^* = 1.808 \times 10^{-5}$ (pattern (b)) in Figure 3.3. In other word, the random initial condition for Case J develops initially into the droplet-type morphology, similarly to Case F. As polymerization proceeds, however, the phase diagram continuously moves toward higher concentration and temperature as mentioned before; thus the curing point **b** is thrust into the critical region after $t^* > t^*\left(N_B \approx 20\right)$ as shown in Figure 3.1. As a result, the early phase-separated structure similar to the droplet-type structure develops into interconnected cylinders. Since the curing point **b** stays in the off-critical region during the very early stage of phase separation, droplets coexist with the

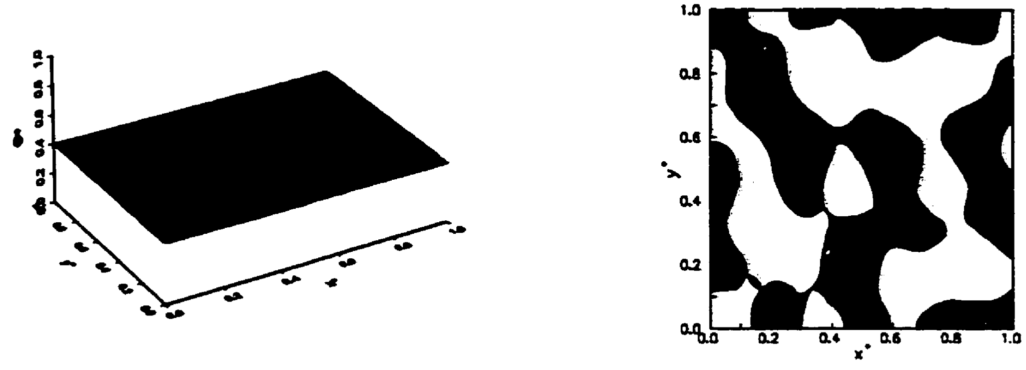

(a) $t^* = 1.649 \times 10^{-5}$

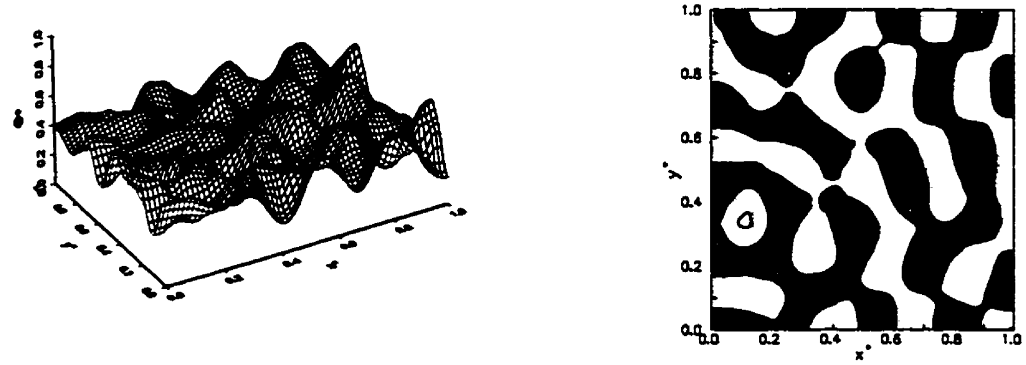

(b) $t^* = 1.797 \times 10^{-5}$

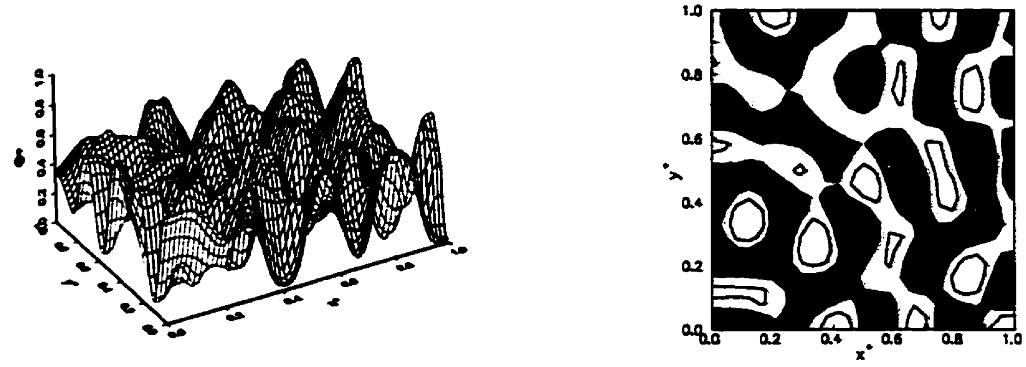

(c) $t^* = 1.804 \times 10^{-5}$

Figure 3.4. (Continued on next page) Dimensionless concentration spatial profiles $\Phi_A^*(x^*, y^*)$ (first column) and patterns (second column) formed during the phase separation phenomena for Case K at point **b** (A/B=40/60).

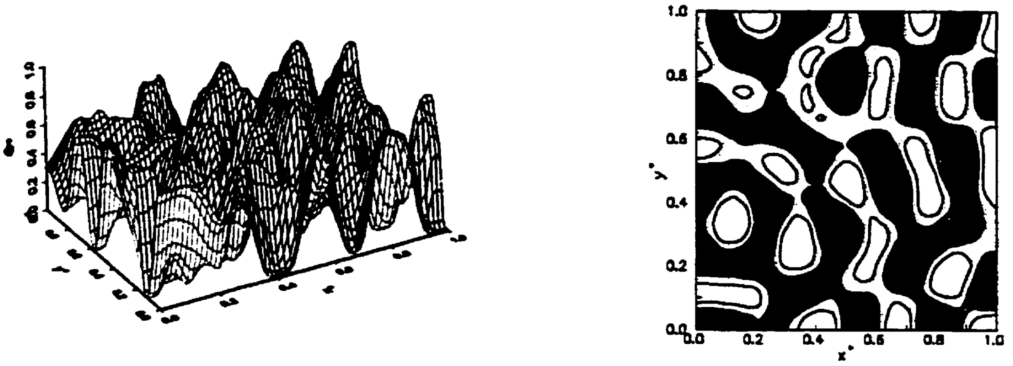

(d) $t^* = 1.806 \times 10^{-5}$

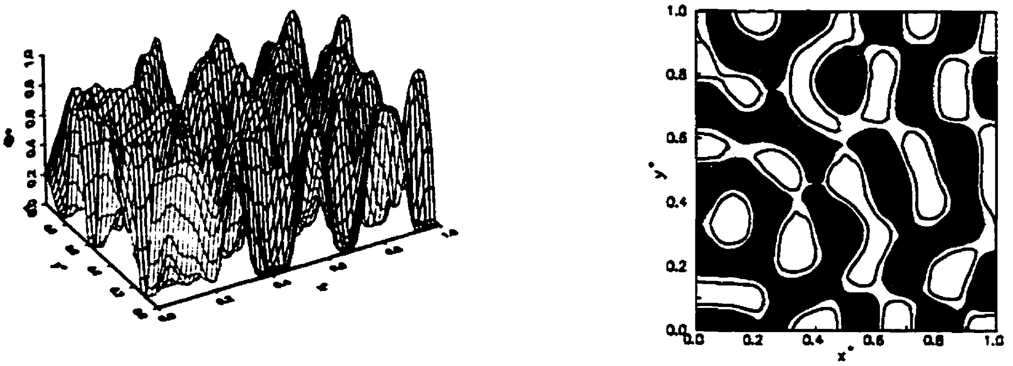

(e) $t^* = 1.810 \times 10^{-5}$

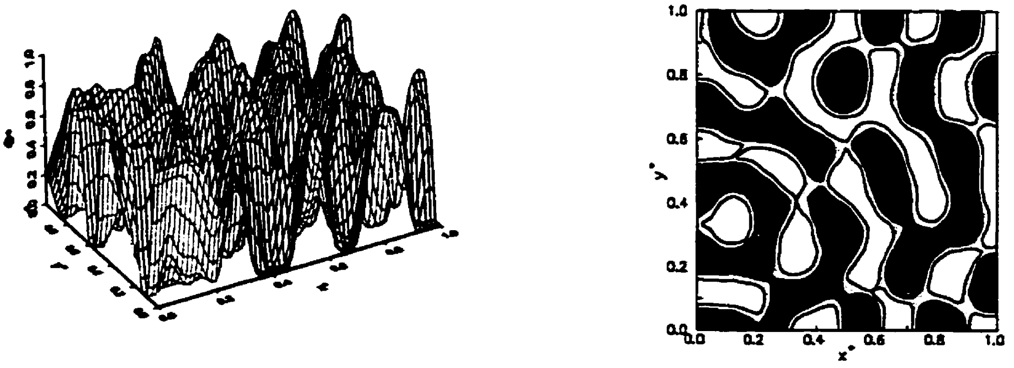

(f) $t^* = 1.820 \times 10^{-5}$

Figure 3.4.

interconnected cylinders in the same morphology (see patterns (d) and (e) in Figure 3.4). When we compare the patterns (e) and (f), the interconnected cylinders coarsen, and the droplets are absorbed into neighboring cylinders. As the phase separation phenomena proceeds, concentration gradients at the surface increases: thus the total free energy also increases with time. To reduce this total free energy, the interconnected cylinders coarsen, favoring a smaller interfacial area.

3.4.2 Dynamical Analysis in Polymerization-induced Phase Separation

To characterize the dynamical phenomena during phase separation, Ariyapadi and Nauman [84] developed a useful measure, known as the extent of phase separation E:

$$E = \frac{1}{N'^2}\sum_{j=1}^{N'}\sum_{i=1}^{N'} \frac{\left(\Phi^*_{A,i,j} - \Phi^*_{A,0}\right)^2}{\left(\Phi^*_{A,0} - \Phi^*_{A,l}\right)\left(\Phi^*_{A,u} - \Phi^*_{A,0}\right)} \tag{3-22}$$

where $\Phi^*_{A,i,j}$ is the volume fraction of component A at the $(i,\ j)$th computational nodal point, $\Phi^*_{A,l}$ and $\Phi^*_{A,u}$ are the lower and upper binodal concentration of component A, respectively, and N' is the total number of nodal points in the computational domain. If there is no phase separation, $\Phi^*_{A,i,j} = \Phi^*_{A,0}$ for all nodal points, thus $E = 0$. On the other hand, for perfect phase-separated structure, $\Phi^*_{A,i,j}$ equals to either one of the two binodal points, $\Phi^*_{A,l}$ or $\Phi^*_{A,u}$, therefore $E = 1$.

It is known that the dimensionless induction time t^*_i exists in the PIPS process because significant phase separation only occurs at $t^* > t^*_i$ [33, 34]. The dimensionless induction time t^*_i can be represented by the sum of the dimensionless polymerization lag time t^*_{lp} and the dimensionless phase separation lag time t^*_{ls} as:

$$t^*_i = t^*_{lp} + t^*_{ls} \tag{3-23}$$

The dimensionless polymerization lag time t^*_{lp} represents the time it takes for the spinodal line to cross the initial curing point and the dimensionless phase separation lag time t^*_{ls} is time required for the system to begin phase separation once it has been placed in the unstable region [33, 34].

Figure 3.5 illustrates a typical plot of the extent of phase separation E versus the difference between the dimensionless time t^* and the dimensionless polymerization lag time t^*_{lp} for Case F. The dashed lines represent tangents to each part of the curve. Their intersection gives a dimensionless transition time t^*_t between the early and intermediate stage of spinodal decomposition. The dimensionless polymerization lag time t^*_{lp} can be

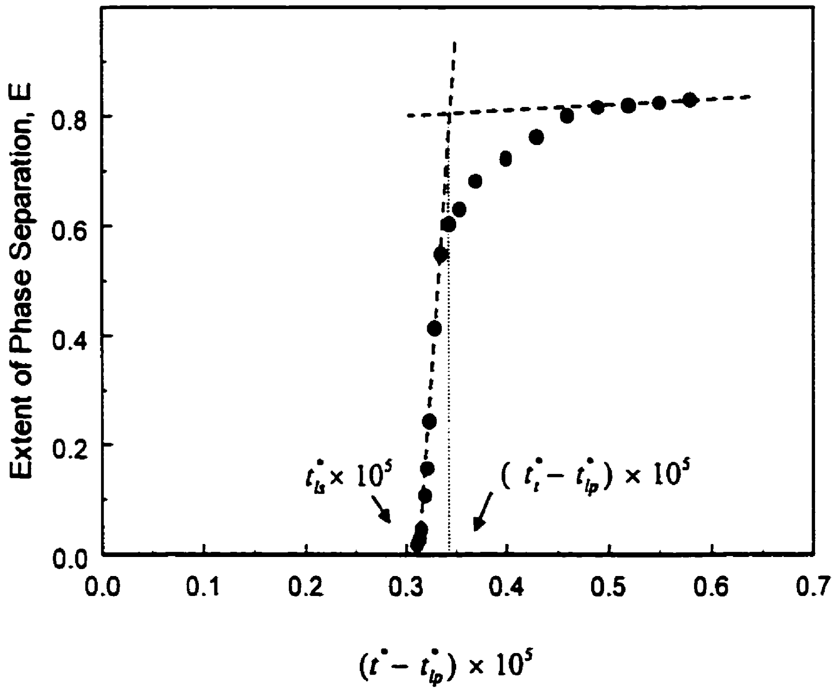

Figure 3.5 Extent of phase separation E versus dimensionless time t^* for Case F, where t^*_{ls} and t^*_t represent the dimensionless polymerization lag time and the dimensionless transition time, respectively. The intersection of the dashed tangent lines to each part of the curve gives the dimensionless transition time t^*_t between the early and intermediate stage of spinodal decomposition. Significant phase separation occurs only after the dimensionless induction time t^*_i. The dimensionless polymerization lag time can be obtained by solving Eq. (3-15) as $t^*_{lp} = 1.495 \times 10^{-5}$. For the pointed cases, $t^*_{ls} = 0.314 \times 10^{-5}$ and $t^*_t = 1.827 \times 10^{-5}$.

computed analytically by solving Eq. (3-15) and, for Case F, $t_{lp}^* = 1.495 \times 10^{-5}$. The dimensionless induction time t_i^* also can be obtained from Figure 3.5, using Eq. (3-23). Since no phase separation occurs until the curing point is thrust into the unstable region, E equals to zero from $t^* = 0$ to $t^* = t_i^*$. Significant phase separation only occurs at $t_i^* < t^* < t_t^*$, and E increases exponentially at this period only. At $t^* > t_t^*$, phase separation saturates and E increases very slightly as it enters the intermediate stage.

Figure 3.6 shows plots of the extent of phase separation E versus ($t^* - t_{lp}^*$) for Case D (■), E (▲), and F (●). For all three cases, $D^* = 2 \times 10^6$. However, the dimensionless reaction rate constants are $K^* = 2 \times 10^3$, $K^* = 1 \times 10^4$, and $K^* = 5 \times 10^4$ for Case D, Case E, and Case F, respectively. Since t_{lp}^* depends on K^*, t_{lp}^*'s are different for all three cases as follows: t_{lp}^*(Case D) = 3.738×10^{-4}, t_{lp}^*(Case E) = 7.476×10^{-5}, and t_{lp}^*(Case F) = 1.495×10^{-5}. However, the difference between t^* and t_{lp}^* is used for the abscissa to see the effect of K^* on t_{ls}^* rather than t_{lp}^*. This was done so that t_{lp}^* can be obtained by solving Eq. (3-13) analytically but there is no analytical solution for t_{ls}^*. Furthermore, because the actual phase separation time span is very small for Case K, this coordinate is easier to see. Figure 3.6 clearly shows that the dimensionless phase separation lag time t_{ls}^* decreases as K^* increases. The dimensionless polymerization lag time t_{lp}^* also decreases as K^* increases as shown before. Consequently the dimensionless induction time t_i^* is inversely proportional to K^*. The dimensionless transition time t_t^* is also inversely proportional to K^* and after t_t^*, phase separation saturates for all three cases. Another observation from Figure 3.6 is that the slope of E in the early stage is getting steeper as K^* increases. Thus, the rate of phase separation is proportional to K^*.

Plots of the extent of phase separation E versus ($t^* - t_{lp}^*$) for the different D^*'s are shown in Figure 3.7 for Case A (●), Case D (▲), and Case G (■). For all three cases, $K^* = 2 \times 10^3$, however, the dimensionless diffusion coefficients D^* are 1×10^6, 2×10^6, and 4×10^6 for the cases A, D, and G, respectively. The dimensionless

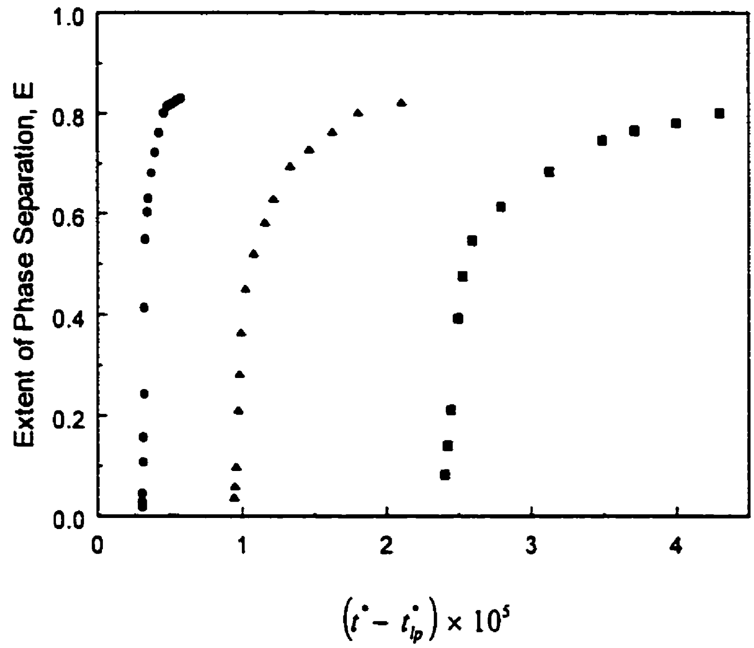

Figure 3.6 Extent of phase separation E versus ($t^{*} - t_{lp}^{*}$) for Case D (■), Case E (▲), and Case F (●). For all three cases, $D^{*} = 2 \times 10^{3}$, but the dimensionless reaction rate constants are $K^{*} = 2 \times 10^{3}$, 1×10^{4}, and 5×10^{4} for the cases D, E, and F, respectively.

polymerization lag time t_{lp}^{*}'s are the same for all three cases ($t_{lp}^{*} = 3.738 \times 10^{-4}$) because t_{lp}^{*} depends on K^{*} but not on D^{*}. Thus the variations of the dimensionless induction time t_{i}^{*} in this case are caused only by the variations of the dimensionless phase separation lag time, t_{ls}^{*}. As shown in Figure 3.7, t_{ls}^{*} and t_{i}^{*} decrease as D^{*} increases. The values of the extent of phase separation where they saturate are very similar to each other, i.e. $E \approx 0.82$. Therefore, their morphological evolution is quite similar in the intermediate stage although they have different dimensionless transition times t_{t}^{*}'s. This result is coincident with that of reference [33].

The values of t_{lp}^{*}, t_{ls}^{*}, and t_{t}^{*} for all cases are listed in Table 3.1. The dimensionless characteristic time t_{c}^{*} is defined as $t_{c}^{*} = 1.01 \times t_{t}^{*}$ to obtain the consistent phase separation data for the dynamical and morphological studies. As shown in Table 3.1, t^*_{ls}, t^*_i, and t^*_t decrease as K^* and D^* increase. However, t^*_{lp} decreases only when K^* increases. The value of D^* does not affect on the value of t^*_{lp}. The degree of polymerization of polymer B at the dimensionless characteristic time $N_B\left(t^*_c\right)$ increases as K^* increases, but decreases as D^* increases. Therefore, phase separation is dominantly restrained by entanglement of molecules at higher K^* and lower D^* values. As N_B increases, the phase diagram shown in Figure 3.2 elevates to higher temperature and the upper (lower) binodal point approaches to the higher (lower) value. As a result, the amount of phase separation, which is indicated by $\left|\Phi^*_A - \Phi^*_{A,0}\right|$, increases. Therefore, it is expected from Table 3.1 that the amount of phase separation is proportional to K^*, but inversely

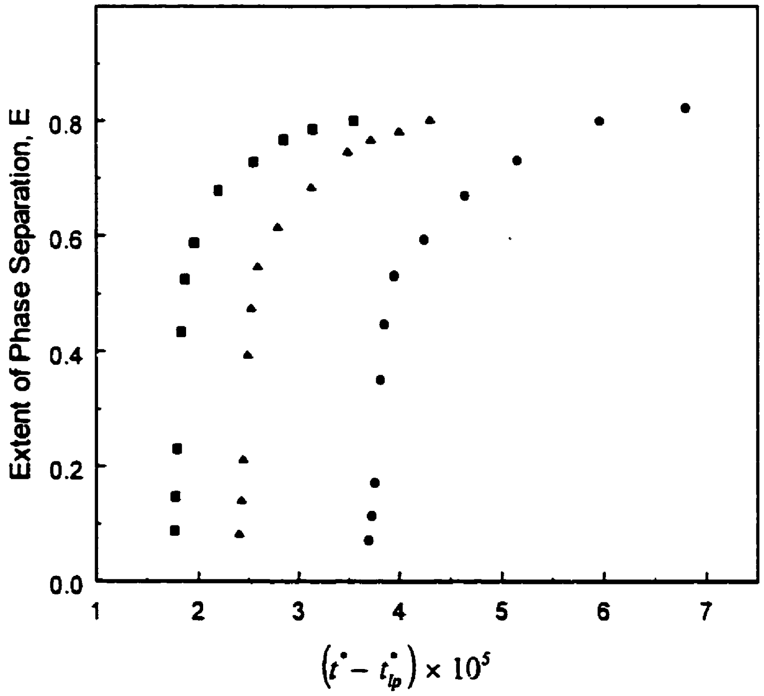

Figure 3.7. Extent of phase separation E versus $(t^* - t^*_{lp})$ for Case A (●), Case D (▲), and Case G (■). For all three cases, $K^* = 2 \times 10^3$, however, the dimensionless diffusion coefficients are $D^* = 1 \times 10^6$, 2×10^6, and 4×10^6 for the cases A, D, and G, respectively.

proportional to D^{*}. However, if N_B exceeds the critical degree of polymerization, $N_{B,c}$, it is expected polymer molecules to entangle each other and phase separation to be retarded. This entanglement effect is reflected in our governing equation by switching equations from (3-9) to (3-10). The degree of polymerization of component B, N_B, exceeds $N_{B,c}$, only for the cases B, C, F, and J because we assumed that $N_{B,c} = 31.5$. In other word, only for the cases B, C, F, and J, the system undergoes entanglement and phase separation simultaneously while for other cases, phase separation already saturates before the entanglement point.

Case	$t_{lp}^{*}\times 10^5$	$t_{ls}^{*}\times 10^5$	$t_t^{*}\times 10^5$	$t_c^{*}\times 10^5$	$N_B(t_c^{*})$
A	37.38	3.520	40.98	41.39	15.42
B	7.476	1.469	9.022	9.112	31.78
C	1.495	0.529	1.914	1.933	88.00
D	37.38	2.480	40.00	40.40	13.62
E	7.476	0.924	8.498	8.583	19.17
F	1.495	0.314	1.827	1.845	36.72
G	37.38	1.740	39.28	39.67	12.52
H	7.476	0.586	8.180	8.262	15.26
I	1.495	0.200	1.707	1.724	19.74
J	7.476	0.917	8.485	8.570	18.23
K	1.495	0.304	1.812	1.830	33.28
L	1.495	0.194	1.699	1.716	18.76

Table 3.1 Results for dynamical study of polymerization-induced spinodal decomposition where t_{lp}^{*}, t_{ls}^{*}, t_t^{*}, and t_c^{*} denote the dimensionless polymerization lag time, the dimensionless phase separation lag time, the dimensionless transition time, and the dimensionless characteristic time, respectively.

3.4.3 Morphological Analysis in Polymerization-induced Phase Separation

Figure 3.8 shows the dimensionless concentration spatial profiles $\Phi_A^*(x^*,y^*)$ (first column), and patterns (second column), for Case D (first row), Case E (second row), and Case F (third row), at the dimensionless characteristic times t_c^*. Note that we defined the dimensionless characteristic time, t_c^*, as $t_c^* = 1.01 \times t_t^*$. For all three cases $D^* = 2 \times 10^6$, however, the dimensionless rate constant K^*'s are: 2×10^3, 1×10^4, and 5×10^4 for Case D, Case E, and Case F, respectively. Figure 3.8 clearly shows that the average droplet diameter decreases but the number of droplets increases as K^* increases. Additionally, the maximum value of concentration of component A, $\Phi^*_{A,\max}$, inside the droplets increases as K^* increases (for Case D, $\Phi^*_{A,\max} = 0.767$, for Case E, $\Phi^*_{A,\max} = 0.857$, and for Case F, $\Phi^*_{A,\max} = 0.979$). It is also observed that the sizes and shapes of the phase-separated droplets are not perfectly circular, and some elliptically shaped particles are observed for all cases. This is clearly due to the local concentration dependent mobility, which is getting more important as phase separation continues. Almost perfectly circular droplets are obtained when we use the concentration dependent mobility [33, 34] because molecules diffuse symmetrically. Figure 3.8 clear shows that the orientation distribution of the major axis of the ellipses is broad, as it should realistically. This is in agreement with other studies that report that the elliptically shaped particles are observed when the concentration dependent mobility is used [84].

To perform the efficient morphological analysis neglecting any temporal variations for the each case, we defined the reduced time as:

$$\tau = \frac{t^*}{t_t^*} \tag{3-24}$$

where t_t^* is the dimensionless transition time from the early stage to the intermediate stage of spinodal decomposition. Figure 3.9 shows plots of the intensity of segregation I versus the reduced time τ for Case D (●), Case E (▲), and Case F (■). The intensity of segregation I has been defined in Eq. (3-17). Recall that I correspond to the first-order

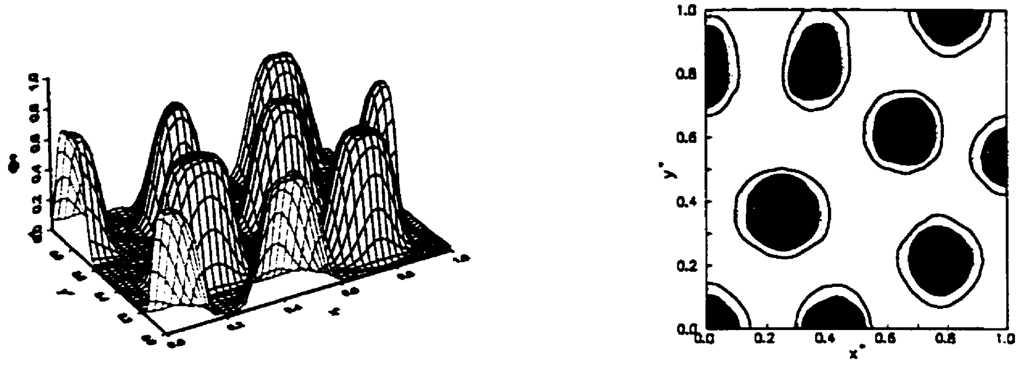

(a) Case D ($t_c^* = 33.03 \times 10^{-5}$)

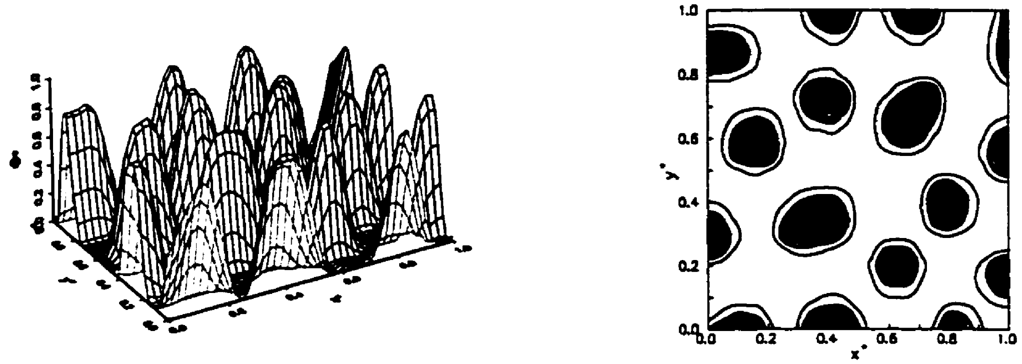

(b) Case E ($t_c^* = 8.583 \times 10^{-5}$)

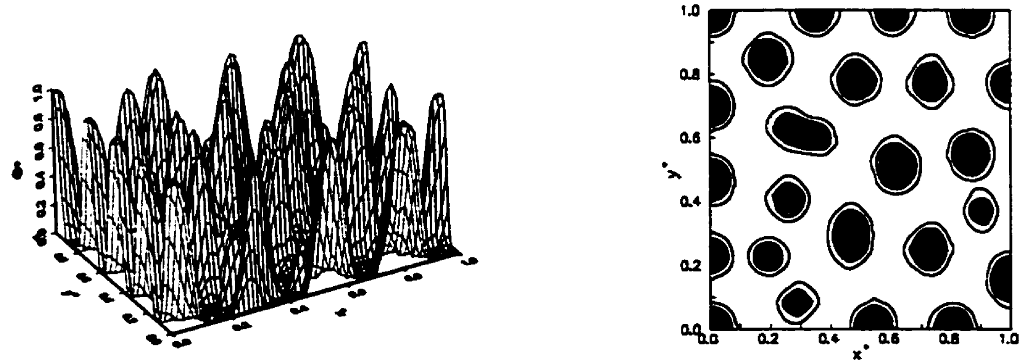

(c) Case F ($t_c^* = 1.845 \times 10^{-5}$)

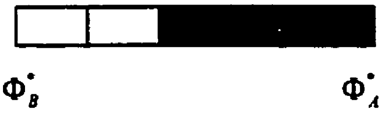

Figure 3.8 Dimensionless concentration spatial profiles $\Phi_A^*(x^*, y^*)$ (first column) and patterns (second column) at the dimensionless characteristic time τ for Case D (first row), Case E (second row) and Case F (third row). As the dimensionless rate constant K^* increases, the number of droplets increases while their average size decreases.

statistics, that is the difference of the proportion of each components, and the scale of segregation represents the second-order statistics, that is droplets' size or distribution in this study. The reduced time τ gives an efficient time scale to perform morphological studies on phase-separated textures in the presence of large phase separation temporal ranges. Note that at the dimensionless transition time $t^* = t_t^*$, τ equals to 1.00, while at the dimensionless characteristic time $t^* = t_c^*$, τ equals to 1.01. As mentioned earlier, for completely segregated state, $I = 1$, and uniformly distributed state, $I = 0$.

As shown in Figure 3.9, I increases significantly with time during the early stage of SD $(0.98 < \tau < 1.00)$; however, this significant growth slows down near the dimensionless transition time $\tau = 1.00$ for all three cases. After phase separation enters the intermediate stage $(\tau > 1.02)$, I saturates at $I \approx 0.1$ for all three cases. However, phase separation is more significantly repressed for Case F because molecules start to entangle each other before they enter the intermediate stage. The entanglement effect of

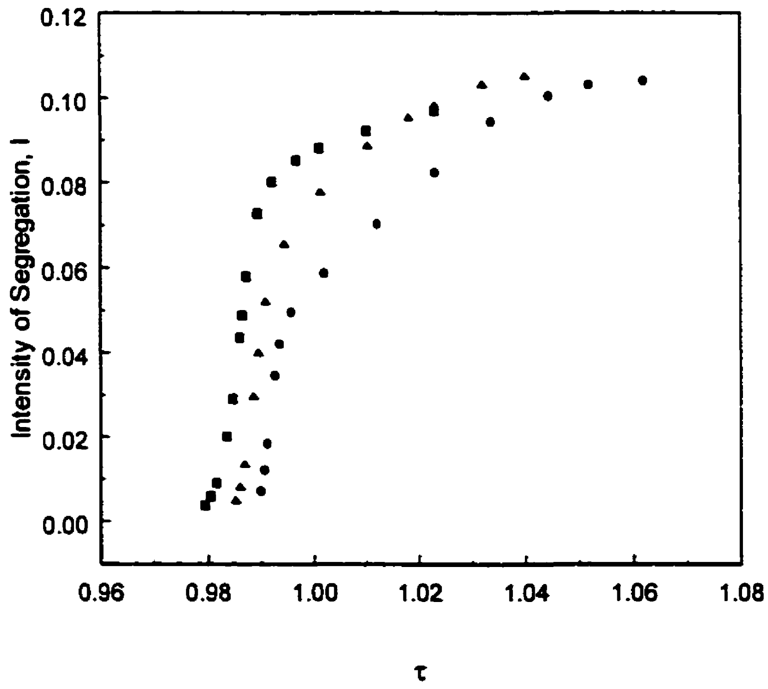

Figure 3.9 Plots of the intensity of segregation I versus the reduced time τ for Case D (●), Case E (▲), and Case F (■)

polymer molecules appears dominantly in the intermediate stage. Moreover, at the beginning of the intermediate stage ($1.00 < \tau < 1.02$), the growth rates of I are significantly different for the different K^*'s, and they increase as K^* increases. At the dimensionless characteristic time ($\tau = 1.01$), I(case D) $= 0.070$, I(case E) $= 0.087$, and I(case F) $= 0.091$. This can be explained as follows. The rate of changes of concentration are significantly different for different K^*'s. Therefore, it takes more time for Case D (lower K^*) to reach the saturated point than Case F (higher K^*). In addition, as K^* increases, the degree of polymerization of polymer B at the dimensionless characteristic time $N_B\left(t_c^*\right)$ increases as shown in Table 3.2. As a result, the amount of phase separation and the intensity of segregation increase as K^* increases. This result is consistent with the observation in Figure 3.8. The Figure 3.8 shows that at $t^* = t_c^*$ ($\tau = 1.01$), the maximum value of concentration of component A, $\Phi^*_{A,\max}$, inside the droplets increases as K^* increases. As the intermediate stage proceeds, however, these concentration differences (between Cases D, E, and F) inside droplets decrease and eventually disappear. For example, the Figure 3.9 shows that at $\tau = 1.06$, $I \approx 0.1$ for all three cases.

Figure 3.10 illustrates plots of the scale of segregation s defined in Eq. (3-15) versus τ, for Case D (●), Case E (▲), and Case F (■). Recall that s is proportional to the average droplet size, but it is inversely proportional to the number density of the droplets as shown in Figure 3.1. Figure 3.10 shows that the scale of segregation s decreases as time proceeds and as K^* increases. This is expected from Figure 3.3 and Figure 3.8. Since the random initial conditions develop initially a phase separation structure (see patterns (a) and (b) in Figure 3.3), the dimensionless average equivalent droplet diameter $\left\langle d^*\right\rangle$ and the scale of segregation s are large. As phase separation proceeds, $\left\langle d^*\right\rangle$ decreases, thus s decreases significantly during the early phase separation stage until the dimensionless transition time $\tau = 1.0$ (see patterns (c) and (d) in Figure 3.3). However, just after $\tau = 1.0$, s increases slightly when the phase-separated structure coarsens. As shown in Figure 3.7, $\left\langle d^*\right\rangle$ decreases as K^* increases. Therefore, s decreases as K^*

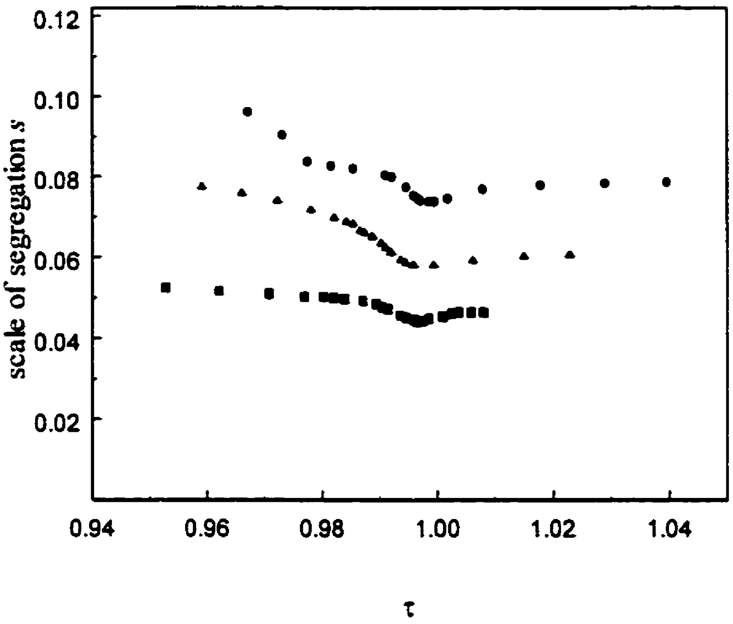

Figure 3.10 Scale of segregation s versus reduced time τ, for Case D (●), Case E (▲) and Case F (■).

increases at all times during the phase separation process, as Figure 3.10 shows. The values of s at the very early stage of SD ($\tau = 0.95$) are significantly different for each case, which indicates that from the very early stage of SD, the phase-separated structures, such as droplet size or distribution, are already different for each case.

Figure 3.11 illustrates the dimensionless concentration spatial profiles $\Phi^*_A(x^*, y^*)$ (first column) and patterns (second column) for Case A (first row), Case D (second row) and Case G (third row), at the dimensionless characteristic time t^*_c. The dimensionless reaction constants K^*'s are $K^* = 2.0 \times 10^3$ for all three cases. However, the dimensionless diffusion coefficients are: $D^* = 1.0 \times 10^6$ (Case A), $D^* = 2.0 \times 10^6$ (Case D), and $D^* = 4.0 \times 10^6$ (Case G). Figure 3.11 shows that the average droplet diameter decreases as D^* increases; however, the droplet number density increases more drastically as D^* increases. As a result, the maximum value of concentration, $\Phi^*_{A,\max}$, inside the droplet and the intensity of segregation I decrease at the dimensionless

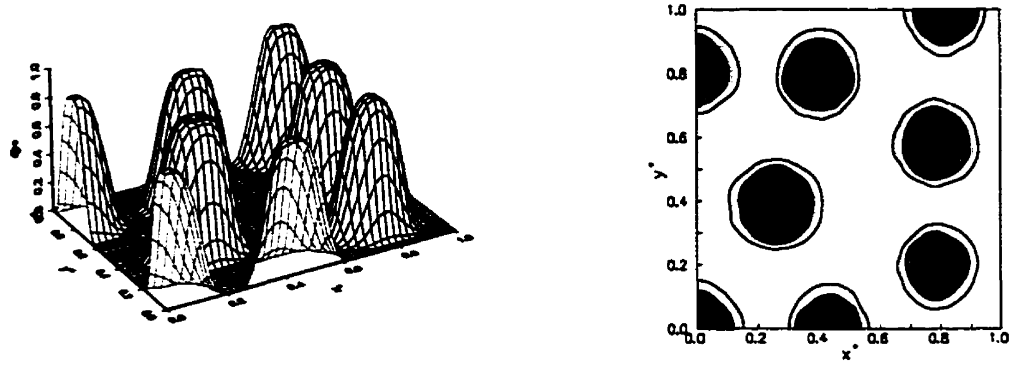

(a) Case A ($t_c^* = 41.39 \times 10^{-5}$)

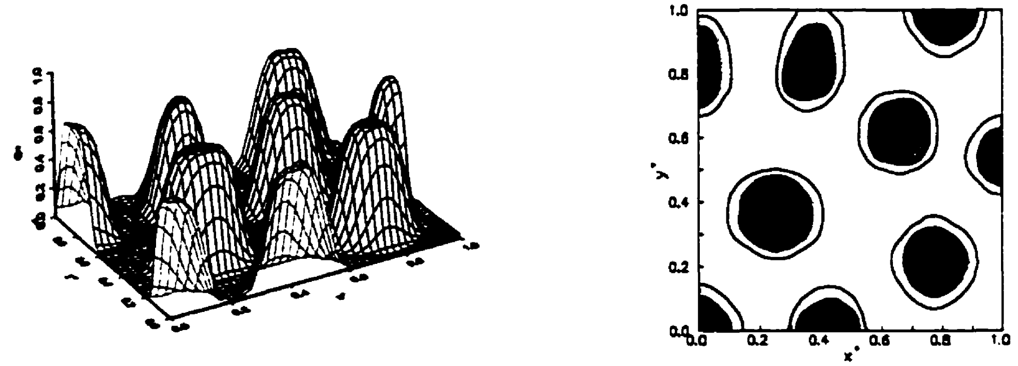

(b) Case D ($t_c^* = 40.40 \times 10^{-5}$)

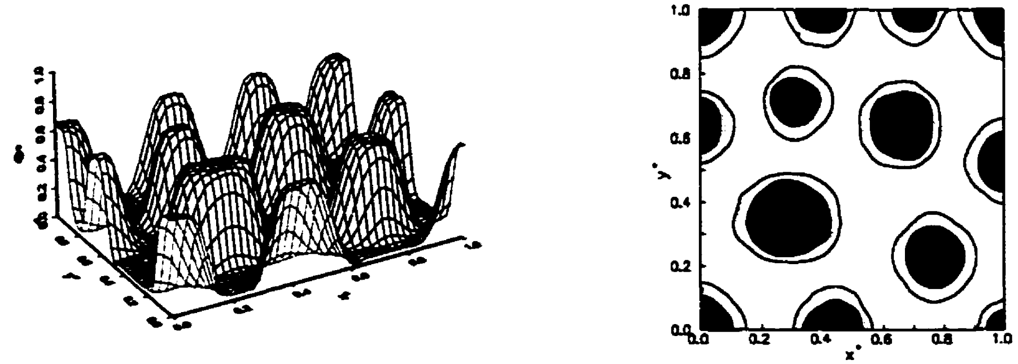

(c) Case G ($t_c^* = 39.67 \times 10^{-5}$)

Figure 3.11 Dimensionless concentration spatial profiles $\Phi_A^*(x^*, y^*)$ (first column) and patterns (second column) at the dimensionless characteristic time τ for Case A (first row), Case D (second row) and Case G (third row).

characteristic time t_c^* as D^* increases, when we compare the height of the dimensionless concentration spatial profiles (first column in Figure 3.11) and the gray level intensity of the patterns (second column in Figure 3.11).

Plots of the intensity of segregation I as a function of the reduced time τ for these cases are shown in Figure 3.12, for Case A (●), Case D (▲) and Case G (■). Certainly, the value of I at the dimensionless characteristic time t_c^* (at $\tau = 1.01$) decreases as D^* increases. The intensity of segregation I, which grows fast during the early phase separation stage, slows down and saturates at the value of I which are very close to each other for all three cases. This result is due to the following reasons. The intensity of segregation I is proportional to the amount of phase separation, which is indicated by $\left| \Phi_A^* - \Phi_{A,0}^* \right|$. As shown in the Table 3.1, the degree of polymerization of polymer B at the dimensionless characteristic time $N_B(t_c^*)$ increases with K^*, but decreases with D^*. As N_B increases, the phase diagram elevates to higher temperature (see Figure 3.2), thus the amount of phase separation $\left| \Phi_A^* - \Phi_{A,0}^* \right|$ increases. Consequently, I is proportional to N_B and K^*, however it is inversely proportional to D^*.

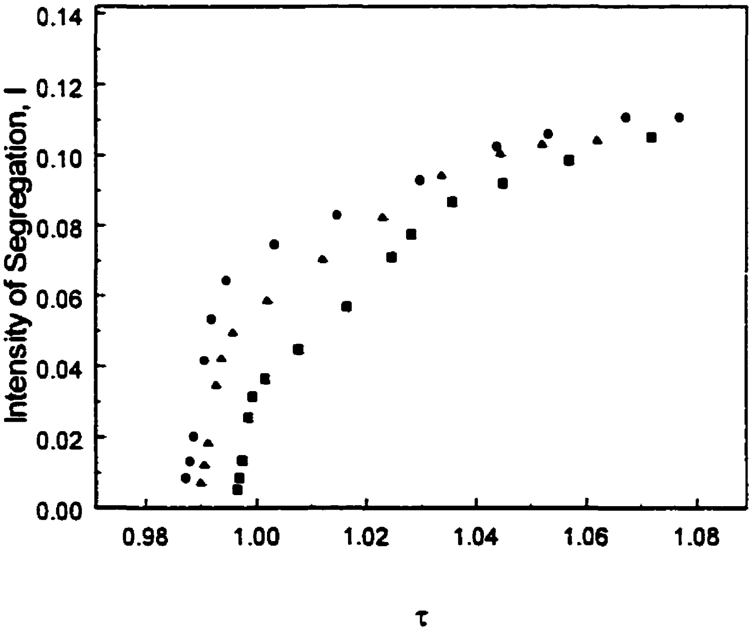

Figure 3.12 Intensity of segregation I as a function of reduced time τ for Case A (●), Case D (▲), and Case G (■)

Figure 3.13 shows plots of the scale of segregation s versus reduced time τ for Case A (●), Case D (▲), and Case G (■). The scale of segregation s decreases as D^* increases. This coincides with the results shown in Figure 3.11, that the average droplet size decreases and the droplet number density increases as D^* increases. The scale of segregation s decreases with time during the early phase separation stage; however, s slightly increases during the intermediate phase separation stage. This growth of s is clearly due to coarsening of phase separated structure as shown in Figure 3.3.

Figure 3.14 illustrates plots of the scale of segregation s versus the intensity of segregation I for different K^*'s with constant D^* (Figure 3.14 (a)) and for different D^*'s with constant K^* (Figure 3.14 (b)). Figure 3.14 (a) represents Case D (●), Case E (▲), and Case F (■), and Figure 3.14 (b) shows Case A (●), Case D (▲), and Case G (■). Both figures show that the scale of segregation s exponentially decreases as I increases during the very early stage of phase separation for all cases because the initial infinitesimal concentration fluctuations develop into the phase-separated structures during the very early stage of SD. Therefore, the significant morphological changes only occur

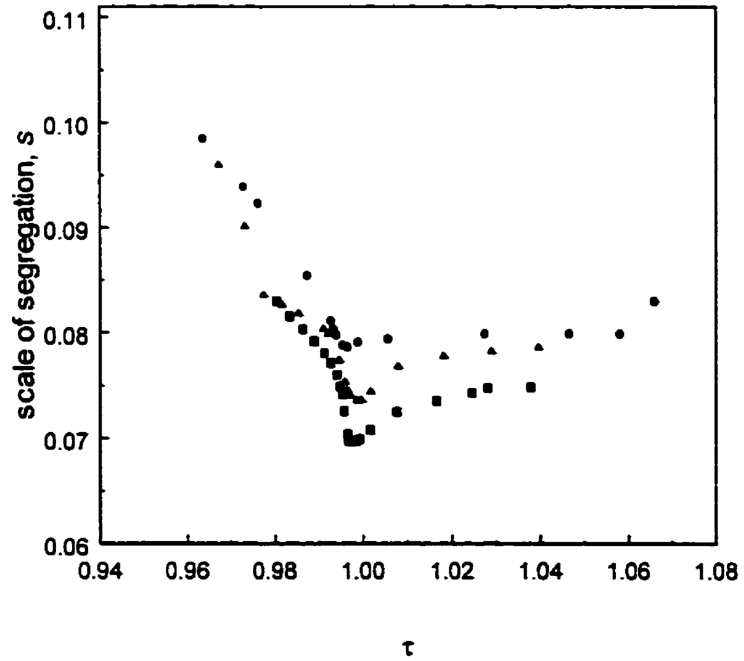

Figure 3.13 Scale of segregation s versus reduced time τ for Case A (●), Case D (▲), and Case G (■).

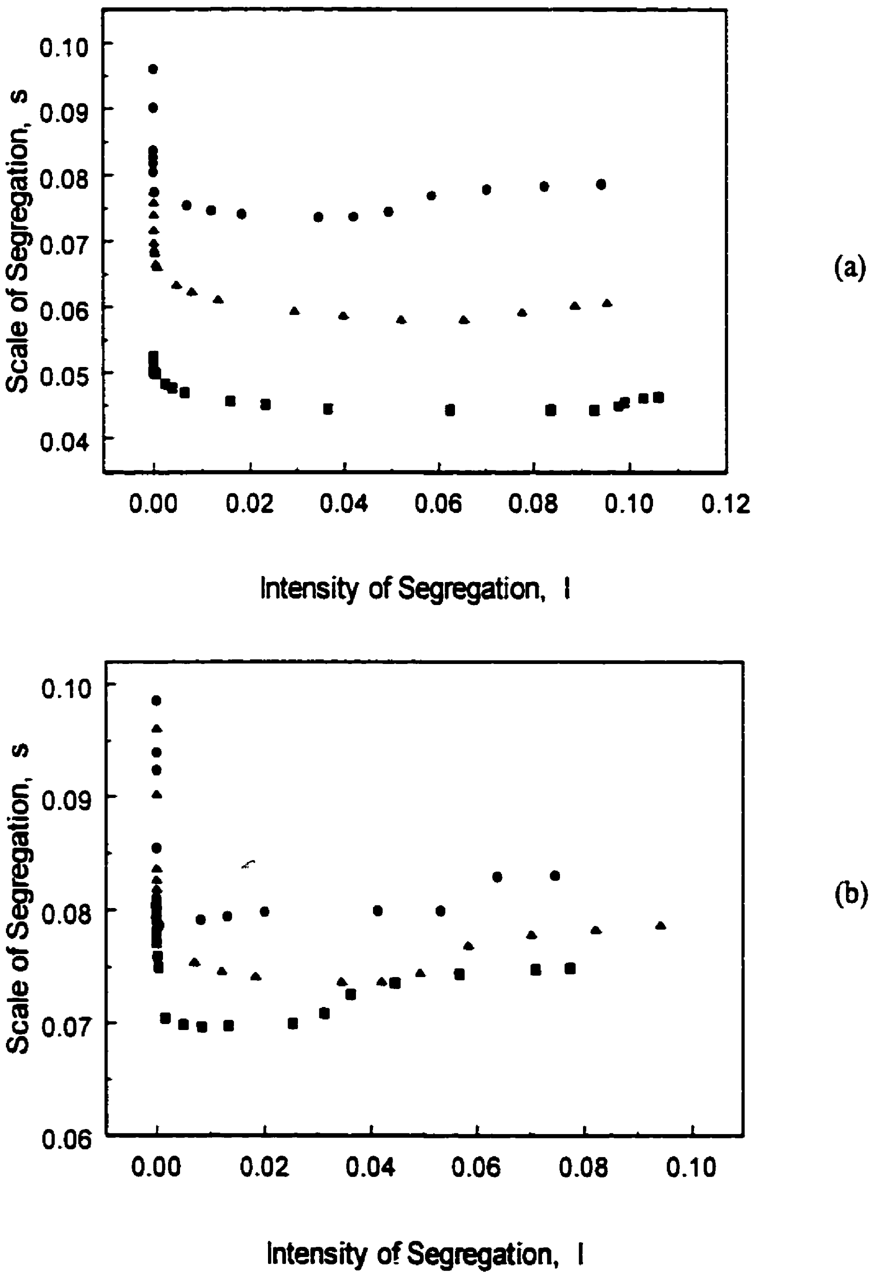

Figure 3.14 Plots of the scale of segregation s versus the intensity of segregation I (a) for different K^*'s with constant D^* for Case D (●), Case E (▲) and Case F (■), and (b) for different D^*'s with constant K^* for Case A (●), Case D (▲) and Case G (■).

immediately after the dimensionless induction time, t_i^*. During the early stage of SD, I continuously increases without any changes of s. Therefore, it is expected that the amplitude of concentration increases during the early stage of phase separation while the wavelength or droplet size is nearly constant in this period. After entering into the intermediate stage of phase separation, that is $t^* > t_i^*$, s increases slightly as I increases, which indicates that during the intermediate stage of SD, both the amplitude and wavelength of concentration increases and the phase-separated structure coarsens. However, s and I eventually saturate at $I \approx 0.1$. Furthermore, the scale of segregation s decreases as K^* and D^* increase at a constant intensity of segregation I.

3.4.4 Droplet Size and Shape Distributions

Using the intensity and scale of segregation, we can obtain comprehensive statistical information about the intensity of concentration inside the droplets, the droplet size, and number density. However, they do not give precise values of the droplet size and shape distributions. To obtain these more accurate measures, we performed an evaluation of droplet size and droplet shape distributions by computing the dimensionless equivalent diameter of the nearly circular droplets, d^*, and the their shape factor, S_f.

The dimensionless equivalent diameter, d^*, is defined as $d^* = \left(4A / \pi \right)^{1/2}$ where A is the area of the nearly circular droplets, and the shape factor is defined as $S_f = 4\pi A / P^2$ where P is the perimeter of droplets, respectively. Figure 3.15 shows frequency histograms for the dimensionless equivalent diameter d^* (first column) and the shape factor S_f (second column) for Case F in Table 3.1 at the following representative dimensionless times: $t^* = 1.823 \times 10^{-5}$ (first row), $t^* = 1.838 \times 10^{-5}$ (second row), and $t^* = 1.853 \times 10^{-5}$ (third row). Note that S_f represents a measure of how circular a droplet is. For a perfect circle, $S_f = 1$, while $S_f = 0$ for a line. The time variation of the histograms shows that the phase-separated morphology evolves gradually from the structure which has a wide distribution of droplet sizes and shapes to the structure which

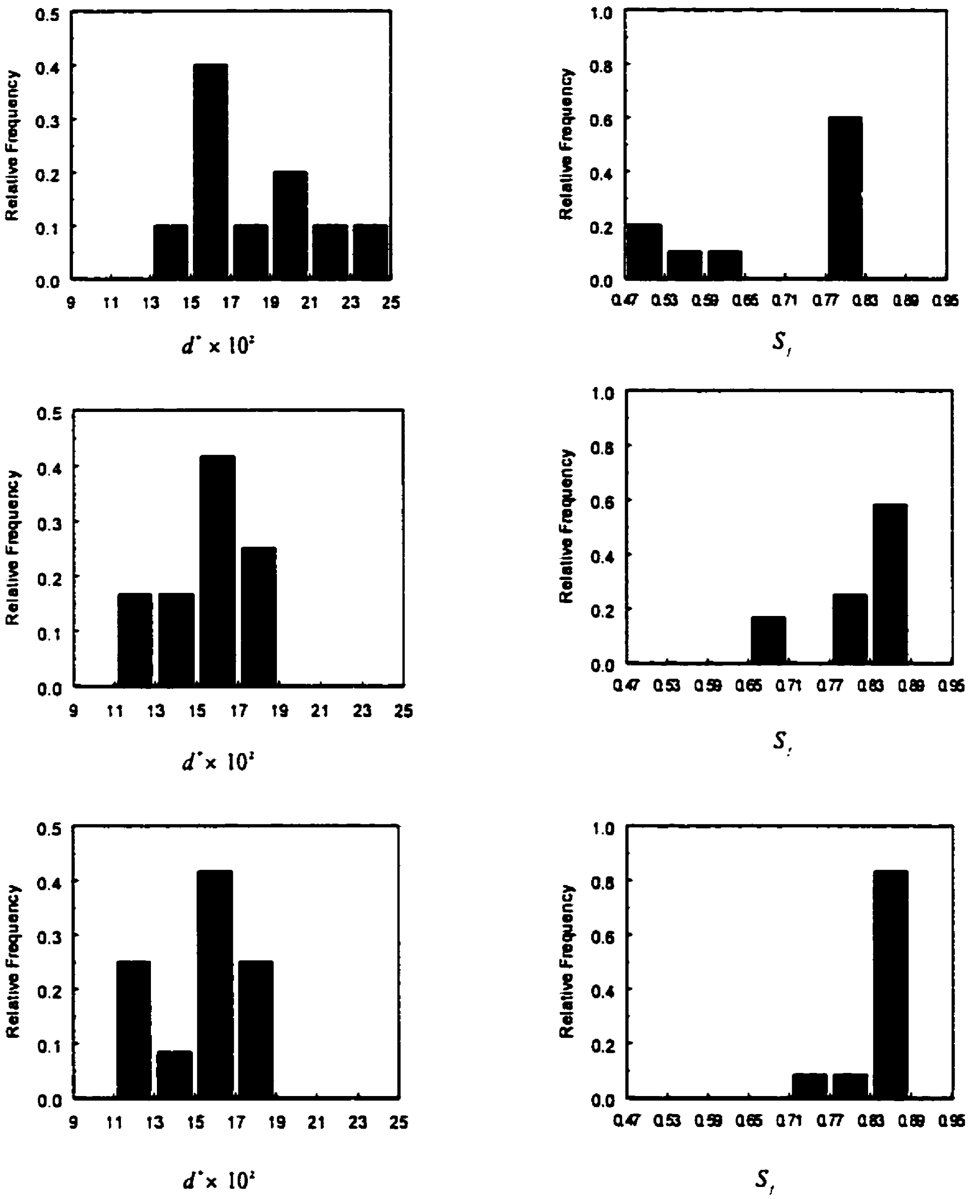

Figure 3.15 Frequency histograms for the dimensionless equivalent diameter of the nearly circular droplets d^* (first column) and the shape factor S_f (second column) for Case F at the following dimensionless times: $t^* = 1.823 \times 10^{-5}$ (first row), $t^* = 1.838 \times 10^{-5}$ (second row), and $t^* = 1.853 \times 10^{-5}$ (third row).

contains a dominant droplet size and shape range. The histograms of relative frequency versus d^* also show that d^* gradually decreases with time during the early phase separation stage. As phase separation proceeds, bigger droplets disappear while smaller droplets appear. However, the dominant droplet size ranged $0.15 < d^* < 0.17$ does not change. These results are also supported by the patterns shown in Figure 3.3. The histograms of relative frequency versus S_f show that dominant shape moves from the elliptical shape to the circular shape as time proceeds. The histograms for S_f also indicate that no droplets are perfectly circular, that is $S_f = 1$. Furthermore, the elliptically shaped particles are observed at all times during phase separation.

The simulation results for the various dimensionless parameter values are summarized in Table 3.3 where $I(t_c^*)$, $S(t_c^*)$, $\langle d^*(t_c^*)\rangle$, $\langle S_f(t_c^*)\rangle$ denote the intensity of segregation, the scale of segregation, the dimensionless equivalent average diameter and the average shape factor of the droplets, respectively, at the dimensionless characteristic time t_c^*. As shown in Table 3.3, $I(t_c^*)$ increases, but $S(t_c^*)$ and $\langle d^*(t_c^*)\rangle$ decrease as K^* increases at constant D^*. However $I(t_c^*)$, $S(t_c^*)$ and $\langle d^*(t_c^*)\rangle$ decrease as D^* increases at constant K^*. As mentioned earlier, the intensity of segregation I relates to the amount of phase separation. Thus it is proportional to the degree of polymerization of polymer B. Since the degree of polymerization of polymer B at the dimensionless characteristic time $N_B(t_c^*)$ is proportional to K^* but inversely proportional to D^*, the intensity of segregation at t_c^* is also proportional to K^* but inversely proportional to D^*. The scale of segregation s is proportional to the average droplet diameter, however it is inversely proportional to the droplet number density. Therefore, s decreases as K^* and D^* increase.

However, $I(t_c^*)$ for Case C is noticeably small compared to those of other cases. This result is clearly due to the entanglement effect governed by Eq. (3-10). With the higher value of K^* and the lower value of D^*, the rate of molecular weight increase dominates over the rate of phase separation, and molecular entanglement occurs in the early stage of phase separation. Table 3.3 also shows that the intensity of segregation is

Case	$I(t_c^*) \times 10^2$	$S(t_c^*) \times 10^2$	$\langle d^*(t_c^*) \rangle$	$\langle S_f(t_c^*) \rangle$
A	7.92	8.07	0.281	0.845
B	8.78	6.79	0.249	0.788
C	7.41	5.33	0.203	0.780
D	7.06	7.60	0.280	0.839
E	8.51	5.96	0.216	0.853
F	8.59	4.80	0.154	0.839
G	4.82	7.28	0.266	0.864
H	7.45	5.03	0.208	0.837
I	7.60	3.47	0.154	0.748
J	10.54	6.02	NA	NA
K	10.81	4.98	NA	NA
L	8.93	3.84	NA	NA

Table 3.3 Results for the morphological study of polymerization-induced spinodal decomposition where $I(t_c^*)$, $S(t_c^*)$, $\langle d^*(t_c^*) \rangle$, and $\langle S_f(t_c^*) \rangle$ denote the intensity of segregation, the scale of segregation, the dimensionless equivalent average diameter and the average shape factor of the droplets, respectively, at the dimensionless characteristic time t_c^*. (NA means not available)

more affected by polymer entanglement than the scale of segregation. This is because the phase-separated structure is established in the very early stage of phase separation as discussed earlier. Figure 3.16 illustrates the intensity of segregation I versus the dimensionless time t^* for Case F to show the effect of the switched governing equation. The arrow indicates the critical degree of polymerization of component B $N_{B,c}$, that is the switching point from Eq. (3-9) to Eq. (3-10). Two different governing equations, switched from Eq. (3-9) to Eq. (3-10) at $N_{B,c}$, are used for the circles and only one equation, Eq. (3-9), is used for the triangles. Figure 3.16 clearly shows that phase separation is restrained by Eq. (3-10), because the diffusion of molecules is retarded due to the entanglement of polymers.

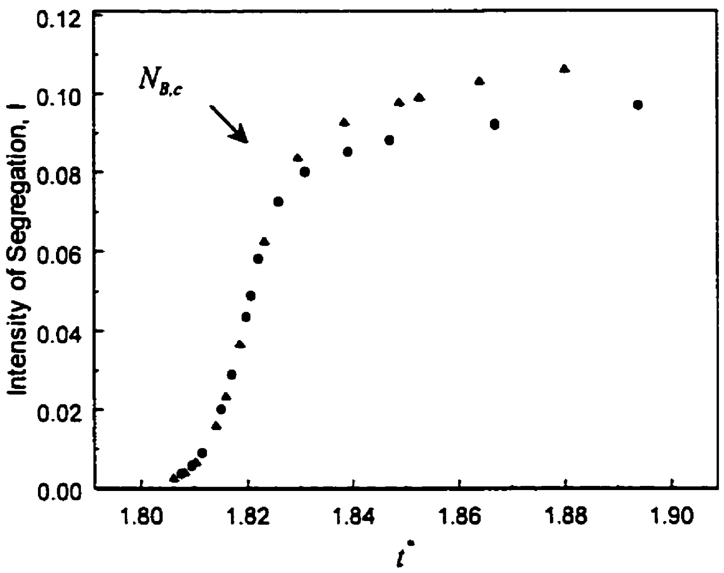

Figure 3.16 Intensity of segregation I as a function of the dimensionless time t^* for Case F where the arrow indicates the critical degree of polymerization of component B, $N_{B,c}$. Two governing equations (switched from Eq. (3-9) to Eq. (3-10) at $N_{B,c}$) used for circles and only one equation (Eq. (3-9)) is used for triangles. This figure clearly shows that phase separation is restrained by entanglement of polymers reflected in Eq. (3-10).

3.4.5 General Guidelines for Morphological Control in the PIPS process

To obtain the morphology with the smaller droplet diameter (or the narrower spacing between the particles) and the higher number density, the higher value of the reaction rate constant and/or the higher value of the diffusion coefficient should be used. The higher values of the reaction rate constant and the diffusion coefficient also give a faster processing time. However, the circular droplets are observed in the lower values of K^* and D^*. For the morphology with the larger droplet size and the lower number density, on the other hand, the low values of the reaction rate constant and the diffusion coefficient should be used.

The amount of phase separation is proportional to the dimensionless rate constant, K^*, but it is inversely proportional to the dimensionless diffusion coefficient D^*. Hence a large amount of phase separation can be obtained by using the higher value of K^* and the lower value of D^*. However, the degree of polymerization during the phase separation process N_B also increases with increasing K^*. Therefore, with the high value of K^*, the rate of increase of molecular weight dominates that of phase separation, and the polymer entanglements would occur in the early stage of phase separation.

3.5 Conclusions

In this chapter, simulations describing the PIPS process are presented when a monomer polymerizes in the presence of a polymer. The nonlinear fourth order partial differential governing equation based on the Cahn-Hilliard and Flory-Huggins theory for phase separation combined with a second-order polymerization kinetic equation is solved. The model consists of a balance equation for the low molecular weight regime and another balance equation for the high molecular weight entangled regime to cover all the molecular weight ranges of polymerizing component. We use the mobility that is a function of the molecular weight and concentration of the components, to describe the morphological evolution realistically. The most important aspects of the initial concentration evolution in the PIPS process, that is the dynamical and morphological features, are studied using useful indexes (the extent of phase separation for the dynamical study, and the intensity and scale of segregation for the morphological study). Depending on initial curing composition, two different types of morphology are formed: the interconnected cylinder-type morphology and the droplet-type morphology. The dimensionless phase separation induction time t_i^* represents the sum of the dimensionless polymerization lag time t_{lp}^* and the dimensionless phase separation lag time t_{ls}^* and it decreases as the dimensionless reaction rate constant K^* and the dimensionless diffusion coefficient D^* increase. The phase-separated morphology is fully characterized using the intensity of segregation I and the scale of segregation s. The intensity of segregation I is proportional to K^*, however it is inversely proportional to D^*. The scale of segregation s and the average droplet diameter decrease with increasing K^* and D^*. The amount of phase separation increases as K^* increases and D^* decreases. With the high value of K^*, the polymer entanglements occur in the early stage of phase separation because the degree of polymerization of polymer B N_B increases with K^*.

Chapter 4

Computational Simulation of Polymerization-induced Phase Separation under a Temperature Gradient

Summary

Polymerization-induced phase separation (PIPS) via spinodal decomposition (SD) under a temperature gradient for the case of a monomer polymerizing in the presence of a polymer is studied using high performance computational methods. An initial polymer (A) / monomer (B) one-phase mixture, maintained under a temperature gradient, phase-separates and evolves as polymerization of component B and phase separation proceed to form spatially inhomogeneous microstructures. The space-dependence of the phase-separated structures under the temperature gradient field is determined and characterized using a visualization method. It is found that the droplet-type phase-separated structure is formed in the higher temperature region as a result of the intermediate stage of SD. On the other hand, the lamella- (interconnected cylinder) type phase-separated structure is observed in the lower temperature region, indicating structure of the early stage of SD, in the strong (weak) temperature gradient field. The kinetics of the evolution of composition depends on the magnitude of the temperature gradient field. The non-uniform morphology induced by the temperature gradient is characterized using the novel morphological techniques, known as the intensity and scale of segregation. It is found that the significant (noticeable) non-uniform structure is formed in the strong (weak) temperature gradient while the uniform morphology is formed at constant temperature.

4.1 Introduction

Polymerization-induce phase separation (PIPS) is an important and practical method for producing multi-component composite materials [9, 33, 34]. With increasing demands and interests on multi-phase materials that have better properties and functionality, phase separation, particularly spinodal decomposition (SD), has been active area of material science research. The PIPS process is a more complicated process than the classical thermal-induced phase separation (TIPS) method because phase separation and polymerization occur simultaneously in the PIPS method. For this reason, relatively few theoretical [9, 33-35, 50, 82] and experimental [5, 44, 63, 74, 83] studies have been performed on the PIPS method despite many advantages over other phase separation techniques.

In the PIPS process, an initial mixture is prepared in the one-phase (stable) region and the mixture is homogeneous. When the molecular weight of the components increases due to polymerization, the phase diagram, which has an upper critical solution temperature (UCST) in this study, constantly shifts toward higher temperature and concentration. As a result, the single-phase mixture is thrust into the unstable or metastable region, and phase separation occurs. The polymerization-induced phase-separated morphologies may be different depending on the initial composition and molecular weight. Typically, in a binary polymer blend system, the droplet-type morphology can be found if the volume fraction of one phase is low (off-critical region). If the volume fraction of the minor phase is increased until the critical point (critical region), the interconnected cylinder-type morphology can be observed [1].

The majority of works on phase separation has been performed in the absence of external fields, such as temperature gradient. However, temperature gradients are common during material processing and characterization experiments. Recently a few studies concerning phase separation behavior under external fields such as shear flows [52-54], electric fields [55, 56], and temperature gradients [87, 88] have been presented. In addition, composite materials, exhibiting inhomogeneous microstructures (or composition) and space-dependent properties, known as functionally graded materials (FGM) [89, 90], have received attentions because many current applications of materials require specific bulk/surface properties. For example, a body of turbine blade must be strong, tough and creep-resistant, whereas its outer surface must be refractory and oxidation-resistant [89]. It is expected that in the future similar space-dependent functionality may be applied for polymeric materials. FGM's are designed to take advantage of certain desirable features of each of the constituent phases and reduce the local concentration of stress induced by the abrupt changes in composition and microstructure [89, 90]. The spatially graded structures are produced by several constructive processes. However, as shown here, transport-based processes, such as the polymerized-induced phase separation method, can also create locally graded microstructures.

Phase separation under a temperature gradient was studied by several authors in the last few years [87, 88, 91-93]. Platten and Chavepeyer [91] studied experimentally phase separation under a temperature gradient for a low-molar mass binary solution. Kumaki et. al [93] also performed an experimental study of phase separation under a small temperature gradient and they found that phase separation can be induced by the temperature gradient even in the one-phase region because macromolecules tend to move toward the colder surface. Tran-Cong and Okinaka [87, 88] investigated the TIPS process of poly(2-chlorostyrene) / poly(vinyl methyl ether) (P2CS/PVME) blend under a temperature gradient. Since P2CS/PVME blend has a lower critical solution temperature (LCST), they found that the interconnected structure is formed slowly in the high-temperature side and the droplet-type structure is formed as a result of the late stage of spinodal decomposition in the low-temperature side of the gradient. To our knowledge, however, no numerical study has yet been performed on polymerization-induced phase separation (PIPS) under a temperature gradient.

The objectives of this study are: (1) to develop and solve a computational model of the PIPS process for binary composite materials under a temperature gradient, and (2) to develop guidelines for the formation of spatially inhomogeneous microstructures applied to produce FGM's, using the PIPS process. We study the particular case of the PIPS process of a monomer polymerizing in the presence of a polymer. The organization of this chapter is as follows. In Section 4.2, the PIPS process is described theoretically using the nonlinear Cahn-Hilliard (C-H) theory and the Flory-Huggins (F-H) theory coupled with a reaction kinetic equation. The numerical equation describing the PIPS process under a temperature gradient is formulated and solved using the computational methods. The numerical results are presented in Section 4.3. Section 4.3.1 presents the typical time evolution of the morphology under a temperature gradient field for the different magnitude of temperature gradient. In Section 4.3.2, the dynamical features of PIPS under a temperature gradient are studied and discussed. In Section 4.3.3, the length scale and compositional non-uniformity of phase-separated structures are characterized using a useful morphological characterization techniques, known as the scale of segregation and the intensity of segregation, respectively, as a function of positions along the temperature gradient. Moreover, the results of morphological analysis under the temperature gradient are compared with those of PIPS under constant temperature.

4.2 Theories

In this 2-dimensional study of the PIPS process, it is assumed that a linear temperature gradient exists along, say, the y-axis. The computational domain is a square of size: $0 < x < L$ and $0 < y < L$. Therefore, the temperature field is given by:

$$T(y) = \frac{T_2 - T_1}{L} y + T_1, \qquad T_1 < T_2 \tag{4-1-a}$$

$$\frac{dT}{dx} = 0 \tag{4-1-b}$$

Under the temperature gradient field given in Eq. (4-1), one of the components (monomer), say B, undergoes polymerization while the other component, polymer A, does not participate in this polymerization reaction.

In the PIPS method, the degree of polymerization of component B, N_B, constantly increases due to polymerization. The growth rate of N_B can be determined by solving the following kinetic rate equation [69]:

$$\frac{dp}{dt} = k_1(1 - p)^2 \tag{4-2}$$

where p is the extent of reaction, t is time, and k_1 is the reaction rate constant. The solution to Eq. (4-2) is:

$$p = \frac{k_1 t}{1 + k_1 t} \tag{4-3}$$

The reaction rate constant k_1 depends on reaction temperature, following the Arrhenius equation as [73]:

$$k_1 = A_0 \exp[-E_0/RT] \tag{4-4}$$

where A_0 is the collision frequency factor, E_0 is the Arrhenius activation energy, and R is the gas constant.

The expressions for the weight average molecular size $\overline{X}_w$ in terms of functionality of the monomer γ is given by [70-72]:

$$\overline{X}_w = \frac{1+\alpha}{1-(\gamma-1)\alpha} \tag{4-5}$$

where α is the branching coefficient, defined as the probability that a given functional group of a branch unit leads to another branch unit [73]. By assuming the degree of polymerization of component B, N_B, can be represented by $\overline{X}_w$ and applying Eq. (4.4) for k_1, the growth rate of N_B can be written as:

$$\begin{aligned} N_B &= \frac{1 + 2k_1 t}{1 + 2k_1 t - \gamma k_1 t} \\ &= \frac{1 + 2\,(A_0\exp(-E_0/RT))\,t}{1 + 2\,(A_0\exp(-E_0/RT))\,t - \gamma\,(A_0\exp(-E_0/RT))\,t} \end{aligned} \tag{4-6}$$

Since k_1 depends on reaction temperature, following Eq. (4-4), N_B is a function of both t and y in this study.

The phase separation phenomena via spinodal decomposition can be properly described by the non-linear Cahn-Hilliard equation as [21, 25, 26]:

$$\frac{\partial \Phi_A}{\partial t} = \nabla \cdot \left[M\nabla \left[\frac{\partial f}{\partial \Phi_A} - 2\kappa \nabla^2 \Phi_A \right] \right] \tag{4-7}$$

where Φ_A is the volume fraction of component A (for a binary mixture, $\Phi_A + \Phi_B = 1$), M is mobility, f is free energy density of the system, and κ is a positive interfacial constant.

The Flory-Huggins theory is used for the bulk free energy density f in Eq. (4-7) and is written as [29, 30]:

$$f = \frac{k_B T}{v} \left(\frac{\Phi_A}{N_A} \ln\Phi_A + \frac{\Phi_B}{N_B} \ln\Phi_B + \chi \, \Phi_A \Phi_B \right) \tag{4-8}$$

where k_B is Boltzmann constant, v is the volume of the reference unit, N_A is the degree of polymerization of polymer A, and χ is the temperature dependent interaction parameter. The expression for χ in terms of temperature can be written as [31]:

$$\chi = \frac{1}{2} - \Psi \left(1 - \frac{\Theta}{T} \right) \tag{4-9}$$

where Ψ is the dimensionless entropy and Θ is the theta temperature. Note that the interaction parameter χ also depends on temperature, thus it is also a function of y, in this study.

The mobility M in Eq. (4-7) depends on the molecular weight and local concentration of the components, and, for the low molecular weight regime, it is defined as:

$$M = \frac{v N_A N_B \Phi_A \Phi_B}{\zeta (N_A + N_B)(N_A \Phi_A + N_B \Phi_B)}, \qquad N < N_c \tag{4-10}$$

where ζ is the friction coefficient and N_c is the critical degree of polymerization. For the high molecular weight regime, M is defined as:

$$M = \frac{4\nu N_e N_A N_B \Phi_A \Phi_B}{15\zeta\left(N_A^2+N_B^2\right)\left(N_A\Phi_A+N_B\Phi_B\right)}, \qquad N>N_e \tag{4-11}$$

where N_e is the number of monomer units between entanglements. The full derivations of Eqs. (4-10) and (4-11) are presented in Chapter 2, Section 2.2.2. Lastly, the molecular dependent interfacial parameter κ in Eq. (4-7) is written as [33, 34]:

$$\kappa = \kappa_0\left(N_A + N_B\right) \tag{4-12}$$

where κ_0 the interfacial parameter for a linear polymer.

The dimensionless governing equation describing the polymerization process can be obtained from Eq. (4-6). When we introduce the dimensionless collision frequency factor as $A^* = A_0 L^4 \zeta / 2\kappa_0 \nu$ and the dimensionless activation energy as $E^* = E_0 / R\Theta$, Eq. (4-6) can be expressed in the dimensionless form as:

$$N_B\left(y^*, t^*\right) = \frac{1 + 2A^* \exp\left(-E^*/T^*\right) t^*}{1 + 2A^* \exp\left(-E^*/T^*\right) t^* - \gamma\, A^* \exp\left(-E^*/T^*\right) t^*} \tag{4-13}$$

where $x^* = x/L$, $y^* = y/L$, $t^* = 2\kappa_0 \nu t / L^4 \zeta$, and $T^* = T/\Theta$. The superscripted asterisks denote dimensionless variables.

The detailed expressions for the governing equation describing the phase separation phenomena are given in Sections 2.3 and 3.2 where the dimensionless diffusion coefficient is defined as $D^* = k_B \Theta L^2 / 2\nu\kappa_0$. The governing equation for the phase separation process and the boundary and initial conditions used in Chapter 3 are also used in this study. However, the dimensionless temperature T^*, the Flory-Huggins interaction parameter χ, and the degree of polymerization of component B in the governing equation for the polymerization process are variables along the spatial direction y^* under the temperature gradient, as given in Eq. (4-1), Eq. (4-9), and Eq. (4-13), respectively.

The governing equation describing the polymerization process given in Eq. (4-13) is the dimensionless algebraic equation and it can be solved analytically. However, the governing equation for the phase separation process has to be solved numerically for $\Phi_A^*\left(x^*, y^*, t^*\right)$ using sets of natural and zero mass flux boundary conditions and initial conditions, reflecting the infinitesimal thermal concentration fluctuations presented initially. Hence, the numerical computation is carried in the 2-dimensional geometry ($0 < x^* < 1$, $0 < y^* < 1$), assuming only one of the components, B, in a binary mixture, undergoes polymerization while the degree of polymerization of the component A remains constant ($N_A = 100$), under the temperature gradient. The dependent variables are Φ^*_A and N_B, and the independent variables are x^*, y^*, and t^*. The parameters are the dimensionless diffusion coefficient D^*, the dimensionless collision frequency factor A^*, the dimensionless activation energy E^*, the dimensionless initial average concentration $\Phi^*_{A,0}$, the dimensionless temperature at $y^* = 0$, T_1^*, and at $y^* = 1$, T_2^*, and

Parameter	Value
D^*	2.0×10^6
A^*	2.0×10^7
E^*	10
$\Phi^*_{A,0}$	0.2
Ψ	1
Θ	273
N_A	100
T_1^*	1.500
T_2^*: Case A	1.510
Case B	1.502
Case C	1.500

Table 4.1 Parameter values used in this study. D^* is the dimensionless diffusion coefficient, A^* is the dimensionless collision frequency factor, E^* is the dimensionless activation energy, Θ is theta temperature, $\Phi^*_{A,0}$ is the dimensionless initial average concentration, Ψ is dimensionless entropy, and T_1^* and T_2^* are the lower and higher dimensionless temperature, respectively. Three different temperature gradient fields are examined: Case A (high temperature gradient), Case B (low temperature gradient), and Case C (constant temperature)

the Flory-Huggins interaction parameter, χ. The parameter values used in this study are listed in Table 4.1. The three different cases for the different magnitude of the temperature gradient are studied, i.e. the strong and weak temperature gradient, and constant temperature, as shown in Table 4.1.

In the previous study (see Chapters 2 and 3), we used two different governing equations for phase separation depending on the molecular weight regime of component B, and assumed that the critical degree of polymerization N_c is 31.5. However, in this study, the degree of polymerization of component B never exceeds the critical value. Therefore, only the governing equation for the low molecular weight regime is used.

4.3 Result and Discussion

4.3.1 Typical Phase-Separated Structures and Patterns of PIPS under a Temperature Gradient.

Figure 4.1 shows plots of $1/\chi$ versus Φ_A^* for Case A at the lowest temperature side $\left(T_1^* = 1.50\right)$ and the highest temperature side $\left(T_2^* = 1.51\right)$, at the dimensionless times of $t^* = 2.039 \times 10^{-5}$ and $t^* = 2.091 \times 10^{-5}$. The long and short dashed lines represent the binodal and spinodal lines, respectively, at T_1^*, and the solid and dotted lines denote the binodal and spinodal lines, respectively, at T_2^*. The blank and filled circles represent curing temperature, T_1^* and T_2^*, respectively. The arrow indicates the phase diagram changes with increasing molecular weight of component B. Since $N_A = 100$ and $N_B = 1$ at $t^* = 0$, and everywhere in the system, the lower temperature side is located closer to the initial binodal line. However, as polymerization proceeds, the molecular weight of component B increases faster in the high-temperature region than the low-temperature region because the dimensionless reaction rate constant K^* is proportional to temperature following the Arrhenius equation shown in Eq. (4-4). As a result, for Case A, the curing

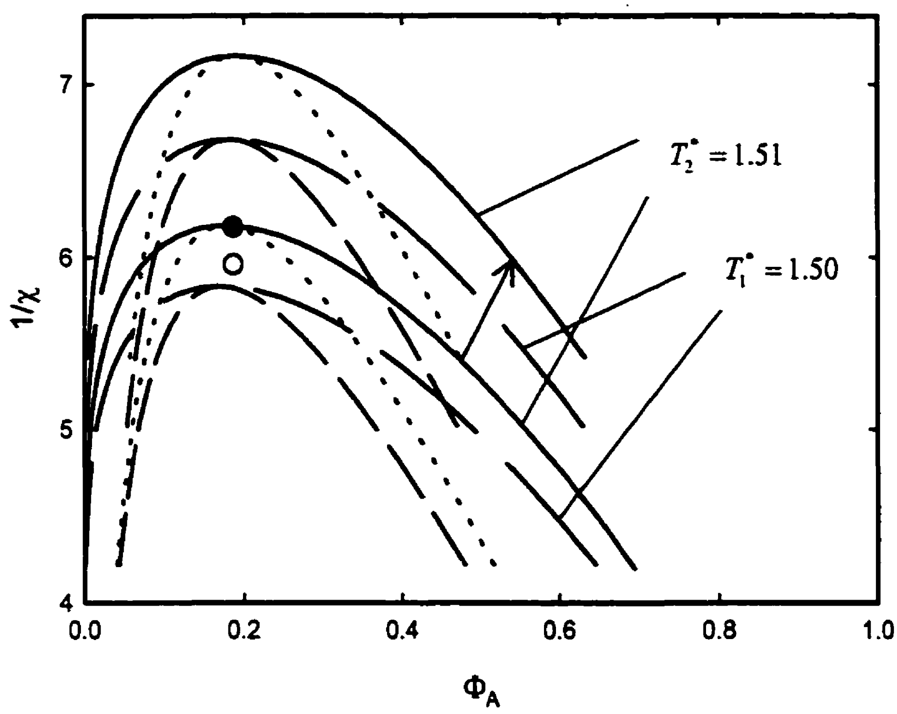

Figure 4.1 Phase diagrams of $1/\chi$ versus Φ_A computed based on the Flory-Huggins equation (Eq. (4-7)) for Case A in Table 4.1, where χ is the Flory-Huggins interaction parameter and Φ_A^* is dimensionless concentration of polymer A. The long and short dashed lines represent the binodal and spinodal lines, respectively, at the lowest temperature (T_1^*). The solid and dotted lines denote the binodal and spinodal lines, respectively, at the highest temperature (T_2^*). The blank and filled circles represent the curing temperature, T_1^* and T_2^*, respectively.

point at the higher temperature side is thrust into the unstable region earlier and phase separation occurs first in the high-temperature region.

Figure 4.2 shows the dimensionless concentration spatial profile, $\Phi_A^*(x^*, y^*)$, (first column) and patterns (second column) formed during phase separation for Case A in Table 4.1 at the following representative dimensionless times: (a) $t^* = 2.531 \times 10^{-5}$, (b) $t^* = 2.570 \times 10^{-5}$, and (c) $t^* = 2.598 \times 10^{-5}$. Darker regions represent polymer A rich regions while brighter regions are polymer B rich regions. The temperature gradient exists along the y^*-axis and the temperature at $y^* = 0$ $\left(T_1^* = 1.50\right)$ is lower than the temperature at $y^* = 1$ $\left(T_2^* = 1.51\right)$. Because we assume that the mixture has an upper

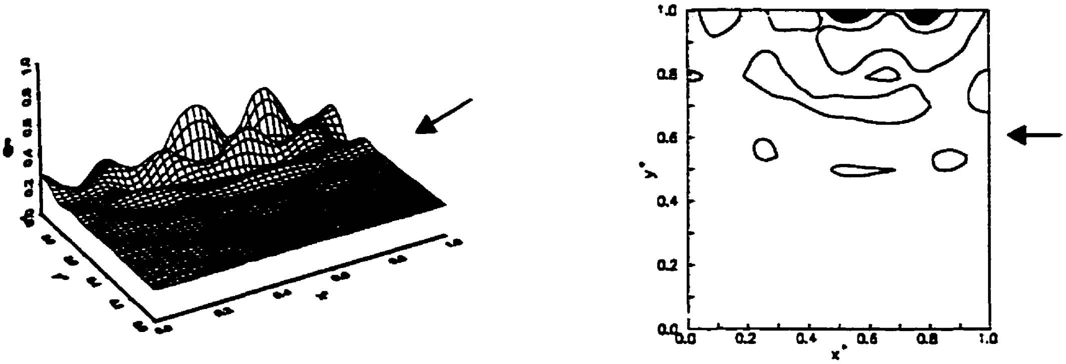

(a) $t^* = 2.531 \times 10^{-5}$

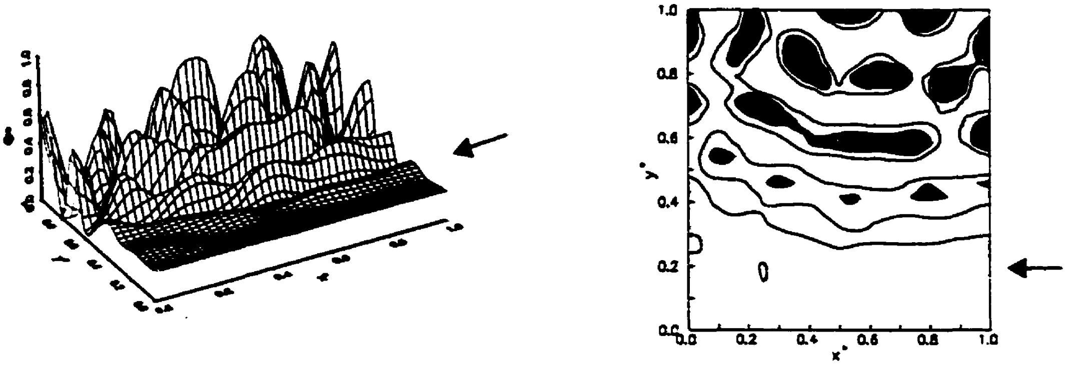

(b) $t^* = 2.570 \times 10^{-5}$

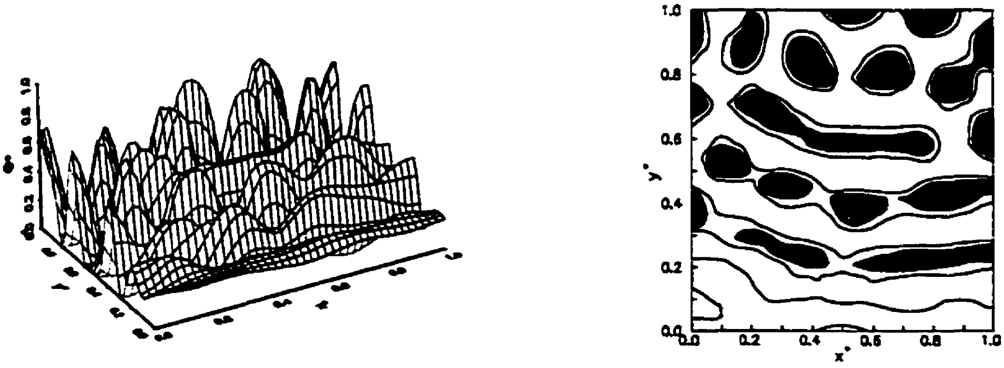

(c) $t^* = 2.598 \times 10^{-5}$

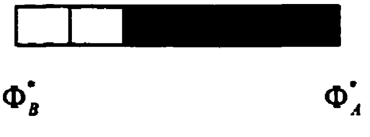

Figure 4.2 Dimensionless concentration spatial profiles $\Phi_A^*(x^*, y^*)$ (first column) and patterns (second column) formed during the phase separation phenomena under a temperature gradient for Case A.

critical solution temperature (UCST), the lower temperature side is closer to the unstable region of the phase diagram than the higher temperature side, as shown in Figure 4.1. However, Figure 4.2 clearly shows that phase separation occurs earlier and more drastically in the high-temperature region. This is obviously due to the different values of the dimensionless reaction rate constants, K^*, along the direction of the temperature gradient. Since the dimensionless reaction rate constant K^* is proportional to reaction temperature according to Eq. (4-4), the phase diagram elevates more rapidly in the high-temperature region as shown in Figure 4.1. As a result, in the high-temperature region, phase separation occurs more significantly, and the droplet-type morphology forms and evolves. Moreover pattern (c) indicates that the phase separation phenomena already reaches to the intermediate stage of phase separation in the high-temperature region. It is noted that phase separation occurs exponentially and the significant phase-separated structure is established during the early stage of phase separation. Phase separation slows down in the intermediate stage as shown in Chapter 3.

In Figure 4.2, the arrows indicate the locations of the front y_f^*, defined as the boundary between the phase-separated region and the region in which no phase separation occurs. The location of the front y_f^* constantly propagates toward the low-temperature region, leaving the high-temperature region behind, as phase separation proceeds. In the high-temperature region far away from y_f^*, $y^* > y_f^*$, phase separation occurs more significantly. On the other hand, in the low temperature region, $y^* < y_f^*$, no phase separation takes place until the front line passes, and in the region near y_f^*, $y^* \approx y_f^*$, phase separation occurs slowly. For the strong temperature gradient field, the propagation of the front line is slow. As a result, a lamella-type of phase-separated structure parallel to the x^*-axis forms in the low-temperature region.

The droplet-type of phase-separated structure indicates that the curing point at the higher temperature side remains in the off-critical region during the polymerization and phase separation process. As phase separation and polymerization proceed, the lamella-type structures slowly break up during the phase separation process to form the droplet-type structure (see Figure 4.4 for constant temperature). Thus in general a composite structure of lamella and droplet morphologies can be obtained by the PIPS method under the strong temperature gradients.

Figure 4.3 represents the dimensionless concentration spatial profiles $\Phi^*_A(x^*, y^*)$ (first column) and patterns (second column) formed during the phase separation phenomena for Case B in Table 4.1, at the following dimensionless times: (a) $t^* = 2.590 \times 10^{-5}$, (b) $t^* = 2.610 \times 10^{-5}$, and (c) $t^* = 2.615 \times 10^{-5}$. A temperature gradient exists along the y^*-axis and the temperature at $y^* = 0$ ($T_1^* = 1.500$) is lower than the temperature at $y^* = 1$ ($T_2^* = 1.502$). Since the temperature gradient for this case is weaker than that for Case A, the front line shown in Figure 4.2 propagates toward the low-temperature region much faster than Case A. As a result, the initial one-phase mixture phase-separates and the initial concentration evolves almost simultaneously. However, the weak temperature gradient also induces the spatially different morphologies (the droplet-type phase-separated structures in the high-temperature region and the highly interconnected cylinder-type morphology in the lower temperature region) in this case, indicating different temporal ranges of phase separation. The interconnected cylinder-type structure also breaks up (see pattern (c)) to form the droplet-type morphology. Consequently, both for Case A and Case B, the spatially graded structures from the lamella- (interconnected cylinder) type to the droplet-type morphology are obtained under the temperature gradient.

The dimensionless concentration spatial profiles $\Phi^*_A(x^*, y^*)$ (first column) and patterns (second column) for constant temperature (Case C in Table 4.1) are presented in Figure 4.4, at the following dimensionless times: (a) $t^* = 2.610 \times 10^{-5}$ (b) $t^* = 2.617 \times 10^{-5}$, and (c) $t^* = 2.640 \times 10^{-5}$. Compared to Case A (Figure 4.2) and B (Figure 4.3), the initial mixture phase-separates and evolves independently on the position during the polymerization and phase separation process. At the early stage of phase separation, the random initial condition develops into an interconnected cylinder-type structure because the initial curing point is located in the critical region at given concentration and temperature, as shown in Figure 4.1. As polymerization proceeds, the phase diagram shown in Figure 4.1 shifts toward higher temperature and concentration region, and the curing point moves off the critical region into the off-critical region. As a

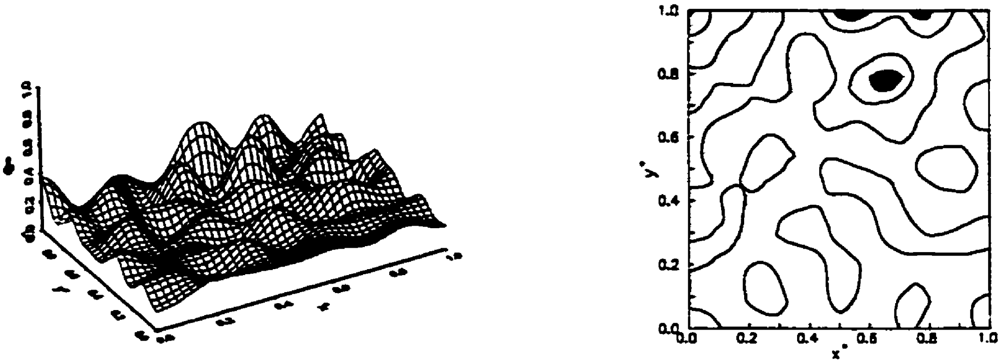

(a) $t^* = 2.590 \times 10^{-5}$

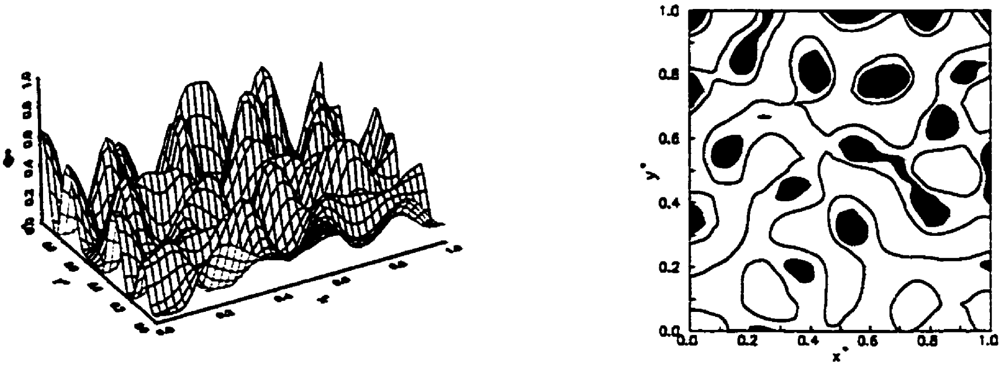

(b) $t^* = 2.610 \times 10^{-5}$

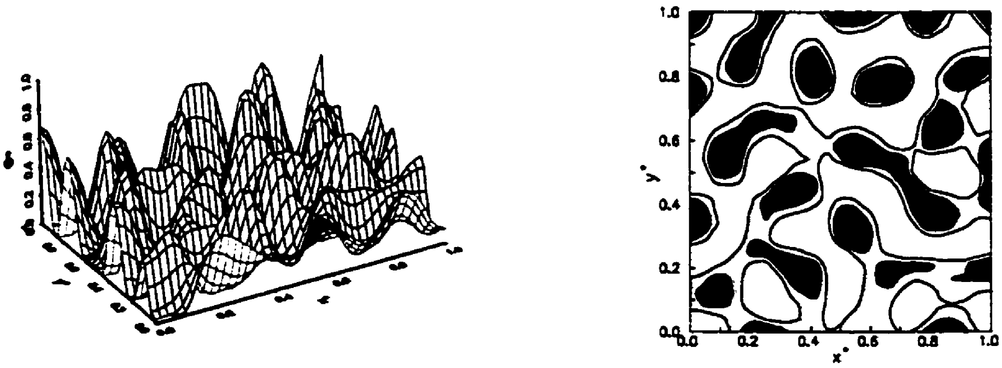

(c) $t^* = 2.615 \times 10^{-5}$

Figure 4.3 Dimensionless concentration spatial profiles $\Phi_A^*(x^*, y^*)$ (first column) and patterns (second column) formed during the phase separation phenomena under a temperature gradient for Case B.

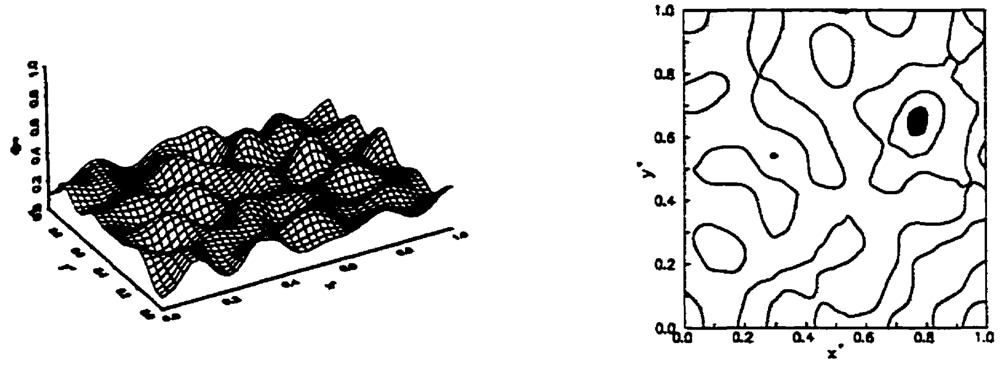

(a) $t^* = 2.610 \times 10^{-5}$

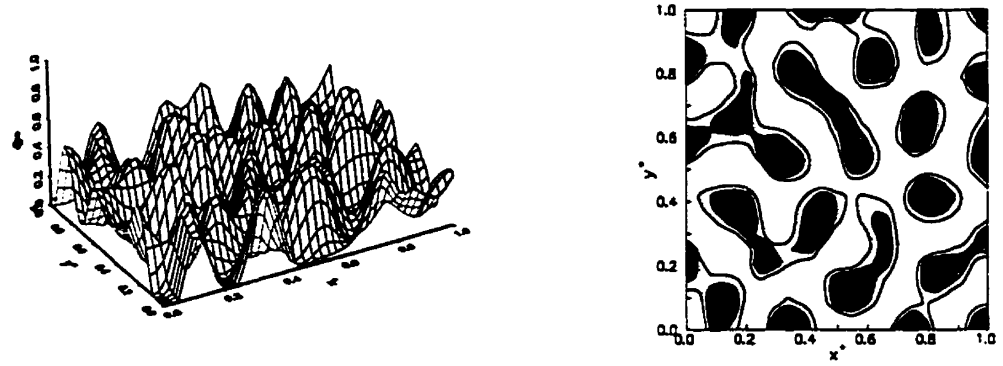

(b) $t^* = 2.617 \times 10^{-5}$

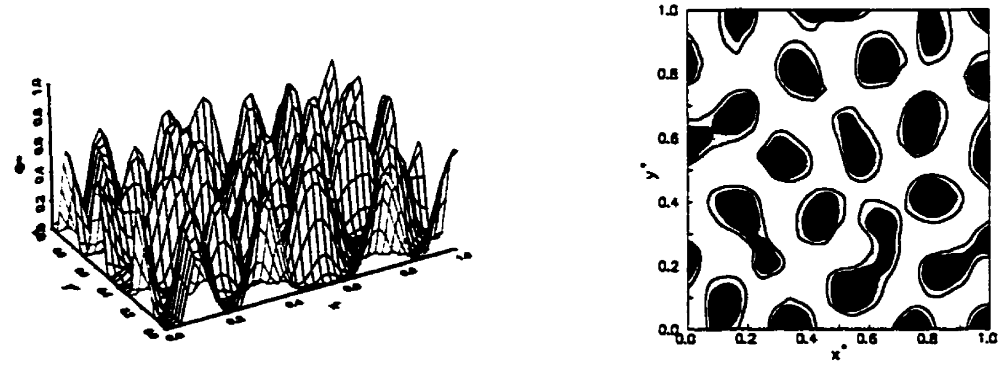

(c) $t^* = 2.640 \times 10^{-5}$

Figure 4.4 Dimensionless concentration spatial profiles $\Phi_A^*(x^*, y^*)$ (first column) and patterns (second column) formed during the phase separation phenomena for Case C (constant temperature).

result, the early phase-separated structure similar to the interconnected cylinder-type develops into the droplet-type structure.

4.3.2 Dynamical Features of PIPS under a Temperature Gradient

It is known that a dimensionless induction time t_i^* exists in the PIPS process and that significant phase separation only occurs at $t^* > t_i^*$ [33, 34]. As shown in Chapter 3, the dimensionless induction time t_i^* can be represented by the sum of the dimensionless polymerization lag time t_{lp}^* and the dimensionless phase separation lag time t_{ls}^* as $t_i^* = t_{lp}^* + t_{ls}^*$. The dimensionless polymerization lag time t_{lp}^* represents the time it takes for the spinodal line to cross the initial curing point and the dimensionless phase separation lag time t_{ls}^* is time required for the system to begin phase separation once it has been placed in the unstable region [33, 34]. The dimensionless polymerization lag time t_{lp}^*, the dimensionless phase separation lag time t_{ls}^*, and the dimensionless induction time t_i^* for Case A, B, and C are listed in Table 4.2.

In this chapter, simulations are performed only for the early stage of phase separation because of numerical limitations. When the interconnected-cylinder type of structure breaks up in pattern (c) in Figure 4.2 and 4.3, rapid variation of the integrand occurs at the pinching points. The time step Δt_i for stable integration must be less than the smallest time scale of the problem. The smallest time scale becomes infinitesimally small with rapid variation of the relaxation velocities $\partial\Phi_A^* / \partial t^*$ at the pinching points, thus limiting the ability of the computational scheme to capture fast and small temporal scale procedures. However, the dominant morphological inhomogeneities depend on the location along the temperature gradient can be found in the very early stage of phase separation. Thus, these computational limitations do not preclude visualization of the main morphological transformations in the PIPS process.

Table 4.2 shows that all the dimensionless kinetic values, t_{lp}^*, t_{ls}^*, and t_i^*, decrease as the magnitude of the temperature gradient increases and the highest temperature in the

Case	$t_{lp}^{*} \times 10^{5}$	$t_{ls}^{*} \times 10^{5}$	$t_{i}^{*} \times 10^{5}$
A	2.039	0.489	2.528
B	2.080	0.505	2.585
C	2.090	0.516	2.606

Table 4.2 Results for dynamical study of polymerization-induced phase separation where t_{lp}^{*}, t_{ls}^{*}, and t_{i}^{*} denote the dimensionless polymerization lag time, the dimensionless phase separation lag time, and the dimensionless induction time, respectively.

system T_2^{*} increases. As discussed in Chapter 3, the dimensionless polymerization lag time t_{lp}^{*} decreases with increasing K^{*}, and the dimensionless phase separation lag time t_{ls}^{*} is inversely proportional to both the dimensionless diffusion coefficient D^{*} and the dimensionless rate constant K^{*}. Since the dimensionless rate constant K^{*} is proportional to temperature, phase separation occurs earlier in the strong temperature gradient field in this study.

4.3.3 Characterizations of the Non-Uniform Phase-Separated Structures

The state of the phase-separated mixture can be fully characterized by measuring two values: 'the intensity of segregation' and 'the scale of segregation' [86]. The intensity of segregation I represents the compositional difference of the each component and it is defined as the ratio of the measured variance to the variance of a completely segregated system as:

$$I = \frac{\left(1/\left(N^{*}-1\right)\right)\sum_{i=1}^{N^{*}}\left(\Phi_{A,i}^{*}-\Phi_{A,0}^{*}\right)^{2}}{\Phi_{A,0}^{*}\left(1-\Phi_{A,0}^{*}\right)} \tag{4-14}$$

where N' is the total number of concentration taken, $\Phi^*_{A,i}$ is the dimensionless concentration of the various points in the sample, and $\Phi^*_{A,0}$ is the dimensionless average concentration. Note that for completely segregated state, $I = 1$, and uniformly distributed state, $I = 0$.

The scale of segregation s represents the length scale of segregated structures and their distributions. The scale of segregation s is defined as the integral of the certain function of correlation, known as the coefficient of correlation $R(r)$, and $R(r)$ is defined as:

$$R(r) = \frac{\sum_{i=1}^{N^*} \left(\Phi'_{A,i} - \Phi^*_{A,0}\right)\left(\Phi''_{A,i} - \Phi^*_{A,0}\right)}{N^* S^2} \tag{4-15}$$

where $\Phi'_{A,i}$ and $\Phi''_{A,i}$ are concentrations at two points at a distance of r from each other, N^* is the total number of couples of concentrations taken, and S is the variance which is calculated from the concentrations at all points. Similarly, for a perfect correlation between the two phases, $s = \varsigma$ where ς represents the value of r at which $R(\varsigma) = 0$, and for no correlation between the two phases, $s = 0$. The detailed explanations for I and s are given in Chapter 3, Section 3.3.

Figure 4.5 shows the intensity of segregation I as a function of y^* for Case A (●, —), Case B (▲, ······) and Case C (■, - - -) at the following characteristic times: (a) $t^* - t_i^* = 0.019$, (b) $t^* - t_i^* = 0.026$, and (c) $t^* - t_i^* = 0.040$. In Figure 4.5, the intensity of segregation I is calculated individually for the particular region along the temperature gradient. In addition, to eliminate the differences of the dimensionless induction time t_i^* due to the temperature gradient for each case, $t^* - t_i^*$ is used for the characteristic time. Note that Case A and Case B are under the strong and weak temperature gradient field, respectively, while Case C is maintained at constant temperature. For all three cases, the intensity of segregation I increases with time. However, the time variations of I are significantly different for each case. For Case A, near the low-temperature side (between $y^* = 0$ and the front y_f^*), $I = 0$, since no phase separation occurs. On the other hand, at the high-temperature side ($y^{*} = 1$), the value of I is considerably high because phase separation occurs significantly in the high-temperature region during the early stage of phase separation. It is also observed that the location of the front y_f^{*} propagates slowly toward the low-temperature side $y^{*} = 0$. In Figure 4.5 (c), phase separation slows down in the high-temperature region, indicating the intermediate stage while phase separation starts to occur in the vicinity of the front. Consequently, the highly position-dependent microstructure forms in the strong temperature gradient field.

Plots of the intensity of segregation for Case B clearly shows that the non-uniform structure forms during the phase separation process in the weak temperature gradient field. As expected, the value of I in the high-temperature side is much higher than that in the low-temperature side. The slopes of plots for Case B are considerably steep compared to those for Case C. Figure 4.5 also shows that the phase-separated morphology evolves uniformly for Case C, and almost same values of I are observed in everywhere.

Plots of the scale of segregation s as a function of y^{*} are shown in Figure 4.6 for Case A (●,—), Case B (▲,┈┈), and Case C (■,- ·) at the following characteristic times: (a) $t^{*} - t_i^{*} = 0.019$, (b) $t^{*} - t_i^{*} = 0.026$, and (c) $t^{*} - t_i^{*} = 0.040$. The scale of segregation s decreases as phase separation proceeds for all three cases. Figure 4.6 also shows that the highly inhomogeneous microstructure forms during the phase separation process for Case A. In the high-temperature region, the value of s is low, indicating that the droplet-type morphology forms as a result of the intermediate stage of phase separation. On the other hand, the morphology in the low-temperature region is the highly lumped lamella-type structure, and the value of s is high.

In the weak temperature gradient field, as shown in plots for Case B, the phase-separated particle size is different along the gradient. Since the value of s in the high-temperature region is slightly lower than that in the low-temperature region, it is expected that the small droplet-type morphology forms in the high-temperature region and the interconnected phase-separated structure develops in the low-temperature region. However, for Case C, the phase-separated morphology evolves uniformly everywhere, and the space-independent droplet-type morphology forms.

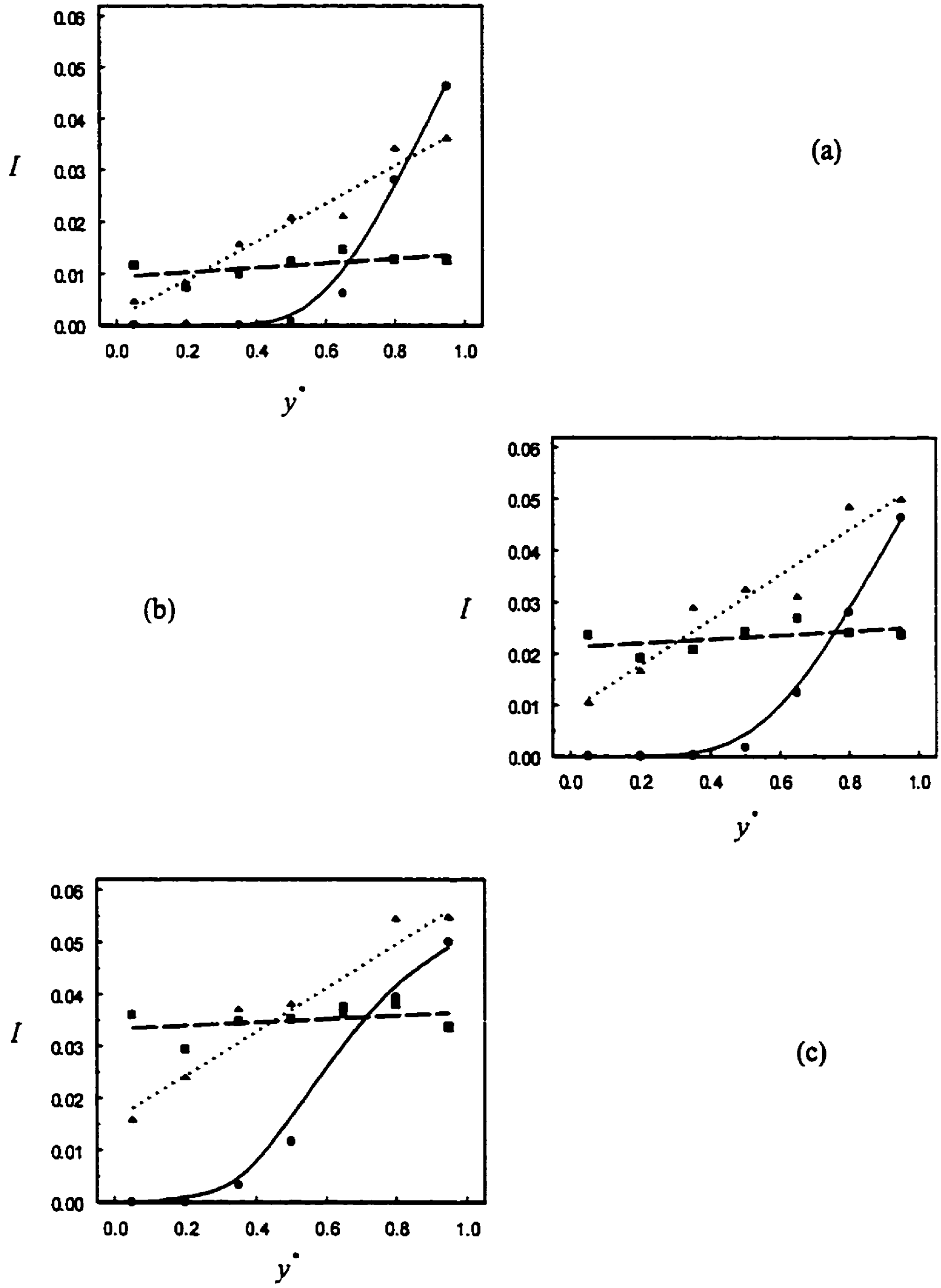

Figure 4.5 Plots of the intensity of segregation I as a function of the position along the temperature gradient y^* for Case A (●, —), Case B (▲,—), and Case C (■,- -) at the following characteristic times: (a) $t^* - t_i^* = 0.019$, (b) $t^* - t_i^* = 0.026$, and (c) $t^* - t_i^* = 0.040$.

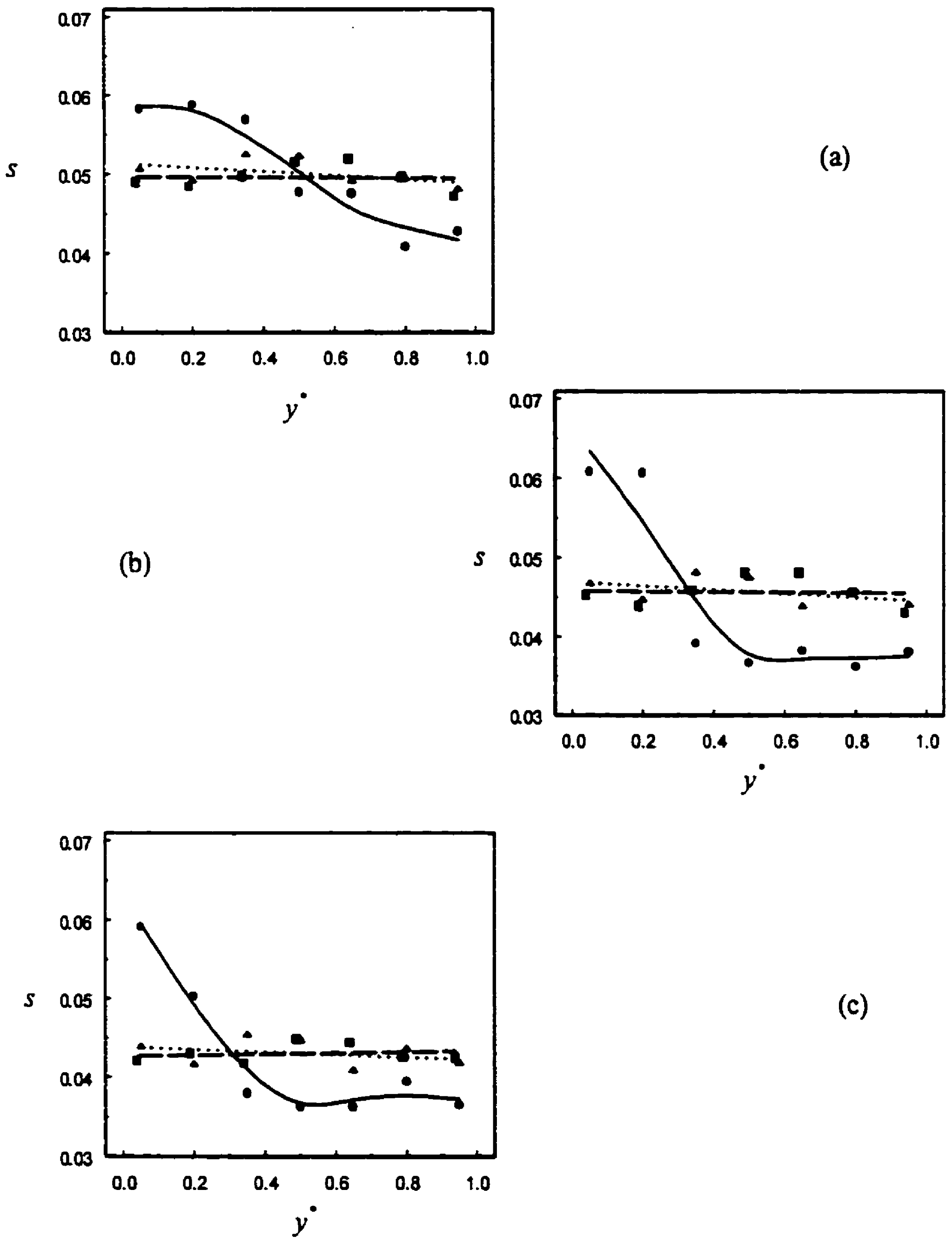

Figure 4.6 Plots of the scale of segregation s versus the position along the temperature gradient y^* for Case A (●,—), Case B (▲,···), and Case C (■,- -) at the following characteristic times: (a) $t^* - t_i^* = 0.019$, (b) $t^* - t_i^* = 0.026$, and (c) $t^* - t_i^* = 0.040$.

In conclusion, the space-dependent morphologies, showing different particle size and shape, are obtained by the PIPS process under the temperature gradient. Since the mechanical and optical properties of multi-component composite material depend on the phase-separated morphology, it is expected that the presented numerical results can be applied to fabricate multi-component polymers with graded properties, and, in particular, FGM with different skin/core properties. As general guidelines, it can be stated that the strong temperature gradient field should be applied for broad distributions of particle size and the highly inhomogeneous microstructures. However, the position-dependent structures with considerably inhomogeneous particle size and shape can be also produced in the weak temperature gradient field.

4.4 Conclusions

This chapter presents the computational modeling of polymerization induced phase separation (PIPS) process under a temperature gradient. The time evolution of morphology under a temperature gradient describes how the initial homogeneous mixture evolves and phase-separates during the phase separation and polymerization process to eventually form a spatially inhomogeneous microstructure. The droplet type morphology (in the high-temperature region) and the lamella type morphology (in the low temperature region) are obtained in the strong temperature gradient field. The location of the front propagates toward the low-temperature side, leaving the high-temperature region behind. In the region far from the front (high-temperature side) phase separation occurs much earlier and more significantly while no phase separation takes place ahead of the front line (low-temperature region). On the other hand, the droplet and interconnected cylinder type structure is found in the weak temperature gradient field.

The kinetic measures of the PIPS process under a temperature gradient, such as the dimensionless polymerization lag time, the dimensionless phase separation lag time, and the dimensionless induction time, decrease as the highest temperature in the system increases due to the increasing reaction rate constant.

Lastly, the time variations of the intensity and scale of segregation as a function of the location along the temperature gradient, also indicate that the phase-separated structure evolves non-uniformly along the gradient. Under a temperature gradient field, the intensity and scale of segregation change more significantly in the high-temperature side than in the low-temperature side. However, the variations of the intensity and scale of segregation are uniformed at constant temperature.

In conclusion, to design FGM (functionally graded materials) with composite lamella-droplet morphologies, these simulations show that the temperature gradient should be greater than a critical value, so that front propagation behavior sets in. In this case, a droplet morphology forms in the hotter region while a lamella morphology with unit normal parallel to the temperature gradient forms in the cooler region. These results provide useful guidelines in the manufacturing of FGM's by the PIPS method.

Chapter 5

Conclusions and Recommendations

This thesis presents a detailed theoretical and computational study of polymerization-induced phase separation (PIPS) method, which is an industrial process for multi-phase material production. In particular, this thesis has been mainly devoted to the industrially relevant PIPS process, consisting of a monomer polymerizing in the presence of a polymer. This study has been performed based on the following two main objectives: (1) the numerical and theoretical study of the PIPS process and (2) the numerical and theoretical study of the PIPS process under a temperature gradient. The first section of this chapter gives the conclusions to this thesis and the second section presents recommendations on further work.

5.1 Conclusions

The characterization and analysis of the main dynamical and morphological features, that are predicted to arise during the PIPS process, can be summarized as follows. (1) The time evolution of morphology exhibits the interconnected phase-separated structure in the critical region and the droplet-type morphology in the off-critical region. (2) Phase separation occurs exponentially during the early stage of phase separation but eventually slows down in the intermediate stage of phase separation. (3) The time and length scales of the phase-separated structure strongly depend on the dimensionless diffusion coefficient D^* and the dimensionless reaction rate constant K^*. Specifically, in dynamical analysis, as D^* and K^* increase, the dimensionless induction time t_i^* and the dimensionless transition time t_t^* decrease. With respect to the morphological analysis, the intensity of segregation I, that represents the difference of the concentration of each component, increases as K^* increases but decreases as D^* increases. The scale of segregation s, that represents the droplet size and distribution, decreases as K^* and D^* increase. The average dimensionless droplet diameter $\langle d^* \rangle$ also decreases as K^* and D^* increase. In addition, droplet number density is proportional to K^* and D^*. Lastly, (4) phase separation slows down drastically in the high molecular weight region (above the critical point N_c) because it is restrained by topological constraints, that is the entanglement of polymers.

The simulation results of the PIPS process under a temperature gradient have shown the following results. (1) The time evolution of morphology exhibits a spatially inhomogeneous phase-separated structure depending on the location along the temperature gradient. In the strong temperature gradient field, the droplet-type morphology is observed in the high-temperature region and the lamella-type morphology forms in the low-temperature region. On the other hand, in the weak temperature gradient field, the droplet-type morphology is found in the high-temperature region and the interconnected cylinder-type phase-separated structure forms in the low temperature region. (2) The dynamical indices of the PIPS process under a temperature gradient, such as the dimensionless polymerization lag time, the dimensionless phase separation lag time, and the dimensionless induction time, decrease as temperature in the system increases. (3) As phase separation and polymerization proceed, the intensity of segregation I increases and the scale of segregation s decreases more significantly in the high-temperature region than the low-temperature region under a temperature gradient, showing broad distribution of particle size and shape, while I and s change uniformly under a constant temperature.

The presented simulation results replicate reported experimental observations on the polymerization-induced phase separation (PIPS) method of forming the binary component composite material and on the phase separation method under a temperature gradient, and serve as useful guidelines for the optimization and control of microstructures in functionally graded polymer material systems.

5.2 Recommendations

The following recommendations are suggested for further work in the subject area of this thesis:

(1) The numerical model used in this thesis has been formulated assuming that the mixture is binary and polymer component is monodispersed. However, for more realistic situation, the ternary mixture and polydispersed molecular weight distribution have to be considered.

(2) Using the ternary component system, the numerical model for a more complex morphology, such as "phase within a phase within a phase", has to be developed and solved.

(3) The numerical model describing the polymerization-induced phase separation (PIPS) process under the shear flow has to be formulated and solved.

References

1. L. H. Sperling, *Polymeric Multicomponent Materials; An Introduction*, John Wiley & Sons, New York (1997).
2. J. C. Salamone, *Polymeric Materials Encyclopedia, Vol. 9*, CRC press, New York (1996).
3. L. A. Utracki, *Encyclopaedic Dictionary of Commercial Polymer Blends*, ChemTec, Toronto (1990).
4. L. A. Utracki, *Polymer Alloys and Blends*, Hanser, New York (1990).
5. P. A. Oyanguren, C. C. Riccardi, R. J. J. Williams, and I. Mondragon, *J. Polym. Sci. Part B*, **36**, 1349 (1998).
6. F. M. Mirabella, Jr., *J. Polym. Sci. Part B*, **32**, 1205 (1994).
7. K. F. Silveira, I. V. P. Yoshida and S. P. Nunes, *Polymer*, **36**(7), 1425 (1995).
8. T. Kojima, T. Ohnaga and T. Inoue, *Polymer*, **36**(11), 2197 (1995).
9. J. W. Doane, A. Golemme, J. L. West, J. B. Whitehead, Jr., and B. –G. Wu, *Mol. Cryst. Liq. Cryst.*, **165**, 511 (1988).
10. J. L. West, *Mol. Cryst. Liq. Cryst.*, **157**, 427 (1988).
11. J. W. Doane, N. A. Vaz, B. –G. Wu, and S. Zumer, Appl. *Phys. Lett.*, **48**, 269 (1986).
12. C. –W. Nan, *Progr. Mater. Sci.*, **37**, 1 (1993).
13. A. J. Markworth, K. S. Ramesh, and W. P. Parks Jr., *J. Mater. Sci.*, **30**, 2183 (1995).
14. S. Suresh and A. Mortensen, *Fundamentals of Functionally Graded Materials: Processing and Thermomechanical Behaviour of Graded Metals and Metal-Ceramic Composites*, The University Press, Cambridge (1998).
15. A. G. Khachaturyan, *Theory of Structural Transformations in Solid*, John Wiley & Sons (1983).
16. P. S. Drzaic, *Liquid Crystal Dispersions*, World Scientific, Singapore (1995).
17. J. W. Doane, *Liquid Crystals: Applications and Uses*, edited by B. Bahadur, World Scientific, Singapore, Vol.1 (1990).
18. B. –G. Wu, J. L. West, and J. W. Doane, *J. Appl. Phys.*, **62**, 3925 (1987).

19. N. A. Vaz, G. W. Smith, and G. P. Montgomery, *Mol. Cryst. Liq. Cryst.*, 146, 1 (1987).

20. N. A. Vaz, G. W. Smith, and G. P. Montgomery, *Mol. Cryst. Liq. Cryst.*, 146, 17 (1987).

21. J. W. Cahn and J. E. Hilliard. *J. Chem. Phys.*, **28**, 258 (1958).

22. R. T. Detloff, *Thermodynamics in Material Science*, McGraw-Hill (1993).

23. J. D. Gunton, M. San Miguel, and P. S. Sahni, *Phase Transitions and Critical Phenomena*, edited by C. Domb and J. L. Lebowitz, Academic Press, Vol. 8, Chapt. 3 (1983).

24. P. K. Chan, *Formation and Performance of Polymer Dispersed Liquid Crystal Films*, Ph.D. Thesis, McGill University (1997).

25. A. Novick-Cohen and L. A. Segel, *Physica D*, **10**, 277 (1984).

26. F. Falk, *J. Non-Equilib. Thermodyn.*, **17**, 53 (1992).

27. P. G. Shewmon, *Diffusion in Solids*, McGraw-Hill (1963).

28. J. Crank, *The Mathematics of Diffusion*, Oxford Univ. Press (1975).

29. J. M. G. Cowie, *Polymers: Chemistry and Physics of Modern Materials*, 2nd ed. Chapman and Hall (1991).

30. P. J. Flory, *Principles of Polymer Chemistry*, Cornell University Press (1953).

31. M. Kurata, *Thermodynamics of Polymer Solution*, Harwood Academic (1982).

32. C. F. Hammer, *Am. Chem. Soc.*, **37**(1), 234 (1977).

33. P. K. Chan and A. D. Rey, *Macromolecules*, **29**, 8934 (1996).

34. P. K. Chan and A. D. Rey, *Macromolecules*, **30**, 2135 (1997).

35. S. C. Glotzer, E. A. Di Marzio, and M. Muthukumar, *Phys. Rev. Lett.*, **74**(11), 2034 (1995).

36. A. Chakrabarti, R. Toral, J. D. Gunton and M. Muthukumar, *Phys. Rev. Lett.*, **63**(19), 2072 (1989).

37. A. Chakrabarti, R. Toral, J. D. Gunton and M. Muthukumar, *J. Chem. Phys.*, **92**(11), 6899 (1990).

38. A. Chakrabarti, *Phys. Rev. B*, **45**, 9620 (1992).

39. J. S. Langer, M. Baron and H. D. Miller, *Phys. Rev. A*,. **11**, 1417 (1975).

40. H. Furukawa, *Physica A*, **180**, 128 (1992).

41. T. Matsuoka and S. Yamamoto, *J. Appl. Polym. Sci.*, **57**, 353 (1995).

42. H. Zhang, J. Zhang and Y. Yang, *Macromol. Theory Simul.*, **4**, 1001 (1995).

43. B. F. Barton, P. D. Graham, and A. J. McHugh, *Macromolecules*, **31**, 1672 (1998).

44. W. Chen, X. L. Tao Dong, and M. Jiang, *Macromol. Chem. Phys.*, **199**, 327 (1998).

45. W. Chen, J. Wu and M. Jiang, *Macromol. Chem. Phys.*, **199**, 1683 (1998).

46. J. Kojima, M. Takenaka, Y. Nakayama, and T. Hashimoto, *Macromolecules*, **32**, 1809 (1999).

47. C. Shen and T. Kyu, *J. Chem. Phys.*, **102** (1), 556 (1995).

48. P. K. Chan and A. D. Rey, *Comput. Mater. Sci.*, **3**, 377 (1995).

49. P. K. Chan and A. D. Rey, *Macromol. Theory Simul.*, **4**, 873 (1995).

50. B. Lin and P. L. Taylor, *Polymer*, **37** (22), 5099 (1995).

51. I. Chikina, *J. Chem. Phys.*, **109** (6), 2429 (1998).

52. F. Corberi, *Phys. Rev. Lett.*, **81** (18), 3852 (1998).

53. A. J. Wagner and J. M. Yeomans, *Phys. Rev. E*, **59** (4) 4366 (1999).

54. M. Tirrell, *Fluid Phase Equilibrium*, **30**, 367 (1986).

55. D. Wirtz and G. G. Fuller, *Phys. Rev. Lett.*, **71**, 2236 (1993).

56. S. Venugopal and S. Krause, *Macromolecules*, **25**, 4626 (1992).

57. S. A. Shaginyan and L. I. Manevich, *Polym. Sci. Ser. A*, **39** (8), 908 (1997).

58. P. E. Rouse, *J. Chem. Phys.*, **21**, 1272 (1953).

59. P. G. de Gennes, *J. Chem. Phys.*, **72**(9), 4756 (1980).

60. M. Doi and S. F. Edwards, *The Theory of Polymer Dynamics*, Clarendon Press (1986).

61. V. Abetz, *Macromolecules*, **27**, 4621 (1994).

62. T. Ohnaga, W. Chen and T. Inoue, *Polymer*, **35**(17), 3774 (1994).

63. W. Chen, S. Kobayashi, T. Inoue, T. Ohnaga and T. Ougizawa, *Polymer*, **35**(18), 4015 (1994).

64. E. L. Cussler, *Diffusion. Mass Transfer in Fluid Systems*, 2nd Ed. Cambridge University Press (1997).

65. K. Kremer, G. S. Grest and I. Carmesin, *Phys. Rev. Lett.*, **61**(5), 566 (1988).

66. K. Kremer and G. S. Grest, *J. Chem. Phys.*, **92**(8), 5057 (1990).

67. C. C. Lin, H. S. Jeon, N. P. Balsara and B. Hammouda, *J. Chem. Phys.*, **103**(5), 1957 (1995).

68. K. Binder, *J. Chem. Phys.*, **79**, 6387 (1983).

69. J. M. Barton, *Advances in Polymer Science*, edited by K. Dusek, Spriner-Verlag, Vol. 72 (1985).

70. W. H. Stockmayer, *J. Chem. Phys.*, **11**, 45 (1943).

71. W. H. Stockmayer, *J. Polym. Soc.*, **9**, 69 (1952).

72. W. H. Stockmayer, *J. Polym. Soc.*, **11**, 424 (1953).

73. G. Odian, *Principles of Polymerization*, 3rd ed., John Wiley & Sons (1991).

74. T. Inoue, *Prog. Polym. Sci.*, **20**, 119 (1995).

75. L. J. Fetters, D. J. Lohse, D. Richter, T. A. Witten, and A. Zirkel, *Macromolecules*, **27** (17), 4639 (1994).

76. C. M. Elliott and Z. Songmu, *Arch. Ration. Mech. Anal.*, 96, 339 (1986).

77. W. B. Bickford, *A First Course in the Finite Element Method*, 2nd Ed., Richard. D. Irwin (1994).

78. C. A. J. Fletcher, *Computational Galerkin Methods*, Springer-Verlag (1983).

79. A. I. Borisenko and I. E. Tarapov, *Vector and Tensor Analysis with Applications*, Dover Publications (1979).

80. G. F. Carey and J. T. Oden, *Finite Elements : A Second Course*, Prentice-Hall (1983).

81. B. A. Finlayson, *Nonlinear Analysis in Chemical Engineering*, McGraw-Hill, New York (1980).

82. J. C. Lin and P. L. Taylor, *Phys. Rev. E*, **49**(3), 2476 (1994).

83. B. S. Kim, T. Chiba, and T. Inoue, *Polymer*, **36**(1), 43 (1995).

84. M. V. Ariyapadi and E. B. Nauman, *Computer Simulation of Polymers, Chapt. 27*, edited by R. J. Roe, Prentice Hall (1992).

85. B. Julesz, *Sci. Am.*, **232**, 34 (1975).

86. Z. Tadmor and C. G. Gogos, *Principles of Polymer Processing, Chapt. 7*, Wiley-interscience (1979).

87. J. Okinaka and Q. Tran-Cong, *Physica D*, **84**, 23 (1995).

88. Q. Tran-Cong and J. Okinaka, *Polym. Eng. and Sci.*, **39**(2), 365 (1999).

89. S. Suresh and A. Mortensen, *Fundamentals of Functionally Graded Materials: Processing and Thermomechanical Behaviour of Graded Metals and Metal-Ceramic Composites*, The University Press, Cambridge (1998).
90. A. J. Markworth, K. S. Ramesh, and W. P. Parks Jr., *J. Mater. Sci.*, **30**, 2183 (1995).
91. J. K. Platten and G. Chavepeyer, *Physica A*, **213**, 110 (1995).
92. G. Chavepeyer, J. K. Platten, and M. Salajan, *J. Non-Equilib. Thermodyn.* **21**(2), 122 (1996).
93. J. Kumaki, T. Hashimoto, and S. Granick, *Phys. Rev. Lett.*, **77**(10), 1990 (1996).